Electrochemical Lithiation and Delithiation for Control of Magnetic Properties of Nanoscale Transition Metal Oxides

by

Vikram Sivakumar

Submitted to the Department of Materials Science and Engineering
in partial fulfillment of the requirements for the degree of

Doctor of Philosophy in Materials Science and Engineering

at the

MASSACHUSETTS INSTITUTE OF TECHNOLOGY

February 2008

Author .....
.....
Department of Materials Science and Engineering
January 04, 2008

Certified by.....
Caroline A. Ross
Professor of Materials Science and Engineering
Thesis Supervisor

Accepted by.....
.....
Samuel Miller Allen
POSCO Professor of Physical Metallurgy
Chair, Departmental Committee on Graduate Students

Electrochemical Lithiation and Delithiation for Control of Magnetic Properties of Nanoscale Transition Metal Oxides

by

Vikram Sivakumar

Submitted to the Department of Materials Science and Engineering
on January 04, 2008, in partial fulfillment of the
requirements for the degree of
Doctor of Philosophy in Materials Science and Engineering

Abstract

Transition metal oxides comprise a fascinating class of materials displaying a variety of magnetic and electronic properties, ranging from half-metallic ferromagnets like CrO_2, ferrimagnetic semiconductors like Fe_3O_4, and antiferromagnetic insulators like rocksalt-structured FeO. The accessibility of multiple electronic configurations and coordination of cations in these oxides enables the control of magnetism by external stimuli. One such stimulus is the insertion of Li^+, as occurs during the discharge cycle of a lithium battery. This can lead to the change in valence and locations of the metal cations within the structure therefore a change in magnetic moment.

Fe_3O_4 and CrO_2 are of considerable interest, primarily because they demonstrate room-temperature magnetism and high spin polarization.Previous studies focussed on use of these materials as cathodes and characterization of lithiated compounds made through solid state chemical synthesis or via chemical lithiation. In this work, changes in magnetization and structure of pulsed laser deposition (PLD)-grown Fe_3O_4 (magnetite) thin films, Fe_3O_4 nanoparticles, and CrO_2 nanoparticles have been investigated upon electrochemical lithiation.

The reasonable electrical conductivity of magnetite opens the possibility of modifying the saturation magnetization by inserting Li^+ ions into thin films grown on conducting substrates. A substantial decrease in M_s (up to 30%) was observed in PLD-grown thin films. Significantly larger reduction in moment (up to 75%) was observed in commercially available nanoparticles upon addition of 2 moles of Li per formula unit, along with changes in remanence and coercivity. The smaller drop in M_s observed in thin films is attributed to a kinetic effect due to high density and greater diffusion lengths in PLD-grown films.

The electrochemical lithiation process has also been applied to needle-shaped particles of chromium dioxide and a model has been proposed to explain the observations. The effects of cycling and discharge-charge rate on these CrO_2 particles have been studied. It has been shown that the process may be partially reversible for low Li contents. The effects of increasing the temperature of cycling and decreasing the length of the CrO_2 particles have been explored. These changes in magnetic moment

may be rendered useful in magnetomechanical or magnetoelectronic applications.

Thesis Supervisor: Caroline A. Ross
Title: Professor of Materials Science and Engineering

Acknowledgments

Firstly, I would like to express my gratitude to Professor Caroline Ross for her guidance and support. I am very grateful to her for her inspiring leadership and judgement, especially during difficult phases. Her kind words of encouragement over the years have been truly invaluable.

I thank Prof. Harry Tuller and Prof. Gerd Ceder for being on my thesis committee. I wish to thank Prof. Ceder for his input and ideas for the project. I would like to thank Prof. Tuller for his valuable time and guidance during thesis writing. I am grateful to Prof. Yang Shao-Horn and her postdocs Dr. Sundeep Kumar and Dr. Naoaki Yabuuchi for their collaboration. I thank Naoaki for his patience and valued input. I would also like to thank Prof. Dane Morgan and Dr. Kristin Persson from the Ceder group, in particular Prof. Morgan for patiently tutoring me on oxide magnetism and superexchange.

My heartfelt thanks to the members of the Magnetic Materials and Devices Group. I have benefited greatly from their kind support and able mentorship. I would like to thank Dr. Fernando Castano and Dr. Wonjoon Jung for their time and patience. I am thankful to Filip Ilievski, Dr. Tamar Tepper and Dr. Ashok Rajamani for their guidance during my early days in the group. I am especially grateful to Filip for his valuable time and input, thoughtful discussions, and for being a simply great colleague and person.

I wish to thank other former and present members of the Ross group, including Dr. Elizabeth Friend, Dr. Deborah Morecroft, Vivian Chuang, Alex Taussig, Irenee Colin, David Navas (thanks for help with thesis drafts!), Lei Bi and Dr. Hyunsuk Kim for making the group a cordial place, and for the lunch/dinner outings during the conference trips. Thank you Gabrielle for your cheerful presence! I also wish to thank members of Prof. Tuller's group, especially Dr. Dilan Seneviratne, Jussi Hiltunen, Scott Litzelman, Dr. Tsachi Avrahami, Dr. Il-Doo Kim and Dr. Joshua Hertz, for taking time out from their busy schedules to help out with the PLD. Acknowledgments are due also to the members of EEL, especially Gerardo Jose Lao

and Anjuli Appapillai; Dr. Jorge Feuchtwanger (of Prof. Bob Handley's group); and to Dr. David Bono for his guidance. I am grateful to Mr. Peter Morley of the machine shop; and to Dr. Scott Speakman and Mr. Peter Kloumann of the XRD lab. I would also like to thank Jeff Edberg of Coherent Inc. and Erik Samwell of ADE Magnetics for their support on technical issues. I thank the staff of the DMSE, including Kathy Farrell, Angelita Mireles, Stephanie Bright and Gerry Hughes for their efforts.

It has personally been a great experience for me to have had the opportunity of scholarship at MIT. The doctorate has instilled in me an appreciation of the scientific method. It has also taught me the value of the pursuit of knowledge.

My sincere thanks to all of my friends, who have helped me navigate through some tough times. I wish to express my gratitude here to Vikrant, Arjun, Pranava, Rags, Simran, Vikas, Vijay, J. Srini and Mithila. The weekend sessions of cricket, movies and food have been enjoyable. Vikrant - thanks for organizing the cricket games. Pranava and Rags - thank you both for being good roommates. Vijay, J. Srini, Hari - thanks for the insightful discussions. Vikas - thanks for introducing me to the tennis ladder! Special thanks to Simran - she was kind in offering to proof-read my first thesis draft and also to offer good food! Additionally, I would like to thank: my neighbors in the dorms - Mithila, Bhanu, Harish, Vikram and Abhinandan; also Sivaram, Dhananjay and Jaykumar for their help with resolving issues of coding in LaTeX. I also wish to express my gratitude to Ann Orlando and Prof. Terry Orlando, Housemasters of Ashdown; and to Dilip and Janaki Subramanyam, my host family in Boston - thank you for your incredible kindness and hospitality.

Finally, I would like to thank my family. My brother has been an inspiration to me. He and my sister-in-law Aparna have helped me stay balanced. I should thank my grandparents who have been a great source of strength and comfort. My father has worked hard to give me the freedom to pursue my dreams, and I respect him immensely for that. My mother has taught me to believe in myself, and has made innumerable sacrifices. For that and more, I love her, and I shall be eternally grateful.

Contents

List of Figures

List of Tables

Chapter 1

Introduction and Motivation

Transition Metal Oxides (TMOs) comprise a fascinating class of materials that display a wide range of magnetic and electronic properties. These range from half-metallic ferromagnets like CrO_2 to antiferromagnetic insulators such as rocksalt-structured FeO. Magnetic transition metal compounds have been exploited in many applications over the years, from microwave devices to magnetoelectronics [5, 6, 7, 8]. In recent years, there has been a renewed interest in this area. In particular, oxides such as Fe_3O_4 and CrO_2 are being studied as candidates for spin injection in magnetoelectronic devices due to the high degree of spin polarization in these materials and due to the low-loss nature of spin-polarized current. Spin transition ceramics and coordination polymers, in which a Low Spin (LS) to High Spin (HS) transition can be triggered by temperature (or light or pressure), are in demand for applications in energy absorption [9, 10].

1.1 Magnetism in Transition Metal Oxides

Magnetism in TMO's such as Fe_3O_4 is due to coupling of spins of cationic 3d electrons via superexchange mediated by the intervening anion. As an example, let us consider the structure of the ferrimagnetic spinel Fe_3O_4. Here, the spontaneous moment arises from the difference in moments on the A (tetrahedral) and B (octahedral) sublattices. The moments due to the Fe^{3+} ions in the structure cancel

out, leaving the moments on the Fe^{2+} ions in the B sublattice. Here a difference in the moments of the individual ions (dipoles) creates the magnetism. In other cases, for example the defect spinel maghemite, that can be written as $(Fe^{3+})_{8a}$ $(Fe^{3+}{}_{5/3}$ ϕ $_{1/3})_{16d}$ O_4, it is the difference in the number of ions (i.e. the number of dipoles) due to vacancies ϕ on B sites that creates the ferrimagnetism. There can be other sources of magnetism in oxides, for example the "parasitic magnetism" observed in hematite α-Fe_2O_3 due to canting of moments on the Fe^{3+} ions in the basal plane of the hexagonal structure. This gives rise to the weak moment in the otherwise antiferromagnetic hematite. In $Fe_{1-x}O$, the presence of iron vacancies means that the moments do not exactly cancel out as expected to by solving for the ground state. In this thesis, we are interested in the first type of magnetism (ferrimagnetism) and in particular, in developing ways of changing the magnetic properties reversibly. It is expected that the magnetic properties could be modified by changing the number of available electrons or the bond length between ions. The accessibility of multiple electronic configurations and coordination of cations in these compounds enables the tuning of magnetism by an external stimulus, such as a change in the environment, or of temperature or pressure.

1.2 Electrochemistry

The conversion of electrical energy into chemical energy, which is the basis for electrochemical phenomena, can be used to control the magnetism of oxides. One such example is the insertion of Li^+ ions into the structure, which can reduce the valence states of cations, alter the metal-oxygen-metal (M-O-M) bond angles and M-O bond distances, and possibly also the coordination of transition metal ions in the structure. Since the magnetic properties of these oxides are largely determined by the oxidation state and geometrical arrangement of the magnetic ions, this offers us the possibility of controling the magnetic properties electrochemically. This can be investigated experimentally by electrochemical discharge of a Li battery consisting of the transition metal oxide as cathode.

1.3 Iron Oxide and Chromium Dioxide

The work in this thesis is focused on iron oxide and chromium dioxide. Magnetite, Fe_3O_4, is the oldest magnetic material known to man. However, it has many interesting properties that pique curiosity even today. It is a room-temperature ferrimagnet with a high Curie temperature and a high degree of spin polarization, which makes it attractive for spintronics. Magnetite is a well-studied spinel, which is still under intense scientific scrutiny for its interesting physics and wealth of applications which include microwave devices, ferrofluids and spintronics. Fe_3O_4 has also been researched as a thin film cathode for rechargeable Li-ion batteries. The spinel structure consists of cations in tetrahedral and octahedral interstices within a face centered cubic packed anion lattice. Magnetite crystallizes in the inverse spinel structure (Fd3m space group), where Fe^{2+} ions occupy the 16d octahedral sites and Fe^{3+} ions are distributed equally among tetrahedral (8a) and 16d sites. This means that 1/8 of the 64 tetrahedral sites and 1/2 of the 32 octahedral sites are occupied.

Magnetite has good electronic conductivity, due to hopping of electrons between octahedral sites. Also, close-packed oxygen arrays such as spinels have room- temperature Li^+ mobility [11]. This mixed ionic-electronic conductivity makes Fe_3O_4 a viable cathode material. Li^+ mobility can be enhanced by vacancies in the structure, as occur in maghemite γ-Fe_2O_3, which can be thought of as iron-deficient magnetite with vacancies (ϕ) in 16d octahedral sites, and can be written $(Fe^{3+})_{8a}$ $(Fe^{3+}{}_{5/3}\ \phi_{1/3})_{16d}$ O_4.

CrO_2 is another interesting material because it is the only known stoichiometric binary oxide that has the useful property of being a ferromagnetic metal [12]. It has therefore been studied extensively by researchers [12, 13, 14, 15, 16, 17, 18, 19]. Most transition metal oxides are either antiferromagnetic insulators or ferrimagnets, but CrO_2 possesses a curious mix of electronic conductivity and ferromagnetism [14] because the Cr d bands are divided into two sub-bands. The first sub-band is a weakly interacting localized d state below the Fermi level. These d states provide the local atomic moments [14]. The other band is a hybridized d band close to the Fermi level

which provides metallicity. This makes CrO_2 a half-metal, with a spin polarization (measured by Andreev reflectometry) in the range 80-97% at temperatures close to 1 K [12, 15, 16, 17].

Additionally, the presence of room-temperature magnetism in CrO_2 is a desirable property; the Curie temperature is 392 K. However, CrO_2 is metastable under ambient conditions. It has been successfully grown as a good quality thin film via chemical vapor deposition [17]. Historically, CrO_2 has been used in particulate magnetic recording tapes, and also as an oxidizing agent in various chemical reactions. It is considered as a potentially useful material for applications in spintronics [5, 6, 7, 8].Despite being a metastable compound, CrO_2 has been studied extensively, and has been used in magnetic tape recording media [12, 13, 14, 15, 16, 17, 18, 19].

1.4 Motivation

In this section, the overall motivation for the thesis will be outlined.

To date, there has been little study of the effects of electrochemical lithiation on the magnetic properties of chromium dioxide. Also, studies on Fe_3O_4 for its use as a material for cathodes of Li batteries have focused on its suitability as a battery material, and have not systematically tested the effects of the process on the magnetic properties. We therefore aim to explore the effect of lithium insertion in these materials, in particular the reversibility and magnitude of changes in saturation moment.

The ability to reversibly manipulate the magnetic properties of materials by external stimuli is of considerable interest in the development of sensors, actuators and other magnetic devices. The requirement for room temperature chemical magnetic switching necessitates some practical considerations. First, we are constrained to look at materials that have their Curie and Néel temperatures at or above room temperature. Ideally, there should be a substantial change in magnetic moment, and therefore we should use materials that have large moments to begin with. This narrows down the possibilities. Most of the known metallic oxides are antiferromagnetic. The ex-

ceptions are the ferromagnetic oxides EuO and CrO_2 and the ferrimagnetic spinels Fe_3O_4 and γ-Fe_2O_3. Out of these, CrO_2 (T_C = 395 K), Fe_3O_4 (T_N = 858 K) and γ-Fe_2O_3 have ordering temperatures above room temperature. CrO_2 has been grown by Chemical Vapor Deposition [10] but so far single-phase CrO_2 films have not been grown by Pulsed Laser Deposition. Transition metal oxides are very promising for such applications, primarily because of the accessibility of multiple electronic configurations due to a multitude of valence and spin states and coordination of the cations therein. In particular, compounds with manganese, chromium, cobalt and ruthenium could be exploited, as these elements exist in multiple valence states.

The materials for the purpose of this thesis were narrowed down to Fe_3O_4 and CrO_2, primarily due to two reasons. Firstly, these satisfy the preconditions of room-temperature magnetism and high saturation magnetization. Secondly, these are well-researched in the literature, and have many practical applications.

The objective of the thesis is to create large (and preferably reversible) changes in the room-temperature magnetic properties of nanoscale transition metal oxides by using a process that is similar to the discharge/charge process in a rechargeable lithium battery. The Li^+ ions are inserted into the oxide lattice during discharge and de-intercalated during charging. The insertion of lithium leads to a change in the valence states of the Fe ions and a corresponding change in the overall magnetization of the ferro/ferrimagnetic material. For example, the insertion of Li^+, as occurs during the discharge cycle of a lithium battery, can lead to the reduction of metal cations and a change in magnetic moment. Another objective of this thesis is to gain better understanding of the physics of the lithium insertion process in these materials, in particular, the effects on intrinsic magnetism.

1.5 Applications

There could be several applications of chemically switchable magnetism.

One example is programmable magnetoelectronic devices, such as reversible "magnetic" switches, in which a device is switched between low and high states of magnetization.

This could possibly be used for creating an additional state for bits in magnetic media or magnetic random access memories. Present day magnetic devices rely on defining the bit state by the magnetization state being "up" or "down" (in the case of perpendicular magnetic recording media) or "left" or "right" in plane (in the case of the more classic longitudinal configuration, or in MRAMs). In addition to this, if we were able to reversibly turn on/off the magnetism, this could be potentially useful in creating an additional degree of freedom for information storage because it allows for manipulation of the spin state. However for this to happen, there has to be integration of a solid state Li battery (eg. doped conducting oxide-Transition Metal Oxide-BCP electrolyte-Li multilayer dots) into storage media. It may then be possible to switch between not only up and down states or intermediate magnetization states, but also into a state of zero magnetization, for example by sweeping a voltage applied on the (multilayer) bit at constant discharging and charging currents.

Such a solid state electrochemical device might have inherent limitations on the switching speed (write/erase time) and the endurance, which is the number of write cycles for a given byte. These may not compare favorably with present day MRAM technology (Table 1.1), especially the prototype MRAMs involving spin transfer torque (STT), which exhibit sub-ns switching speeds and almost unlimited ($>10^{15}$) endurance [20]. However, there could potentially be benefits in issues pertaining to power requirements. These practical aspects will be discussed in more detail in Chapter 6.

A second example of an application for a material that shows reversible changes in

Table 1.1: Existing and prototype memory technologies

	MRAM	STT	Flash(NOR)	Flash(NAND)
Write/erase time	3-20 ns	2-20 ns	1 μs/10 ms	1 ms/0.1 ms
Write power	high	low	very high	very high
Voltage	3 V	0.15 V	6-8 V	16-20 V
Endurance	$>10^{15}$	$>10^{15}$	10^5	10^5

magnetic properties in response to a chemical stimulus is to incorporate the material as submicron/nanoparticles in a magnetic fluid. The electrochemical processes

may be accelerated due to kinetic considerations. The tuning of magnetism in these materials via a change in the chemical composition can lead to another interesting application. The fluid can then be triggered to switch reversibly between a relaxed and stiff state within a reasonably fast time. These would be similar to electrorheological or magnetorheological fluids, with the only difference being that the switching and the resultant change in stiffness could be achieved without application of large electric or magnetic fields as triggering mechanisms, which maybe very useful in certain applications such as for dynamic armor. This work could also potentially be used in magnetic actuation, wherein the Li insertion and de-insertion processes could be used as stimulus for actuation.

A third application is as a new type of sensor for Li^+ ions, since a small amount of Li could potentially create large detectable changes in magnetism. Such sensors can possibly be used for monitoring lithium levels in blood serum samples to prevent overdose during therapy. Although other alkali metal and alkaline earth metal ions such as Na^+, K^+, Mg^{2+} and Ca^{2+} may act as interferents, the much larger size of these ions compared to Li^+ might help in yielding good selectivity for Li ions.

In summary, the aim of the thesis is to study the effect of electrochemical lithium insertion on the magnetic properties of thin films and nanoparticles of Fe_3O_4 and that of submicron-sized/nano particles of CrO_2. The thesis has been organized as follows. In the next chapter, the theory of magnetism in oxides is described, followed by the thermodynamics and kinetics of the electrochemical lithiation process. In Chapter 3, the experimental methods used in the thesis are summarized. Chapter 4 describes the experiments on growth and characterization of thin films of Fe_3O_4. Chapters 4 and 5 comprise the results from applying the electrochemical lithiation process on Fe_3O_4 and CrO_2 and also models for explaining the same, based on the oxidation state of the cations. Finally, a summary of the thesis, with some ideas for future work, is presented in Chapter 6.

Chapter 2

Theory

In this chapter, the fundamentals of magnetism of transition metal oxides (TMOs) shall be reviewed. In section 2.1, the quantum mechanical derivation of magnetism of TMOs will be briefly reviewed and followed by a discussion of application of crystal field theory to these compounds. The limitations of the crystal field theory will be outlined, which leads us to a discussion of the Goodenough-Kanamori theory of magnetism in transition metal oxides. This will be followed by a discussion of the various kinds of exchange and superexchange interactions, which is crucial to an understanding of magnetic properties of these materials. There will also be a description of the application of Goodenough rules for predicting the ground state magnetic ordering in these compounds.

This will serve as the basis for understanding the magnetic properties of the two main materials that form the core of the thesis, namely Fe_3O_4 and CrO_2, which will be presented in sections 2.2 and 2.3. In the last section of the chapter, a theoretical overview of electrochemical lithium insertion and its relevance to the thesis will be presented.

2.1 Magnetism in Transition Metal Oxides

2.1.1 Introduction

Theory of magnetism in oxides is an extension of the application of quantum mechanics to a system of non-interacting and indistinguishable electrons, which is the simplest case for a multi-electron system. The origin of magnetism in metallic oxides can be explained as follows. Individual magnetic dipoles, which are created due to the moment of paramagnetic cations sitting on lattice sites, are coupled via quantum-mechanical exchange that causes the moments to be parallel or antiparallel to minimize the energy.

Unlike metals, where the moments are coupled by direct exchange, in oxides, superexchange plays an important role with the p-orbitals of the diamagnetic oxygen anions acting as intermediaries. This is because the metallic cations are typically too far apart for direct exchange. The saturation moment at absolute zero, when the system is at its magnetic ground state, is then determined by the moments of the individual dipoles and the strength and sign of the exchange interactions. The ordering temperature is dependent on the strength of the exchange interactions.

The magnetic moment of individual dipoles is decided by the electronic configuration of the cations. The sign of exchange interactions are a result of the interplay of electronic configuration of the cations and the bond angles between them. The strength of the exchange interactions is determined by the bond distances and the number of nearest neighbors. The relative strengths of the exchange interactions between cations of different coordination are particularly important in deciding the preferred ground state in systems with geometric frustration, where the system has ground state degeneracy. In the case of oxides, the wavefunctions are localized and atom-like, and this permits a simplistic treatment compared to metals.

2.1.2 Crystal Field Theory

Crystal field splitting is an important phenomenon that is central to understanding of magnetic behavior of various systems, especially ionic solids. It is central to the understanding of transition metal oxides, whose bonding is significantly ionic in character. Crystal field theory is an ionic bonding model that was developed to explain the properties of metal ions in crystal lattices. It explains many of the basic features of transition metal compounds, including their magnetic properties.

The distribution functions of the d-orbitals of the metal ion are shown in Figure 2-1.

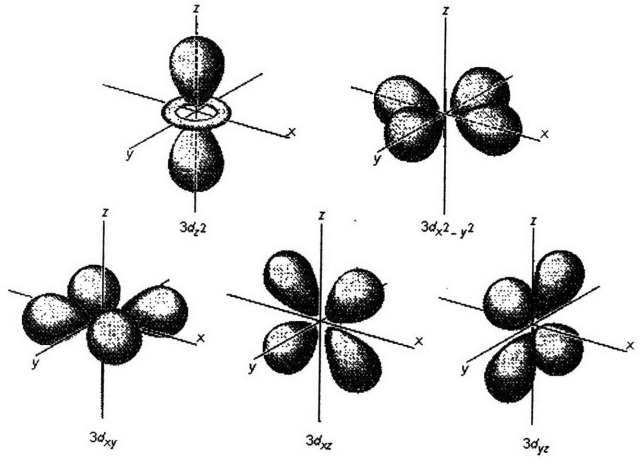

Figure 2-1: Spatial distribution of different d orbitals [1]

Crystal Field Theory assumes that the magnetic electrons in oxides are well-localized and that they are not subject to hopping or do not have an itinerant character. In cubic crystals, crystal field theory predicts that the presence of the ligands leads to a partial removal of the degeneracy due to electrostatic effects and a split in the d-orbitals as shown in Figure 2-2 (for the octahedral case) and Figure 2-3(for the tetrahedral case)[1]. Crystal field splitting energies are usually of the order of 1 eV. This is easily explained by considering the example of the octahedral site. Two of the d orbitals, d_z^2 and $d_{x^2-y^2}$ point in the direction of the oxygen ions, and therefore experience a greater electrostatic repulsion than the other three orbitals. This causes a split of the d-orbitals as shown in Fig. 2-2 . A similar argument can also be used

to explain the tetrahedral splitting. The interplay between crystal field splitting and

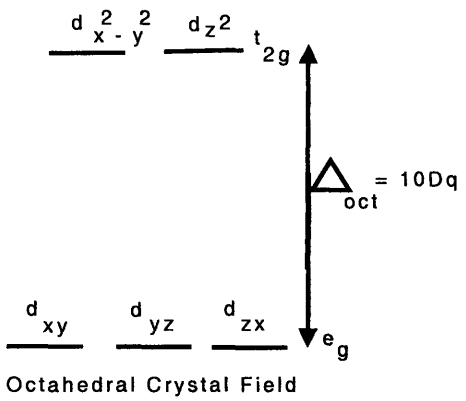

Figure 2-2: Octahedral Crystal Field Splitting

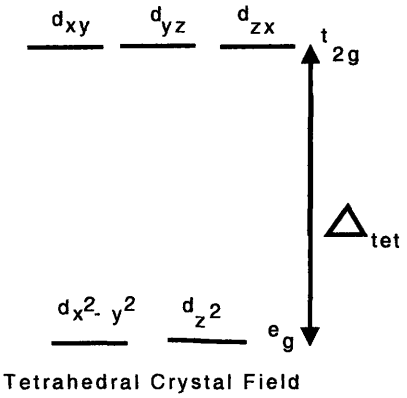

Figure 2-3: Tetrahedral Crystal Field Splitting

exchange energy Δ E_{ex} gives rise to an interesting possibility. If Δ E_{ex} >10 Dq, then the low spin state is stabilized and Hund's rule breaks down. This has been exploited in the development of spin transition materials which rely on using pressure or light to create high spin-to-low spin transitions [9, 10].

In non-cubic (lower symmetry) systems, there can be further splitting of the e_g and t_{2g} orbitals. For example, in tetragonal systems, the t_{2g} orbitals are split into twofold-degenerate and non-degenerate levels, and the e_g orbitals are also split into two. Due to such symmetry considerations, the analysis of ground state magnetic properties of non-cubic crystals is more complicated.

Furthermore, as outlined in the following sections on the Goodenough-Kanamori theory, the assumption of electron localization is not entirely true of metallic oxides. A notable example is in the case of CrO_2, which would be discussed in subsequent sections. Also, there are several other sources of the splitting other than pure electrostatic effects. Covalent mixing is one of the principal effects, which contributes to a much larger split in the d states compared to electrostatic effects in many cases [19].

2.1.3 Goodenough-Kanamori Theory

Traditional band theory satisfactorily explains the behavior of delocalized electrons such as outer s and p electrons. This is accomplished by using the standard Hartree-Fock hypothesis which reduces the many-body problem to the more tractable problem of a single electron in a periodic potential, which is then solved and combined through the Slater determinant [19]. This theory yields the direct exchange energy or potential exchange energy:

$$J\,\Phi_i = \sum_{j=1}^{N} \Phi_i^*(1)\Phi_j^*(2)[e^2/r_{12}]\Phi_i(2)\Phi_j(1) \qquad (1)$$

where Φ_i and Φ_j are one-electron wave functions, e is the electronic charge and r_{12} is the distance between electronic spins [19].

However, such a treatment fails to adequately explain the magnetic and electronic properties of TMOs, since this would involve description of more tightly bound d electrons and assuming fully delocalized electrons in this case is an oversimplification. Band theory also does not satisfactorily take into account electron (Coulomb) correlations between electrons of opposite spins on adjacent lattice sites. Crystal field theory, on the contrary, assumes that the electrons are fully localized at the atomic cores [19]. Outer 'f' electrons are the most tightly bound and screened from neighboring nuclei by s and p core electrons, and can be described by localized electron model. However the outer d electrons, such as those in TMOs, are intermediate in character and therefore in some transition metal oxides the outer electrons can exhibit the properties of localized electrons, and in some others, they can exhibit the properties of collective electrons [19]. This complicates the picture, because traditional band

theory and crystal field theory cannot be used without modification.

There are two kinds of metallic oxides. The first category of oxides have a large cation-cation interaction due to small cation-cation separations. In these transition metal oxides, the d electrons behave in a localized manner. This is true of most 3d transition metal oxides. This is why most of these are insulators, and this also enables a simplistic treatment of magnetism in these through superexchange and crystal field theory [19]. The other class of oxides have large cation-anion-cation interactions due to covalent mixing of cationic d and anionic p orbitals. In these oxides the electrons behave in a collective manner. There are a few oxides in which both mechanisms coexist. The Hubbard model attempts to explain this intermediate regime by discarding the Hartree-Fock assumption, starting with the many-electron Hamiltonian and adding interaction terms into it, which take into account interactions only among electrons of opposite spins on the same lattice site [19].

2.1.4 Energy Minimization

The ground state of a many-electron system is one that minimizes the total energy of the system, which comprises the kinetic energy, the potential energy, the Coulomb repulsion energy, the Hartree-Fock term and the exchange interaction terms [19]. The direct exchange energy term includes accidental electron correlations between electrons of the same spin that arise out of Pauli's exclusion principle. Since the sum of all the other energies other than the correlation energies and the Hartree Fock term are small reductions to the positive Coulombic term, this means that for energy minimization, the potential energy term should be as large as possible [19]. The potential energy increases with increasing localization, while the kinetic energy term shows the opposite trend. Depending on the strength of the interaction between the cations, one dominates over another, and the electrons can behave in either localized or collective ways [19].

2.1.5 Indirect exchange or "Superexchange" Energy

The interaction between any two spins (or ions that produce the spins) in an oxide lattice is essentially through an indirect exchange mechanism involving the intermediate anion. This is most easily observed in rocksalt-structured compounds like FeO and MnO, wherein nearest neighbors are coupled parallel or antiparallel to each other, but next nearest neighbors are always coupled antiparallel. These ions are too far apart to participate in Heisenberg exchange through a direct overlap of wavefunctions, and the coupling between such ions has to be via an indirect or mediated exchange mechanism.

2.1.6 Double Exchange

The above discussion on superexchange can be extended to the case of non-integral number of electrons per atom per partially filled band. This was first described by Zener, and was given the term 'double exchange'. This was derived from the results of the tight binding approximation. This mechanism involves hopping of electrons of minority spin on a lattice of electrons with opposite spin (Fig. 2-4). This typically occurs in mixed valence systems with half-filled or greater than half-filled orbitals [19].

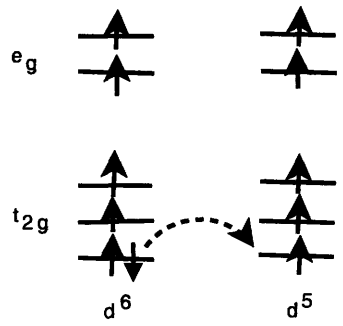

Figure 2-4: An illustration of double exchange

From the above discussion, it is clear that regardless of whether the electrons are itinerant or not, one can distinguish between two kinds of indirect exchange mechanisms, correlation and delocalization.

2.1.7 Correlation Superexchange

Also known by the term 'semicovalent' exchange, this mechanism takes into account the simultaneous partial bond formation ($p\sigma$ or $p\pi$) on each side of the anion that is in between two cations, and arises because the magnetic electrons are not totally independent as is assumed in the Hartree Fock theory, and are in fact correlated. In the traditional Hartree-Fock analysis, Fermi correlations are taken into account, which prevents electrons of the same spin to exist at the same spatial coordinates. However, Coulomb correlations, which are a result of Coulomb repulsion between electrons are neglected. These correlations are important in the analysis of TMO systems [19].

2.1.8 Delocalization Superexchange

This interaction arises due to drifting (or "hopping") of an electron from one cation to the other through the anion intermediary. The anion plays a significant role in the case of 180^o cation-anion-cation bond angles, as it helps along the hopping electron. In 90^o bond angles, the role of the anion is less obvious and there is more overlap of the orbitals of the cations, and therefore the direct exchange mechanism may become significant.

The following sections describe application of Goodenough's theory, described above, to explain the magnetic properties of Fe_3O_4 and CrO_2, which are listed in Table 2.1 [19].

Table 2.1: Some Physical Properties of Selected Transition Metal Oxides. R_{cc} is the intercationic separation and R_c is the 'critical' intercationic separation.

	Structure	R_{cc}(Å)	R_c	T_t (°K)	Magnetic	Transport
Fe_3O_4	Spinel	2.97	2.95	850K	Ferri. μ_{Fe}=4.1μ_B	Half-metallic
γ–Fe_2O_3	Spinel	2.94	2.58	856	Ferri. μ_{Fe}=2.5μ_B	Insulator
CrO_2	Rutile	2.92	2.86	392	Ferro. μ_{Cr}=2μ_B	Metallic

2.2 Magnetism of Fe_3O_4

Figures 2-5, 2-6, 2-7 and 2-8 show the unit cell of the spinel structure and the structure when viewed along the different crystallographic axes. As described

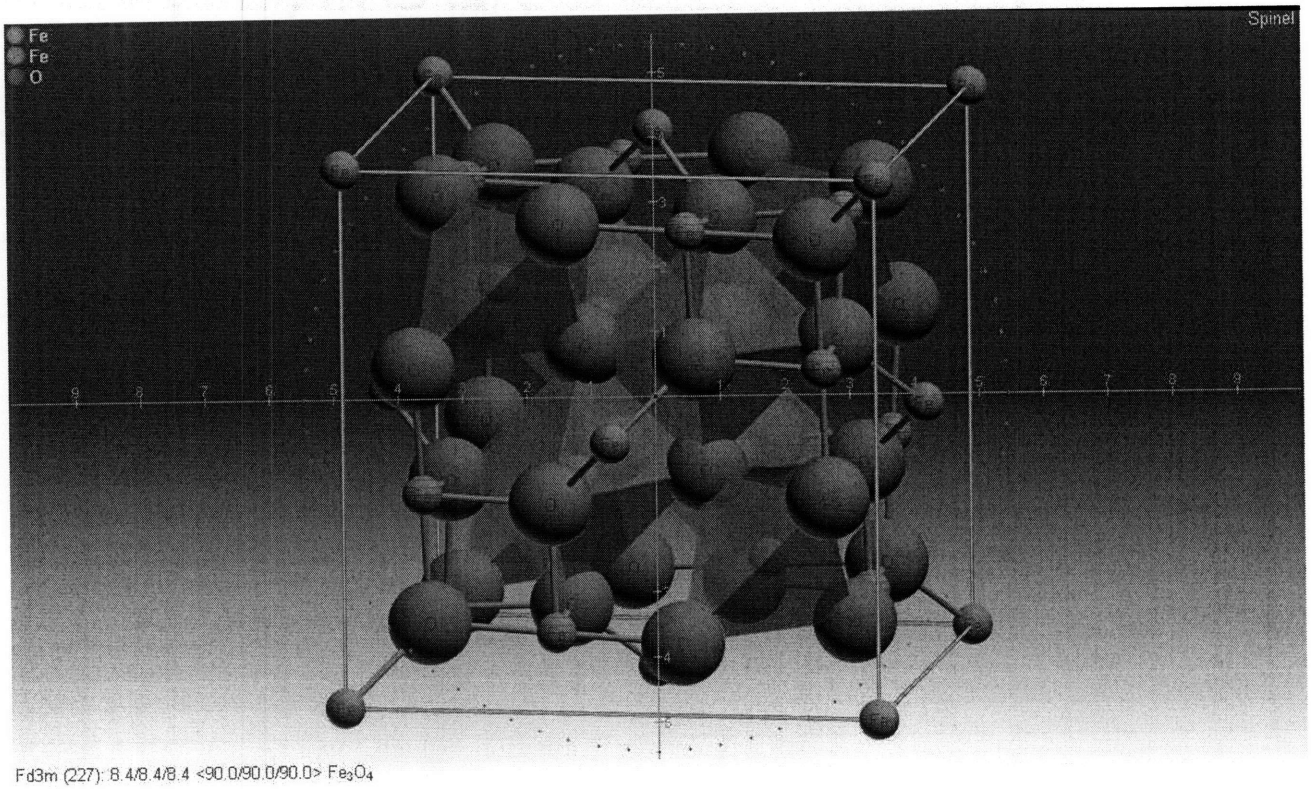

Figure 2-5: The spinel structure

earlier, the ferrimagnetism of Fe_3O_4 is due to antiparallel alignment of the tetrahedral (A) and octahedral (B) site cations on the spinel lattice as shown in Figure 2-5.This is the magnetic ground state which can be arrived by application of the rules outlined (please refer to the appendix).

If we write out the formula of magnetite in detail, it is: $(Fe^{3+})_A(Fe^{2+}Fe^{3+})_BO_4$. The B-O-B bond angles are 90 degrees, while the A-O-B bond angles are 125 degrees, and there are no A-O-A bonds. The interactions that need to be considered are d^5-d^5, d^5-d^6 and d^6-d^6, shown schematically in Figs. 2-9, 2-10 and 2-11 for 90 degree direct exchange interactions, where the role of the anion is not so significant. The superexchange interactions between d^5-d^5, d^5-d^6 and d^6-d^6 ions are summarized

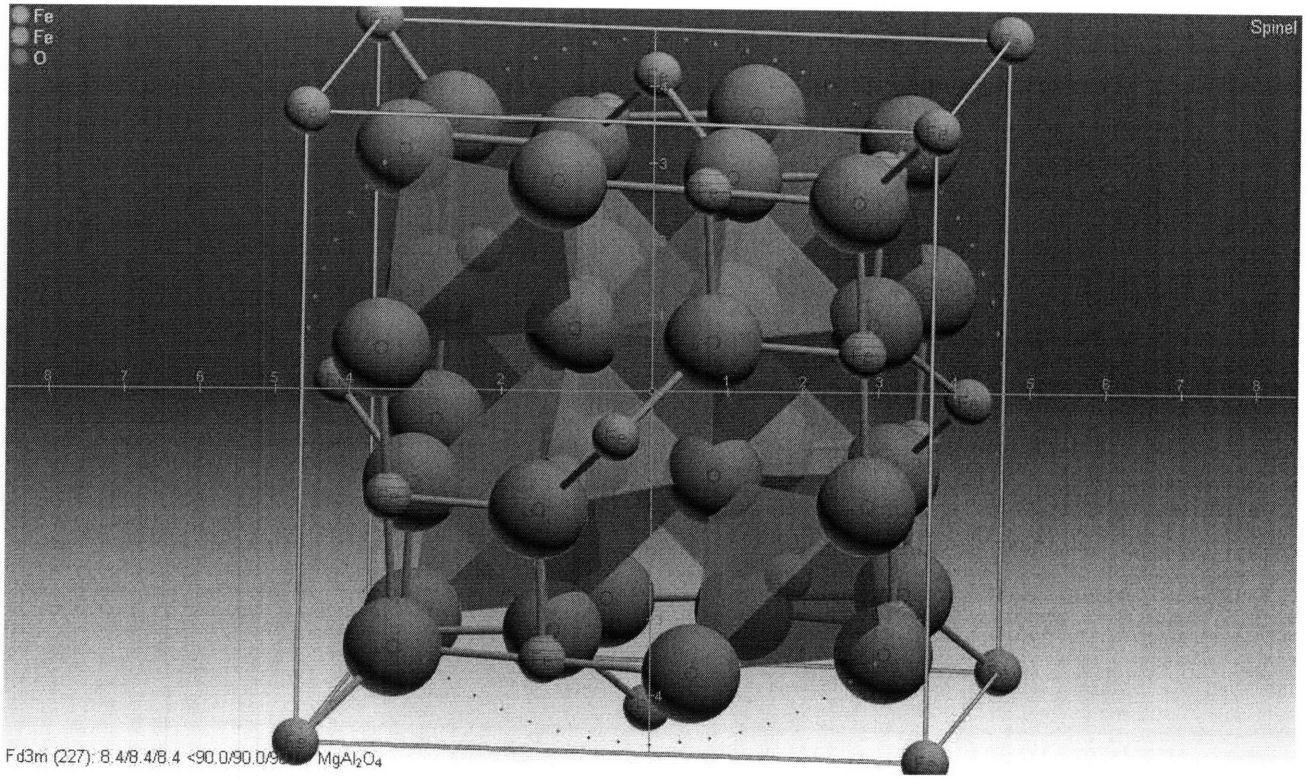

Figure 2-6: The spinel structure looking along [100]

in Table 2.2 [21]. Above the Verwey transition, which involves a large change in

Table 2.2: d^5-d^5, d^5-d^6 and d^6-d^6 superexchange interactions for 180 and 90 degree bond angles

Bond Angle	Mechanism	Orbitals	Interaction
180°	Correlation	e_g-pσ-e_g	Strong AF
180°	Correlation	t_{2g}-pπ-t_{2g}	Weak AF
180°	Delocalization	e_g-pσ-e_g	Strong AF
180°	Delocalization	t_{2g}-pπ-t_{2g}	Weak AF
90°	Correlation	e_g-s-e_g	AF
90°	Correlation	e_g-pσ-pπ-e_g	AF
90°	Correlation	t_{2g}-pσ-pσ-t_{2g}	Strong FM
90°	Delocalization (direct)	e_g-e_g	Weak AF
90°	Delocalization (direct)	t_{2g}-t_{2g}	AF except d^5-d^6 (strong FM)
90°	Delocalization (direct)	e_g-t_{2g}	AF

resistivity, there is hopping of electrons between Fe^{2+} and Fe^{3+} ions and this gives rise to the conductivity of magnetite through electronic exchange due to charge disorder.

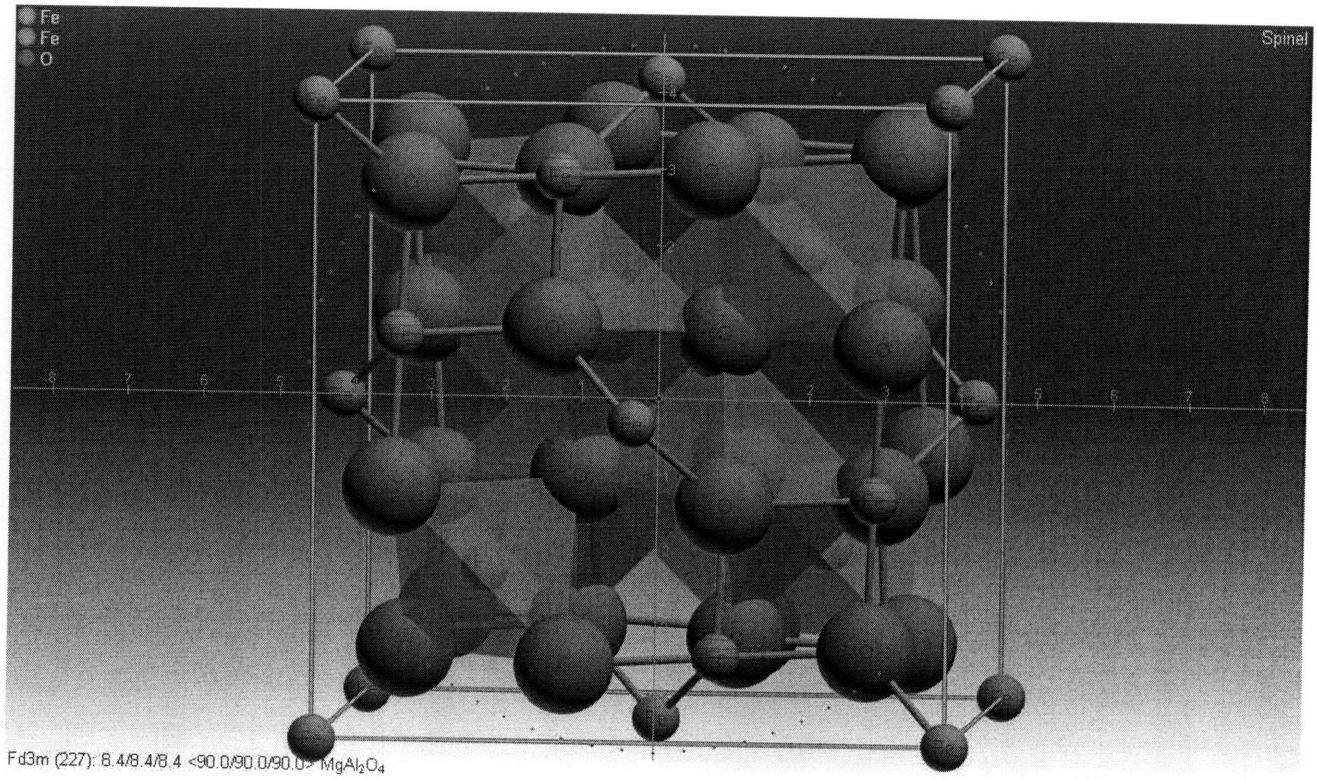

Figure 2-7: The spinel structure looking along [010]

This means that the situation shown in 2-4 comes into play, and this gives rise to ferromagnetic B-B ground state [21]. Below the Verwey transition, all the three interactions would have to be taken into account.

These interactions would be dominant especially for 90 degree bond angles, where direct cation-cation overlap would be large. Therefore it is valid for B-O-B interactions in spinel. However for bond angles greater than 90 degrees, the anion plays a much bigger role and superexchange mechanisms such as those described in the above table need to be considered [21].

Therefore, for temperatures above the Verwey temperature but below the Curie temperature, A-B interactions in Fe_3O_4 turn out to be strongly antiferromagnetic due to superexchange, while B-B interactions are weakly ferromagnetic. Therefore the magnetic ground state is one in which the A site ions couple parallel to each other, and are antiparallel to the B site ions, which are coupled parallel to each other

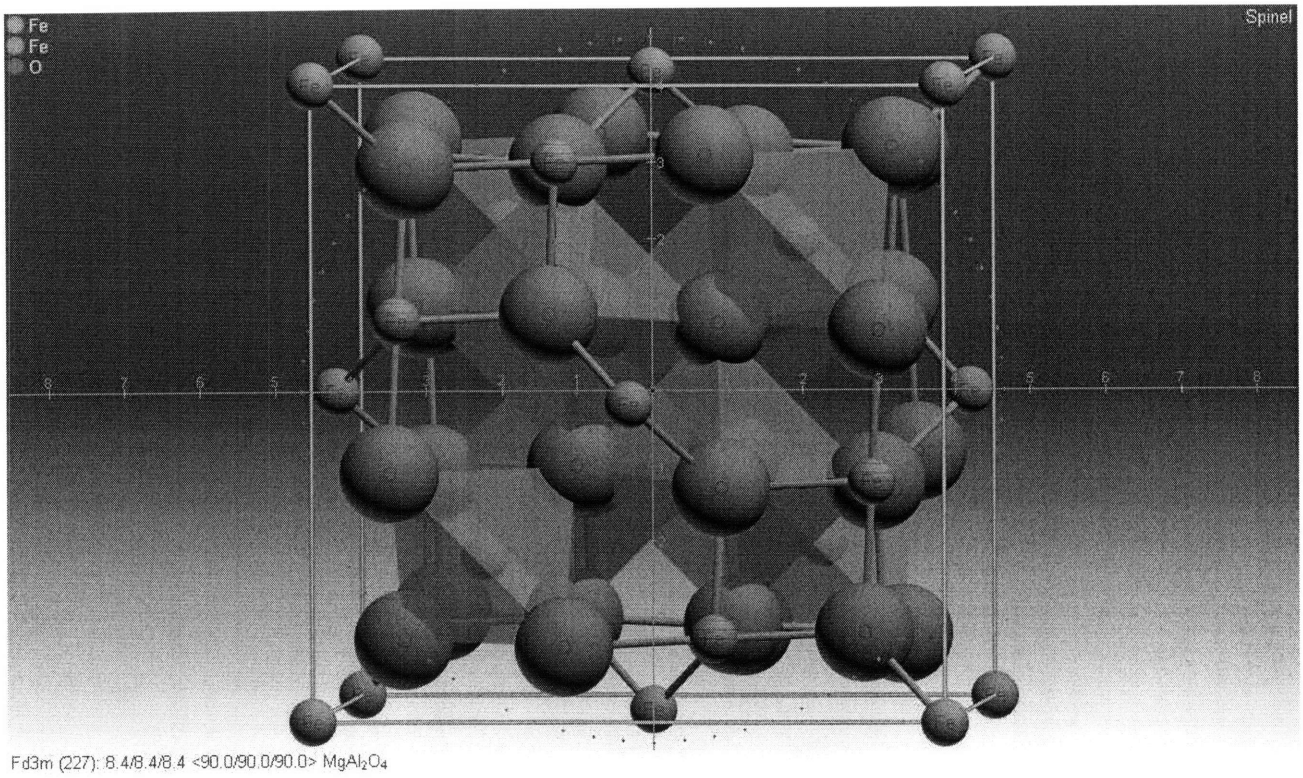

Figure 2-8: The spinel structure looking along [001]

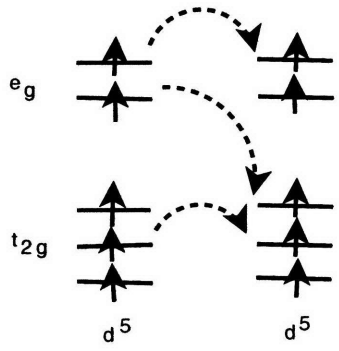

Figure 2-9: Fe^{3+}-Fe^{3+} hopping in Fe_3O_4 (All hopping scenarios favor antiparallel alignment of spins)

amongst themselves. This results in the ferrimagnetism of Fe_3O_4 [19].

Finally, a note about ab-initio (GGA+U) calculations on $Li_xFe_3O_4$ ($0<x<2$). These have shown that degenerate magnetic ground states ($\triangle E \sim 1$ meV at 0K) exist for $LiFe_3O_4$. For $Li_2Fe_3O_4$, the ground state magnetic moment is zero [22].

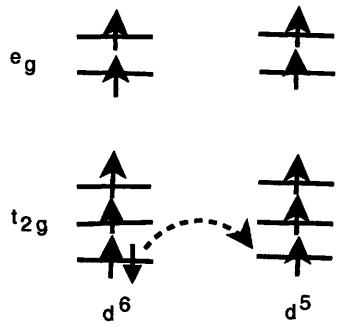

Figure 2-10: Fe^{2+}-Fe^{3+} hopping in Fe_3O_4 (Leads to ferromagnetic exchange due to hopping of minority spin)

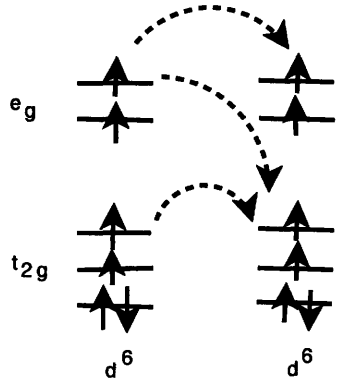

Figure 2-11: Fe^{2+}-Fe^{2+} hopping in Fe_3O_4 (All hopping scenarios favor antiparallel alignment of spins)

2.3 Magnetism of CrO_2

CrO_2 is a half-metallic ferromagnet with the rutile structure ($P4_2/mnm$ space group, c/a=0.6596) in which the octahedrally-coordinated Cr^{4+} spins are coupled parallel to each other on a tetragonal lattice [23]. In CrO_2 , half of the octahedral sites are occupied by Cr^{4+} ions. The Cr^{4+} ions form a set of edge-sharing octahedra along the c-axis and a set of corner-sharing octahedra along the a- and b-axes (Figures 2-12, 2-13, 2-14).The ferromagnetism of CrO_2 is a result of parallel coupling between localized t_{2g} electrons due to double exchange between electrons in the quarter-filled π^* band [19]. This ferromagnetic interaction dominates over the antiferromagnetic superexchange interaction between the localized t_{2g} electrons because of the lifting of

degeneracy due to tetragonal symmetry [19]. The electronic and magnetic properties

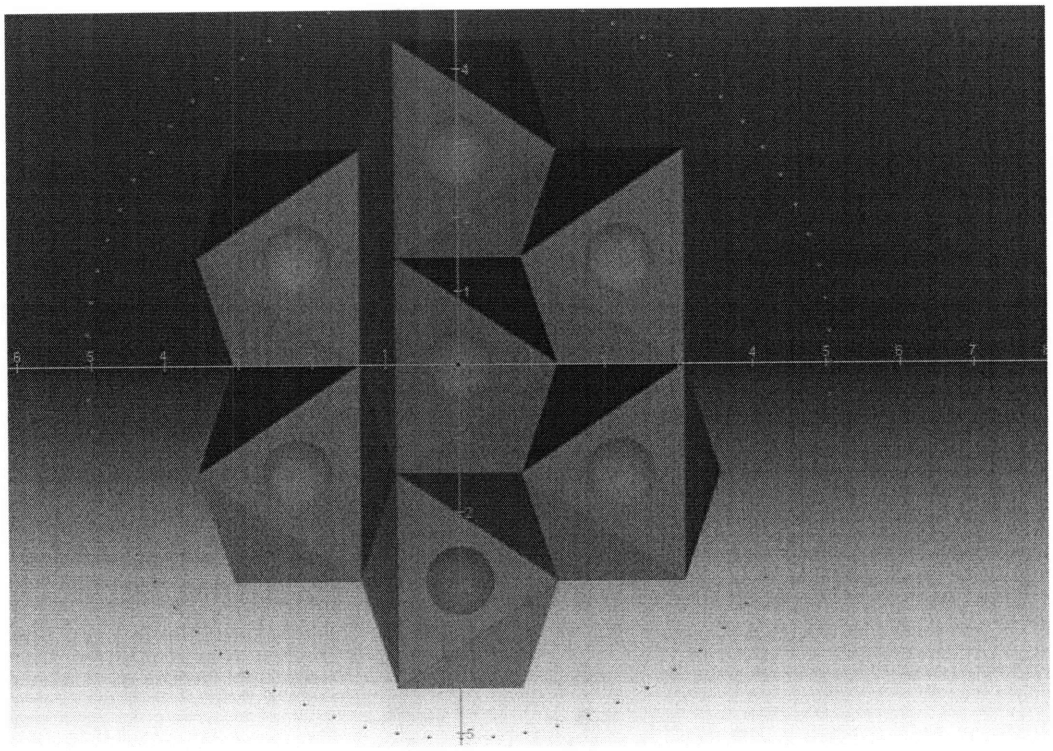

Figure 2-12: The rutile structure, looking along [100]

of CrO_2, and its half-metallicity are because the Cr d bands are divided into two sub-bands [12]. The first sub-band is a weakly interacting localized d state below the Fermi level. These d states provide the local atomic moments. The other band is a hybridized d band close to the Fermi level which provides metallicity. This is the source of the half-metallicity of CrO_2. It is unlike metals like Cu or Cr where conduction electrons are s electrons that are highly delocalized and thus free to move through the lattice, or in Co and Fe where the atoms are located close enough for the electrons in the d- bands to hop from atom-to-atom due to significant overlap.

The electronic and magnetic properties of CrO_2 and its half-metallicity have been well studied [12]. The spin polarization of CrO_2 measured by Andreev reflectometry is in the range 80-97%. This is because the metallic d sub-band consists of parallel spins, while the other sub-band is empty, and thus theoretically CrO_2 is expected to have complete spin polarization at the Fermi level.

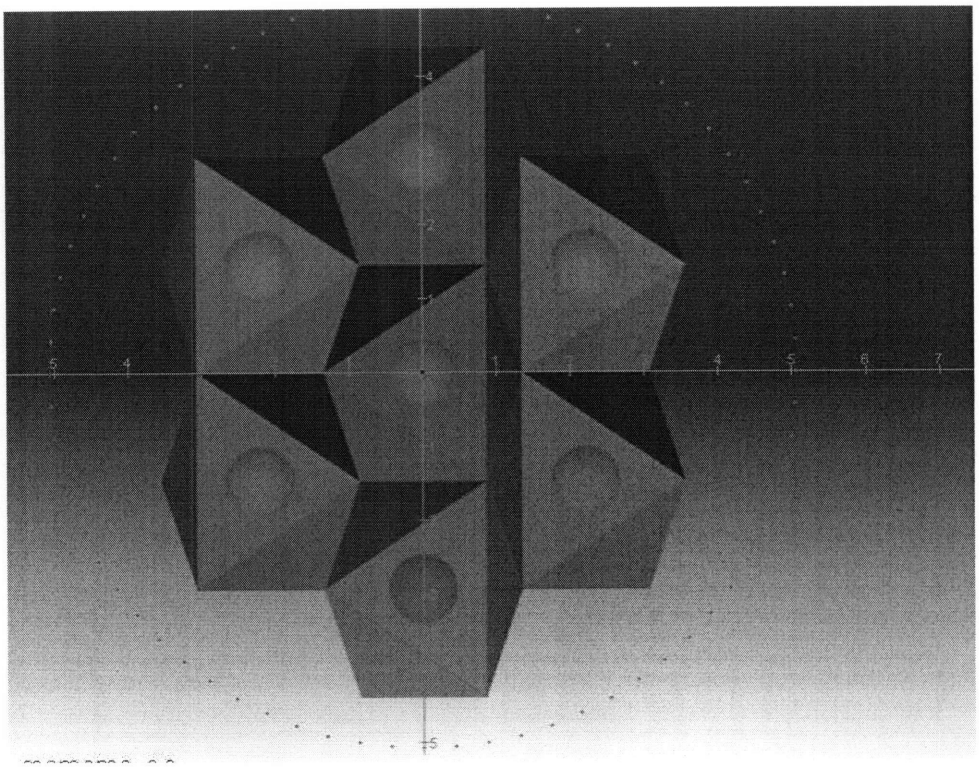

Figure 2-13: The rutile structure, looking along [010]

The ferromagnetism of CrO_2 has been intensively studied [12, 13, 14, 15, 16, 17, 18, 19]. It is very unique for a transition metal oxide. Most transition metal oxides have highly localized d states that make them insulators. In CrO_2, however, due to its half-metallicity, the conduction electrons belong to a delocalized (or partially localized) d- sub band. Thus, in CrO_2, the atom-like character of the metallic d-sub band and the presence of the oxygen framework leads to interesting effects. It is proposed that unlike metals, where the delocalization of electrons leads to the ferromagnetic ground state due to exchange energy stabilization, in CrO_2, the conduction electrons are not delocalized but 'itinerant', which means that the electron-electron repulsion Hamiltonian is large enough to keep the electrons localized around the individual cations. Furthermore, the cations are farther apart than they would be in a metal because of the presence of the anion framework. Therefore, it is a double exchange mechanism via the intervening oxygen anions that contributes to the magnetism of CrO_2 [18].

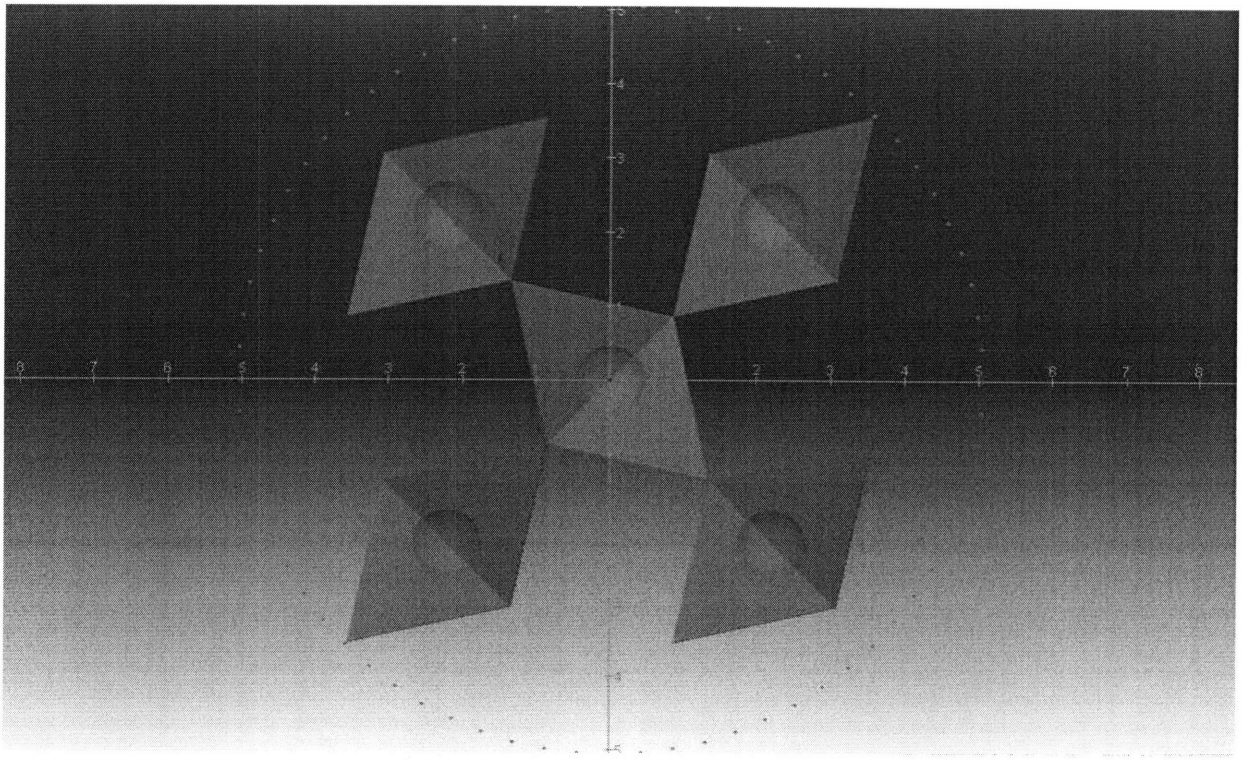

Figure 2-14: The rutile structure, looking along [001]

In CrO_2, the interactions that need to be considered are the d^2-d^2 90 degree interactions, since the bond angles are 80 degrees and can be approximated to 90 degrees for the purposes of analysis. Since the e_g orbitals are empty, the t_{2g}-t_{2g} interactions alone need to be considered. As described above, direct cation-cation interactions are the most important in bond angles that are close to 90 degrees. In CrO_2, there is lifting of the degeneracy of t_{2g} orbitals as shown in Figure 2-15. This simplifies the picture, because the localization of one of the d^2 electrons in t_{2g} gives rise to only one possibility, that of hopping of the electron in t_{2g}^*, which is part of the π^* band, into the orbital of the neighboring ion. The situation would be different if the ions involved were d^3 ions, such as Cr^{3+}. In this case, out of the possible scenarios for hopping, only some are energetically favorable. These scenarios can lead to competing alignment tendencies for neighboring spins, as shown in Figures 2-16 and 2-17, and as will be further explained in Chapter 5. In such a situation, the alignment which leads to energy minimization upon most number of hopping scenarios can be regarded

as the magnetic ground state.

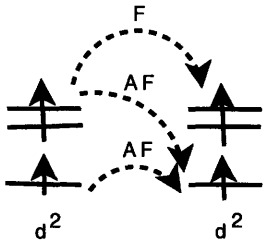

Figure 2-15: $Cr^{4+}(d^2)$-$Cr^{4+}(d^2)$ itinerant electron hopping in rutile

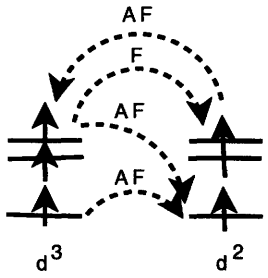

Figure 2-16: $Cr^{3+}(d^3)$-$Cr^{4+}(d^2)$ itinerant electron hopping in rutile

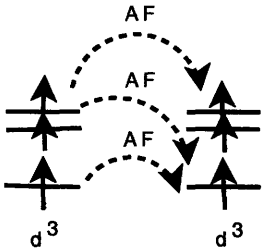

Figure 2-17: $Cr^{3+}(d^3)$-$Cr^{3+}(d^3)$ itinerant electron hopping in rutile

2.4 Electrochemical lithiation: Thermodynamics, Kinetics and Mechanisms

In this section, the basic concepts of lithiation will be reviewed, with the example of $LiCoO_2$ from the literature, which serves the purpose of illustrating the mechanism

of lithium diffusion [24, 25].

The fundamental driving force for Li diffusion is a difference in chemical potential and not the concentration (as predicted by Fick's law). The equilibrium voltage, defined by the difference in electrochemical potential of Li between anode and cathode, is the open circuit voltage [24].

$$V(x) = \frac{(\mu_{Li}^{cathode}(x) - \mu_{Li}^{anode})}{zF} \quad (2)$$

where $\mu_{Li}^{cathode}(x)$ is the electrochemical potential of the cathode (function of lithium content), μ_{Li}^{anode} is the electrochemical potential of the anode, z = Ionic charge of the anodic metal (1 for Li), and F = Faraday's constant = 96485 C.

As Li is intercalated, the chemical potential difference between anode and cathode decreases, and this leads to a decrease in the voltage. The chemical diffusion coefficient D_c, that is often reported in the literature, is different from the self diffusion coefficient:

$$D_c = \theta D_j \quad (3)$$

where θ is a thermodynamic factor that takes into account the deviation of the chemical potential of Li from that of an ideal solution [24]:

$$\theta = \frac{\frac{\partial \mu}{kT}}{\partial \ln x} \quad (4)$$

D_j is like the self/tracer diffusion coefficient, but it also includes correlations between Li ions.

Li_xCoO_2 is a well-studied cathode material for lithium batteries. It crystallizes in the layered ($NaFeO_2$) hexagonal structure, in which Li and Co ions occupy alternate sheets between layers of oxygen ions. In Li_xCoO_2, there are two possible mechanisms for migration into adjacent octahedral sites - Oxygen Dumbbell Hop (ODH) and Tetrahedral Site Hop (TSH), depending on whether the target site is a single vacancy or an associated vacancy (such as a divacancy) respectively [24]. The activation energy is much lower for the TSH (0.23-0.6 eV vs 0.8 eV) than ODH. First-principles electronic structure methods and Monte Carlo simulations have been used to predict the dominant diffusion mechanism. These calculations take into account both thermodynamic considerations (Li-Li interactions) and kinetic factors (eg. activation barriers). These studies have shown that ODH will dominate only at infinite dilution

of vacancies (x close to 1). In real systems, there are always vacancies, so the TSH mechanism almost always dominates [24].

Motohashi et al recently demonstrated synthesis of the fully delithiated compound, CoO_2, via electrochemical oxidation and measured its magnetic properties [25]. They showed that the CoO_2 phase consists of triangular lattice layers of CoO_2 stacked one on top of another, and suggested that CoO_2 is a Pauli paramagnetic metal with itinerant electrons [25]. This literature will be compared to results obtained for CrO_2 in Chapter 5.

The above discussion can also be extended to be applicable for most lithium transition metal oxides with the layered structure. Figure 2-18 shows the variation in activation energy barrier for Li ion migration for different lithium transition metal oxides [2]. It is clear that going towards the right in the d transition metal series increases the activation energy barrier and thus decreases Li ion mobility. Research has

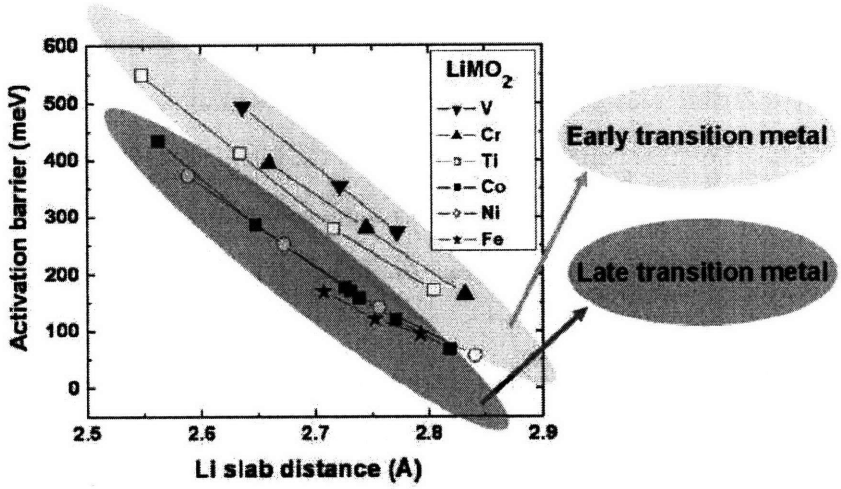

Figure 2-18: Calculated Activation Energies for various layered lithium transition metal oxides [2]

been done on the effect of substitution of non transition metal cations, in particular, on Li ion mobility and rate capability. It has been found that the most important factors for the activation energy (or migration) barrier and thus Li ion mobility is the Li slab distance (c-axis lattice parameter), which determines the compressive stresses

experienced by Li in the intermediate tetrahedral site, and the electrostatic repulsion between the Li and the transition metal cation in that position [2]. It has been found that the latter can be reduced by substitution of lower valence cation, such as by substituting Ni into $LiMnO_2$.

Another factor that influences Li ion mobility is the nature of the vacancy network. Recently researchers have found that the olivine structure of $LiFePO_4$ provides a 1D pathway for Li diffusion and high rate capability suited for high power applications[26]. This means that there may be scope for high rate capability in the rutile structure which also has a 1-D channel along the c-axis, unlike the spinel, which has a 3D network of vacancies. The relevant literature will be discussed in Chapter 5.

There are certain crystal structures that show good reversible capacities for Li insertion. Apart from the layered structure, described above, the anatase, spinel and olivine structures have been considered to be good cathode materials and have been researched from this point of view [26, 27, 28]. Recently it has been shown that there is the possibility of using nanocrystalline rutile electrodes in high power lithium batteries [29, 30, 31]. Of the structures mentioned here, only the spinel and rutile structures are known to show room-temperature ferromagnetic and ferrimagnetic ordering, with saturation moments that are significant enough for practical applications involving such chemical tuning of magnetism.

Chemical and electrochemical lithiation studies have been done on Fe_3O_4 and γ-Fe_2O_3 powders [11, 32, 33]. These studies were done initially for the purpose of investigating the suitability of Lithium|Iron oxide cells for high temperature lithium batteries. These will be detailed in Chapter 4. There appears to be very few reports on Li insertion into rutile-structured CrO_2. The relevant literature will be discussed in chapter 5.

Chapter 3

Experimental Methods

3.1 Pulsed Laser Deposition

Pulsed Laser Deposition (PLD) is a physical vapor deposition technique that is widely used to grow oxide thin films. It is a method that is particularly suited for growing multicomponent oxides, and one whose popularity grew in the late 1980's accompanying the quest for high-T_c superconductors. The experimental setup for Pulsed Laser Deposition is shown schematically in Figure 3-1.The iron oxide films were grown using a pulsed laser deposition system that consisted of a Lambda Physik LPX 325icc laser with $\lambda = 248$ nm. The laser is focused onto the target surface using a lens and is scanned over the surface of the target to prevent uneven erosion.

Laser ablation is a multistep process, one that includes the following steps [34].

1. Absorption accompanied by formation of a molten layer (Knudsen layer) and vaporization (which exerts a large recoil force and ejects molten droplets)

2. Propagation of melt front

3. Formation of plasma containing atomic and molecular species

4. Receding melt front

5. Completion of solidification, until the next pulse arrives

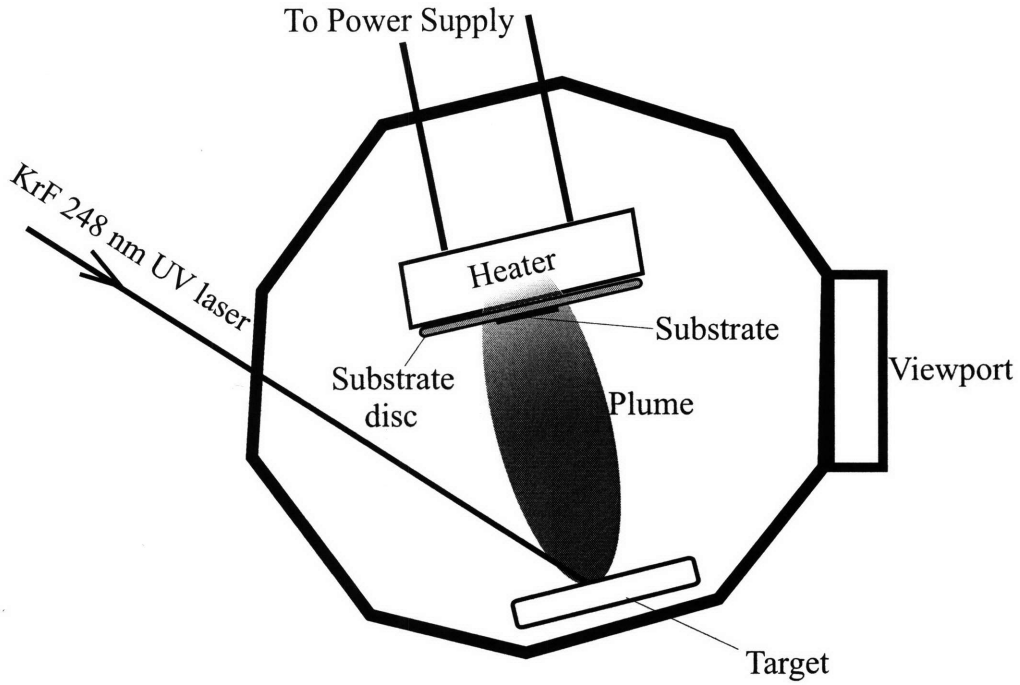

Figure 3-1: A Schematic of Pulsed Laser Deposition

6. Interaction of the laser with the plume.

Depending upon the fluence of the laser, these processes occur at the target to varying degrees. At the fluence levels that are typically used in PLD (1-5 J/cm^2), the melt depth is quite large, and significant vaporization also occurs simultaneously [34].

3.1.1 Process Variables/Parameters

There are several process parameters in PLD which can be used to control the deposition rate (the thickness of the film deposited per unit time, in nm/min) and crystallinity of the films. These will be described next.

1. Laser repetition rate: This is usually varied between 5 Hz and 100 Hz. The higher the laser repetition rate, the faster the deposition. The typical deposition rate in PLD is $\sim$ 10 Å/s. Also the roughness of the films is increased as higher repetition rates are used.

2. Chamber Pressure: The chamber pressure is controlled by the following two parameters:

    - Gas flow rate in sccm: The higher the flow rate of gas, the higher the pressure. This is usually kept between 1 to 10 sccm.
    - Gate Valve opening (%): For systems with gate valve control, larger opening leads to lower pressures.

3. The target-substrate distance: The larger the distance between the target and the substrate, the more collisions atomic and ionic species undergo before they reach the substrate, hence resulting in lower velocities and lower deposition rates. This is due to scattering of material in the plume preventing it from hitting the substrate.

4. Laser Energy (mJ): Higher laser energies can result in higher mobility of species adsorbed on the substrate due to higher laser fluence at the target surface, and thus better crystallinity and/or epitaxy.

5. Number of pulses: This can be used to control the thickness of deposited films, typically between 10,000 and 100,000.

6. Substrate Temperature: Since solid state diffusion is thermally activated, this can also have a substantial effect on mobility of adsorbed species and higher substrate temperatures generally result in better crystallinity. It is also often a critical parameter for phase control, since there could be unwanted phase transformations at certain temperatures.

3.1.2 Processing-Structure-Property Correlation

1. Crystallinity and epitaxy: In general, smaller crystallite sizes result from lower substrate temperatures and lower laser energies. As mentioned in the previous section, for good crystallinity and also for epitaxial growth, low deposition rates and high temperatures are usually required. Therefore, lower laser repetition

rates and higher substrate temperatures are desirable. The deposition rate is also higher in vacuum than in oxygen pressure, because the ablated species undergo fewer collisions, and because the plume shape is much narrower.

2. Growth of metastable phases: PLD is suited to grow certain metastable phases due to the non-equilibrium nature of the process. However, it is preferable to minimize the deposition and annealing times in order to achieve growth of such phases. An example is the growth of maghemite films by PLD, where it has been found that using high repetition rates enhances stability of maghemite through reduction of deposition time [35, 36]. Lower deposition rates lead to formation of the more stable hematite phase and reduction in magnetic moment. It is also important to limit substrate temperatures to less than 500 ^{o}C and to minimize annealing times for stabilizing the maghemite phase.

3. Stoichiometry: Obtaining the correct oxygen stoichiometry in oxide films is important to minimize the effects of oxygen vacancies and to obtain the correct valence state of cations. This requires using appropriate oxygen pressure which can be optimized empirically. Maintaining oxygen stoichiometry can be a problem especially for multicomponent oxides. In these cases, it is sometimes desirable to flush the chamber with oxygen to create higher pressures ($\sim$1 torr) for deposition. The oxygen pressure during cooling is also important. It is better to cool under oxygen pressure if the film has been grown in oxygen, or in vacuum if the deposition was in vacuum.

3.2 Vibrating Sample Magnetometry

3.2.1 Principle

Vibrating Sample Magnetometry has been one of the popular methods for magnetic measurements since its invention by Foner in 1955, partly due to its simplicity [37]. It is shown schematically in Fig 3-2.

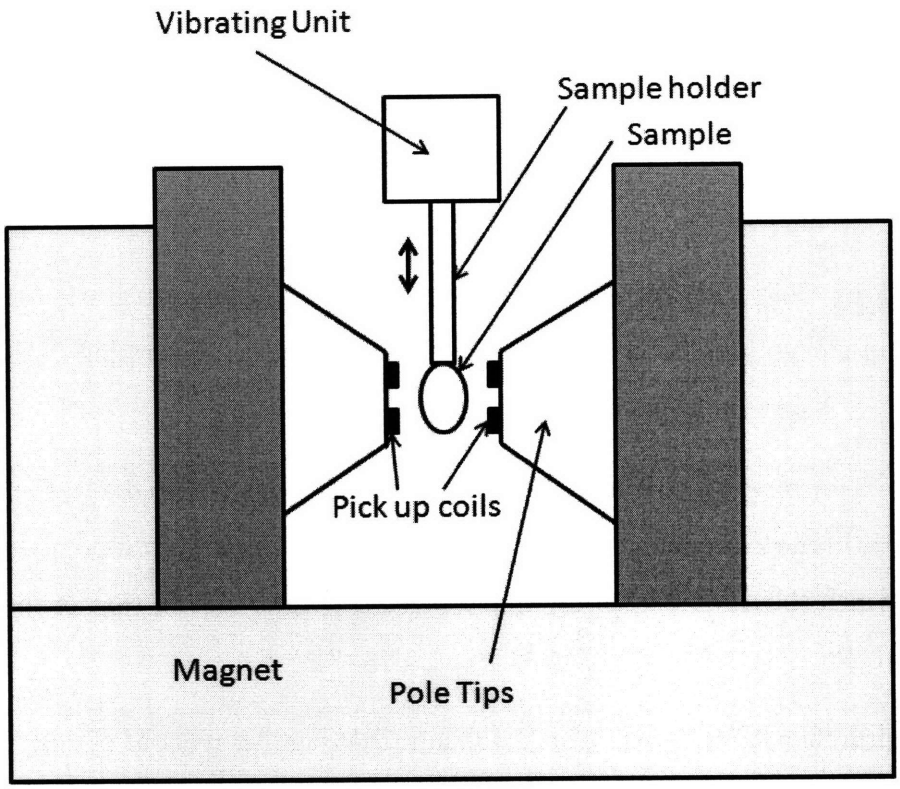

Figure 3-2: A schematic of Vibrating Sample Magnetometry

The operating principle of Vibrating Sample Magnetometry is Faraday's law of magnetic induction. The vibration of a sample placed in a magnetic field perpendicular to the direction of the applied field causes varying flux across the magnetized sample, and this induces a voltage in a set of pickup coils. This voltage is fed to a digital signal processor, and fed to a gain circuit, where it is amplified and converted into a reading of the magnetic moment by calibrating against a known standard. The VSM used for this thesis is the KLA Tencor/ADE Magnetics VSM 1660.

$$V = - N \frac{d\Phi}{dt} \tag{5}$$

where N is the number of turns in the pickup coils, and Φ is the magnetic flux.

3.2.2 Experimental Setup

The VSM in the Magnetic and Magnetoresistive Characterization Laboratory is designed for applied fields upto 1.3 T and for measurement temperatures in the range

100 to 900 K. It consists of the following components.

1. The Electromagnet: This consists of a set of copper coils wound around a magnetic iron core, and supplies the external magnetic field used to magnetize the sample.

2. Pick-up Coils: The VSM uses inductive sensing via flux integration through a set of pickup (detection) coils and an inductive sensor. The radius of the pickup coil, r, is an important quantity.

3. The Vibrating Unit: In the VSM 1660, the sample is vibrated at a frequency of 70 Hz in the z direction. Most conventional VSMs employ a transverse geometry, in which the sample is vibrated in a direction transverse to that of the applied field [38].

4. Digital Signal Processor: This is the unit that enables readout of magnetization values. It takes as input, the amplified signal from the pickup coils and factors in the pickup coil sensitivity for calculation of the sample magnetization.

5. Furnace: The furnace in the VSM is designed to go upto 900 K under a flow rate of 15-20 scfh of He.

3.2.3 Instrument Parameters

1. Gas Flow rate: The VSM 880 has a 1660 temperature controller that has facility of control of the sample temperature by heating up argon gas. Helium can also be used, but the lower heat capacity of argon enables better heating.

2. Coil Spacing: This is a very important parameter especially for optimizing the signal-to-noise ratio. This is particularly important for measurement of low moment samples. The signal can also be potentially improved by adding additional detection coils to the VSM. However, this method does not guarantee a better signal-to-noise ratio, because the thermal noise is directly proportional to the

volume of the coils, while the signal does not scale as rapidly [38].

3. Applied Field: The VSM 880 has a range of 13 kOe for the applied field. For applied fields close to the high range, smaller coil spacings may need to be used.

4. Pickup coil sensitivity: This is an important parameter that helps us keep track of changes in the system. In the normal mode of operation, with the coil spacing around 20mm, this would be between 30-70 emu/V. Large changes may indicate problems that may need to be resolved. The geometry of the setup and the pickup coils is such that the sensitivity is proportional to the number of flux lines per unit area, and this varies as the inverse square of distance from the pole pieces of the electromagnet. Therefore, for larger sized samples and for larger coil spacings, there will be significant changes in the sensitivity. Bowden found that the detection coil system could be setup to obtain a saddle point that is large (several millimeters) in spatial extent, thereby minimizing sample positioning errors and sample size effects, and this is ensured in most commercial VSM equipment [39].

5. Noise: There can be several sources of noise. There is usually significant drift in the gain circuit, which can be 0.5 to 1% in the VSM 1660. The two main types of noise from the hardware are the Johnson noise of the wire of the pickup coils and the field noise [37, 40]. Feldman et al have given the following expression for the signal-to-noise ratio:

$$\eta = (S/4kTR\partial v)^{1/2}\ \ S/R^{1/2} \qquad [41] \qquad (6)$$

Here S is the pickup signal, R is the resistance of the coil and ∂v is the bandwidth of the detector. The noise in any measurement can usually be minimized by increasing the number of averages per reading because it goes as the square root of the number

of averages. However, one should take care not to use too many number of averages. This has the drawback of increasing the drift and coherent noise of the system even though the random and incoherent noise is reduced. Typically, 30-50 averages are sufficient for most measurements.

3.2.4 Static and Dynamic Reproducibility

Static reproducibility refers to the accuracy in measurements of the same sample when measured twice without making any changes to the instrument setup. This is a function of the noise in the surroundings in addition to system noise, and is better when the vibration unit and the gain circuit have been warmed up by continuous use. It is recommended that the VSM be in operation for 4-5 hours to get good static reproducibility and to minimize drift of the gain circuit. The VSM 1660 has a static reproducibility of approximately 0.5%.

Dynamic reproducibility refers to the repeatability of a measurement once a sample has been taken out and placed back into the sample loading assembly. This is a function of the sample size and orientation. Since the error in sample positioning is larger for larger samples and for samples loaded in plane, therefore the dynamic reproducibility is also poorer in these cases, and is of the order of 1.5% for relatively large samples (>10mm Φ).

3.2.5 Shape, Orientation and Size Effects

Out of plane measurements are subjected to lesser sample positioning error, since the sample is placed farther away from the pickup coils than if it was in-plane. Also, generally there is lesser field non-uniformity in out of plane measurements. Ideally, the sample used for measurement should be ellipsoidal in shape, because that ensures uniformity of magnetization and magnetization fields, and well-defined demagnetization factors [38, 42]. However, this is not practically feasible. Instead, sample positioning errors in commercial VSMs are minimized by using a set of even numbered symmetric coils and by loading the sample at the saddle point of the sensitivity

function G (r) [38].

$$\partial^n G/\partial x^n = 0,\ \partial^n G/\partial y^n = 0 \text{ and } \partial^n G/\partial z^n = 0 \text{ for all odd n} \quad (7)$$

3.2.6 Error Analysis

In a well-calibrated measurement, the main sources of error are the static reproducibility error and sample positioning error. The latter can be minimized by performing the sample positioning calibration every time a sample is loaded for measurement. This becomes a difficult task for smaller moment samples due to the low signal-to-noise ratio. However, it has been reported in the literature that the differences in voltage sensed by the pickup coils are $\sim$ 1% for a sample that has been moved around 5mm away from the saddle point [39].

3.2.7 Curie Temperature Measurements

Curie temperature measurements of samples can be done either at remanence or at saturation. Although measuring samples at saturation helps in determining the temperature dependence of magnetization more accurately, if the aim of the experiment is to accurately determine the Curie temperature of a sample, the remanent magnetization state is more useful. This is because the effects of short range ordering of moments above the Curie temperature are canceled out if the measurements were done at zero applied field. The ADE VSM 1660 has a Model 883A temperature controller that enables control of temperature through the EasyVSM software through the "Temperature Scan" menu. The sample is loaded using alumina ceramic paste to the sample holder.

3.3 Electrochemical Lithiation

Figure 3-3 shows a schematic of the experiments.

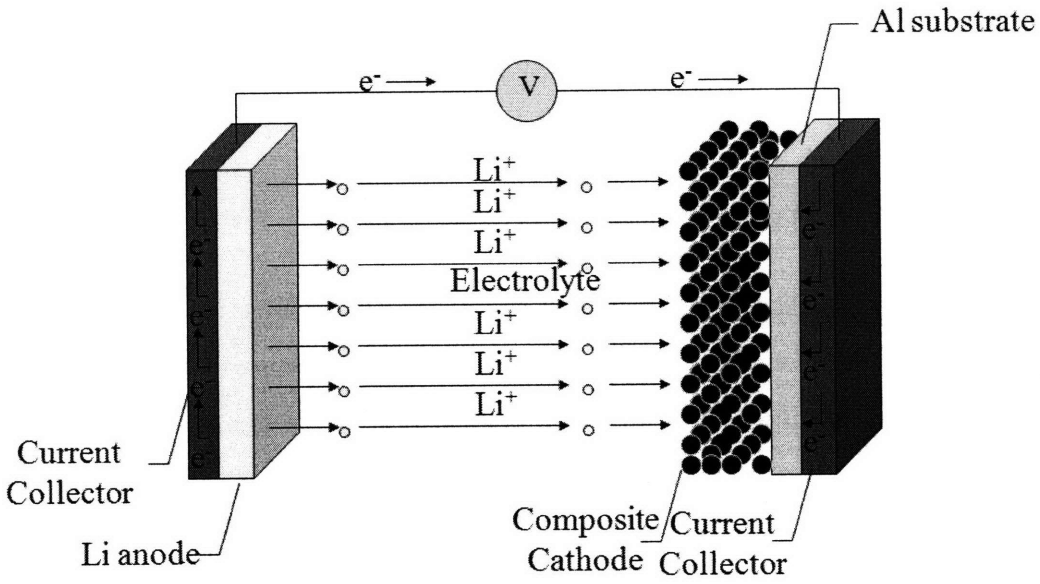

Figure 3-3: A schematic of the electrochemical lithium insertion process

3.3.1 Preparation of Porous Electrodes

For the experiments on nanoparticles and micron-sized powders, composite cathodes were used. The electrode slurry was prepared by mixing the active material (Fe_3O_4 or CrO_2) with appropriate amounts of conducting additive Super P carbon (TIMCAL inc.) and poly (vinylidene fluoride) (PVDF) binder in N-methyl pyrrolidone (NMP) solution. The slurry was cast onto an Al foil and dried in a vacuum oven overnight. The electrode disks (area = 1.77 cm^2) were punched and dried in a vacuum oven at 70 ^oC for 6 hrs before storing them in an argon-filled glove box (oxygen level less than 1ppm and water level less than 1.5ppm). For the experiments on PLD-grown thin films of iron oxide, the films grown on copper were used as cathodes instead of the porous composite cathodes described in this section.

3.3.2 Calculation of capacity and discharge currents

The gravimetric discharge capacity C (in mAh/g) is calculated from :

$$C=\frac{1000nF}{3600M} \quad [32] \quad (8)$$

where n = the number of Li ions that enter the structure per formula unit, F = Fara-

day constant = 95,600 Coulombs/mole, and M = molecular weight of the lithiated compound (in grams/mole).

The active weight of the electrode (weight of the film or that of the active material in the porous electrode) multiplied by the gravimetric capacity gives the electrode capacity in mAh. The weight for the PLD films was calculated by using the volume of the films assuming theoretical density. The current that has to be withdrawn during discharge can be calculated by dividing the electrode capacity by the time of discharge in hours. Here it is assumed that 1 equivalent of Li carries 1 C of charge.

3.3.3 Preparation of cells

Assembly of the cells in the glove box involved stacking layers of the Fe_3O_4 or CrO_2 and Li foil electrodes, and two pieces of Celgard separator in between (Celgard Inc, USA). 1M $LiPF_6$ in a 1:1 EC:DMC solvent (Merck, TECHNO, SEMICHEM Co. Ltd., Korea) was used as the electrolyte. A schematic of the cells used in the experiments is shown in Figure 3-4. The cells were allowed to rest overnight in the glove box before electrochemical testing.

3.3.4 Electrochemical schedules

These cells were subjected to electrochemical lithiation and delithiation via galvanostatic experiments at constant current in which they were discharged (i.e. Li^+ insertion into the cathode) and then charged (Li^+ de-insertion) at rates between C and C/100 using a Solaritron 1470 Battery Tester [43, 44]. A rate of C corresponds to an applied current of 'C' mA per gram of active material and is equivalent to the insertion of 1 mole of lithium ions per formula unit every hour. 'C' is also the theoretical capacity calculated in Section 3.3.2, assuming that the theoretical capacity corresponds to 1 mole of Li inserted into each formula unit of the structure. Similarly, a rate of C/10 implies that, with no kinetic limitations, it would take 10 hours to introduce 1 mole of Li^+ into each formula unit of the structure.

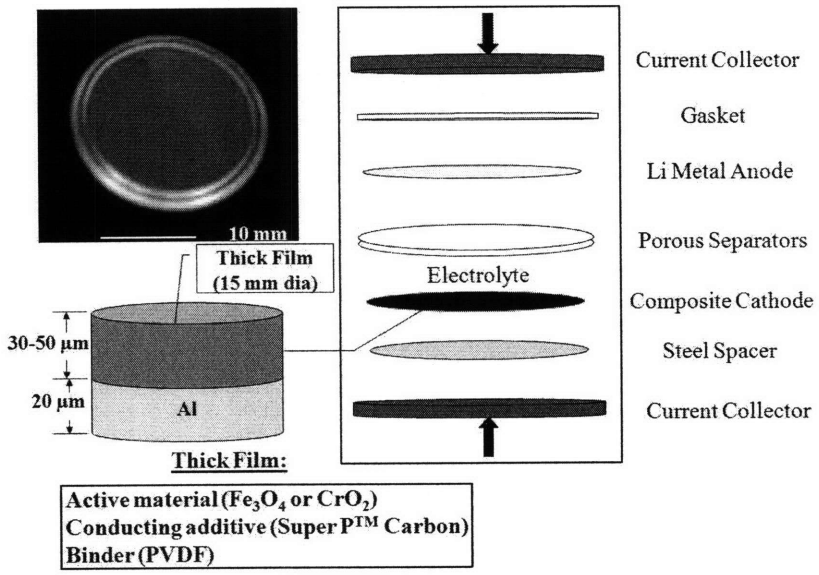

Figure 3-4: A schematic of the cell assembly

3.3.5 Disassembly of cells

At the end of discharge, the coin cells are uncrimped within the glovebox and the electrolyte is washed off with solvent (DEC) to remove $LiPF_6$ so that the formation of HF when the lithiated sample comes into contact with the atmosphere is avoided. For some samples, magnetic measurements were obtained at different time intervals after lithiation, to see the effects of exposure to atmosphere.

3.3.6 Structural and Magnetic Characterization

The films and nanoparticles were characterized for magnetic properties by Vibrating Sample Magnetometry (VSM) and for thickness by profilometry. Structural characterization was carried out by Θ-2Θ and Glancing Angle X-ray diffraction (XRD),

Scanning Electron Microscopy (SEM) and Wavelength Dispersive Spectroscopy. The structural characterization and magnetic property measurements were done pre- and post-lithiation. The lithiated samples are subject to degradation in atmosphere, so they were analyzed within an hour of lithiation, and the XRD measurements were performed in an inert He atmosphere.

Room temperature magnetic measurements were done on the cathodes pre- and post-lithiation using an ADE 880 Vibrating Sample Magnetometer by applying fields in the range between -10 kOe and 10 kOe. Structural changes were tracked by Θ-2Θ X-ray diffraction using a Rigaku RU300 X-ray generator and 185mm diffractometer in helium flow immediately post-lithiation. The Curie temperature was measured by cycling the cathodes in a furnace immediately post-lithiation under helium flow. External magnetic fields of up to 6 kOe were applied for saturation.

Chapter 4

Magnetic and Structural Investigation of Electrochemically Lithiated Magnetite Thin Films and Nanoparticles

4.1 Introduction

This chapter is concerned with analyzing the effects of electrochemical lithiation on Fe_3O_4, which crystallizes in the inverse spinel structure. Lithium spinels have been researched with a view to using them as cathode materials in lithium batteries [45, 46, 47]. Among the chemically synthesized lithium iron oxides, there are two main compounds, $LiFeO_2$ and $LiFe_5O_8$, which have been under scrutiny as cheaper and more environmentally friendly alternatives to $LiCoO_2$ and $LiNiO_2$ as battery cathodes and also as a substitute for garnets in microwave devices [33, 48, 49, 50]. These have been made by calcination of mixtures of Li_2CO_3 and Fe_2O_3, ion exchange reactions or by hydrothermal synthesis methods [49, 51, 52, 53, 54, 55, 56, 57]. $LiFeO_2$ crystallizes as a disordered rocksalt phase (Fm3m space group). Researchers have also synthesized layered $LiFeO_2$ and also the orthorhombic phase of $LiFeO_2$ which is

isostructural to $LiNiO_2$. $LiFe_5O_8$ crystallizes in the inverse spinel structure (Fd3m space group) at higher temperatures, wherein the 16d octahedral sites are symmetrically equivalent. This is a disordered fcc structure (β-$LiFe_5O_8$), in which the Li^+ and Fe^{3+} ions are randomly distributed in the 16d octahedral sites. Nanocrystalline β-$LiFe_5O_8$ synthesized through hydrothermal methods has been shown to have a saturation magnetization of 25 emu/g. It transforms to an ordered primitive cubic structure at lower temperatures where there is ordering on the 16d sites. The higher temperature phase can be preserved by quenching after solid state synthesis [45].

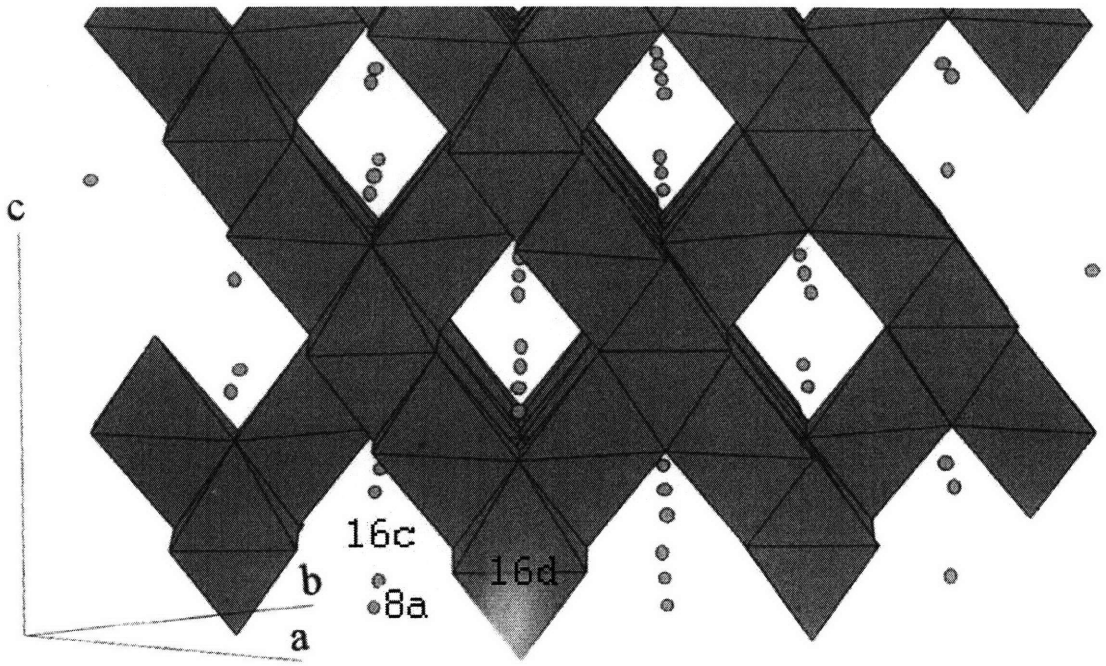

Figure 4-1: 8a, 16c and 16d sites in spinel

Chemical and electrochemical lithiation studies have been previously performed on Fe_3O_4 and γ-Fe_2O_3 powders [11, 32, 33]. These studies were done initially to investigate the suitability of iron oxide as a cathode material for high temperature

lithium batteries. The AB_2O_4 spinel structure provided a 3-D framework for the interstitial diffusion of Li ions. This was surprising because coulombic interactions between guest ions in interstitial 8a sites (small circles in Fig. 4-1) or vacant 16c octahedral sites (centers of empty octahedra in Fig. 4-1); and ions on the A or B sites prevent simultaneous occupation of these sites [27]. The lithiation reaction has been understood to occur through a mechanism that involves a transformation into a rocksalt structure $[\mathrm{Li\ A}]_{16c}[\mathrm{B_2}]_{16d}\mathrm{O_4}$ through cooperative displacement of 8a cations into vacant neighboring 16c octahedral sites due to electrostatic repulsion with Li^+ ions [3, 11, 27, 58, 59]. The spinel phase is retained in the regime $x<0.13$, but for $0.27<x<0.60$ there exists a two-phase mixture of spinel (Fd3m space group) and rocksalt (Fm3m space group) [3, 59]. $LiFe_3O_4$ synthesized by solid state reaction of Li_2CO_3 and α-Fe_2O_3 crystallizes in the rocksalt (Fm3m) structure [59]. Another study on $Li_xFe_3O_4$ ($0<x<1$) synthesized by solid state reactions indicated that the saturation magnetization varies linearly with lithium content for annealed samples, while the non-annealed samples do not show any regular variation in M_s [3]. This study also showed that chemically synthesized $LiFe_3O_4$ is paramagnetic at room temperature. There can be high Li^+ ion conductivity in rock-salt based structures [60]. In nanosized rocksalt transition metal oxides, lithiation may also involve formation of Li_2O and extrusion of Fe to form metallic nanoparticles [50], but this occurs for higher values of x for magnetite, for example at $x>2$ [32]. Mossbauer and atomic absorption spectroscopy studies on chemically lithiated Fe_3O_4 suggest that there may not be any extrusion of iron even for Li contents close to $x=2$ [11].

The conversion reaction is written as

$$\mathrm{Li} + \mathrm{Fe_3O_4} \rightarrow 4\,\mathrm{Li_2O} + \mathrm{Fe} \tag{9}$$

Fontcuberta et al studied the magnetic properties of the lithiated phase $Li_{0.6}Fe_3O_4$ [11]. At 4 K, the magnetic moment of $Li_{0.6}Fe_3O_4$ is 0.93 μ_B per formula unit compared to 4 μ_B for Fe_3O_4. The ordering temperature (Curie temperature) of the lithiated phase is around 150 K, considerably lower than that of Fe_3O_4, which is 860 K. The ordering temperature is lowered because the lithiated phase has its Fe ions in the

octahedral 16c and 16d sites. The strong A-O-B antiferromagnetic interactions that give rise to the high ordering temperature in the spinel are absent, and the weaker B-O-B interactions dominate. The ordering temperature of the lithiated phase is also less than the Néel temperature of 198 K for wustite, $Fe_{1-x}O$, which also crystallizes in the rocksalt structure. This is because there are fewer nearest neighbor Fe ions in the lithiated phase compared to $Fe_{1-x}O$ [11]. We can thus expect the magnetization to decrease as the spinel is lithiated. This should, in principle, result in complete disappearance of the magnetic moment at room temperature, since the rocksalt phase is expected to have a Curie temperature of 150 K [11].

In spinels, the Li ions have a preference to go into the tetrahedral 8a sites. The diffusion pathway for Li ions is through 8a-16c-8a channels in the structure. Therefore normal spinels, in which there are no ions other than Li in the tetrahedral sites, are more receptive to Li ion insertion. For example, it has been found that $Li_4Ti_5O_{12}$, which is a normal spinel, has excellent discharge capacity (105 mAh/g) and undergoes minimal strain upon Li insertion [45]. The $Li_4Ti_5O_{12}$-$LiFe_5O_8$ solid solution also has good reversible capacity because $LiFe_5O_8$ has a good lattice match with $Li_4Ti_5O_{12}$ [45]. However, the discharge capacity decreases with increasing Fe content because of the formation of an inverse spinel structure, in which the presence of octahedral site cations leads to shortening of the O-O distance and impediment in diffusion of Li ions through the 8a-16c-8a channels [45]. The magnetic properties of this solid solution at the iron-rich end has been studied by researchers [53]. This literature will be put in context of the results in Section 4.3.

The aim of the study was to study the effect on magnetic properties of inserting different amounts of Li into commercially available Fe_3O_4 nanoparticles by discharging them down to different voltages and to propose a model for the same.

4.2 Experimental Details

This section describes the methodology used for experiments on thin films grown by Pulsed Laser Deposition, and those on nanoparticles of Fe_3O_4.

4.2.1 Growth, characterization and lithiation of iron oxide thin films

Thin films of iron oxide (Figure 4-2) were grown by PLD on single crystal Si, MgO and polycrystalline polished Cu substrates from a hematite (α-Fe_2O_3) target, using a KrF excimer laser at 248 nm wavelength. In previous work, it was found that at chamber pressures of the order of 10^{-4} Pa and substrate temperature of 500 ^oC, the phase that grows is maghemite, γ-Fe_2O_3 [35, 36, 61]. However, the stoichiometry of the target is not reproduced exactly in the film, and the composition of the films is intermediate between Fe_2O_3 and Fe_3O_4. Based on these results, the films for this study were grown with laser energies of 300-500 mJ/pulse, laser repetition rates of 50 Hz, substrate temperatures between 300-500 ^oC and at chamber pressures in the range 10^{-4} to 10^{-5} Pa. A high repetition rate of 50 Hz is used to prevent transformation of the metastable maghemite to stable hematite, which occurs above 400 ^oC. An example of XRD data (Cu Kα radiation, θ-2θ geometry) from two films is given in Figure 4-3, in which the higher substrate temperature yields a single-phase spinel structure film. Film thicknesses were 100-200 nm, and the films on Cu substrates had a (111) preferred orientation.

Iron oxide films grown on copper were lithiated electrochemically. Coin cells of the form Li|1M$LiPF_6$ (EC:DMC)—Iron oxide were assembled in an Argon filled glove box (oxygen level < 2ppm and moisture level < 1ppm). The cells were tested for open circuit voltage and discharged galvanostatically at rates of C/50-C/200 to voltage cutoffs of 1.2 V-0.8 V vs. Li/Li^+. The current density used for these experiments was 1 $\mu A/cm^2$. The films were analyzed for structure and magnetic properties post-lithiation.

4.2.2 Experiments on Fe_3O_4 nanoparticles

Composite thick film cathodes roughly 30 μm in thickness were prepared by casting a mixture of magnetite nanopowders (Alfa Aesar, mean size 65 nm), SUPER P^{TM} conductive carbon black and poly- (vinylidene fluoride) (PVDF) in the weight ratio

11:6:3 on aluminium substrates, and punching out circular disks [43]. The starting magnetite powders contain hematite, corundum-structured α-Fe_2O_3 as an impurity, which is estimated to be around 15% from the ratio of intensities of XRD peaks and measurement of saturation magnetization M_s [43]. The cathodes were dried, weighed, assembled into cells in an argon-filled glovebox and subjected to galvanostatic electrochemical discharge to voltages in the range 1.0 to 1.7 V. This resulted in samples with lithium contents between x=0.01 and x=2. Details on the procedure can be found in [43].

For the experiments on nanoparticles, composite cathodes were used. The electrode slurry was prepared by mixing Fe_3O_4 powder (Alfa Aesar, USA) with 30 wt% Super P carbon (TIMCAL) and 15 wt% poly (vinylidene fluoride) (PVDF) in N-methyl pyrrolidone (NMP) solution. The slurry was cast onto an Al foil and dried in a vacuum oven at 120 ^oC for 12 hrs. The electrode disks (area = 1.76625 cm^2) were punched and dried in a vacuum oven at 70 ^oC for 6 hrs before storing them in an argon-filled glove box (oxygen level less than 1ppm and water level less than 1.5ppm). 2016 coin cells were assembled in the glove box, which consisted of the Fe_3O_4 and Li foil electrodes, and two pieces of Celgard separator (Celgard Inc, USA). 1M $LiPF_6$ in a 1:1 EC:DMC solvent (Merck, TECHNO, SEMICHEM Co. Ltd., Korea) was used as the electrolyte. The coin-cells were allowed to rest overnight in the glove box before electrochemical testing. The coin-cells were galvanostatically discharged to different voltages between 1.7 V and 0.9 V at C/100 (current density = 2.16 mA/g and 2-3.5 $\mu A/cm^2$) using a Solartron 1470 battery tester. The intensity of (111), (220), (311) and (440) spinel peaks and the main (104) hematite peak were tracked for the samples lithiated to different extents.

4.3 Results and Discussion

The results from experiments on thin films and nanoparticles of iron oxide are summarized below.

4.3.1 Electrochemical Lithium Insertion into Fe_2O_{3-x} thin films

A SEM image of a film grown on Si at a temperature of 500 °C, and a laser repetition rate of 50Hz in vacuum is shown in Fig. 4-2. The film is dense and

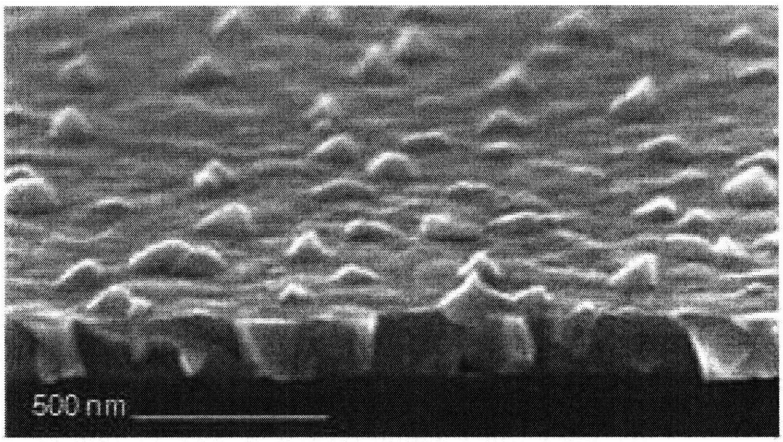

Figure 4-2: SEM of film on Si (50Hz, 500 °C, 8x10^{-4} Pa)

polycrystalline, with surface roughness due to faster growth of some grains. This morphology was observed to persist upon lithiation. XRD shows that the intensity of the (311), (220) and (440) spinel peaks decrease upon lithium insertion. The reduction of intensity of the spinel peaks is consistent with the transformation into the rocksalt phase upon lithiation. However, since the major peaks of the lithiated rocksalt phase overlap with the copper and also the (111) spinel peak, it is difficult to quantify the percentage of the rocksalt phase that forms. The saturation moment of the films decreases by up to 30% upon electrochemical discharge. An example of the effect of lithium insertion on the magnetic hysteresis loop of an iron oxide film grown on Cu at 500 °C, 50 Hz in vacuum is shown in Fig. 4-4. The variation of saturation magnetization with lithium content is summarized in Fig. 4-5. The formation of the lithiated phase is expected to reduce the overall moment of the film, because the rocksalt is paramagnetic at room temperature. In addition, if Fe nanoparticles form by extrusion, their subsequent oxidation in atmosphere would form antiferromagnetic hematite or superparamagnetic magnetite or maghemite particles, which would also

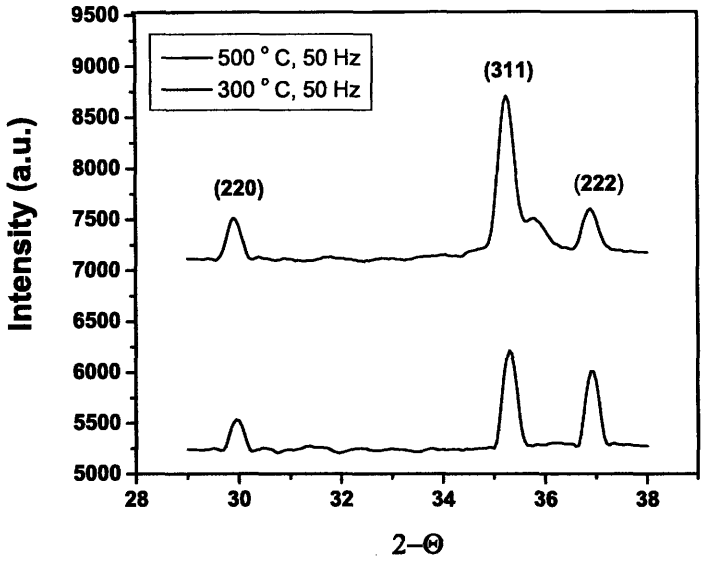

Figure 4-3: XRD of films grown in vacuum on Cu at 300 °C and 500 °C with laser repetition rate of 50 Hz , indexed to the spinel structure. The film grown at 300 °C shows a non-spinel peak at 35.8°.

reduce the moment of the film. Ideally, the moment of the film would drop to zero following completion of any of these reactions, but in this experiment the greatest decrease in moment was approximately 30% over a range of lithiation conditions. This suggests that there is a kinetic limitation to the lithium insertion, presumably as a result of the high density of the film, which limits contact with the electrolyte to the top surface of the film, and thereby limits the lithiation to the surface region of the film. This point will be discussed further in Section 4.5.

4.3.2 Electrochemical Lithium Insertion into Magnetite Nanoparticles

With a view to understanding the possible kinetic limitations of lithiation of thin films, investigations were carried out on commercial nanoparticles with a mean size of 65 nm. In these experiments, composite cathodes were used that comprised 55 wt% active material (Fe_3O_4), 30 wt% conducting additive, and 15wt% PVDF. X-ray

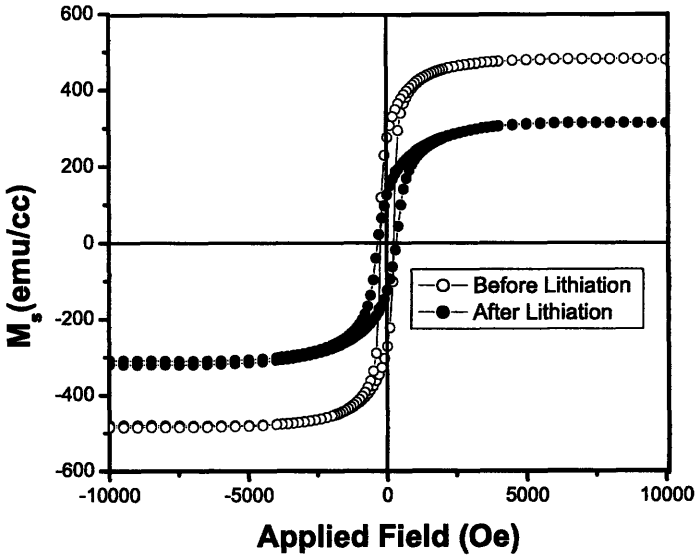

Figure 4-4: Magnetic hysteresis loops of a film grown on Cu before and after discharge to 0.9 V at room temperature. The film was grown at 500 °C, 50 Hz repetition rate and at a chamber pressure of $6x10^{-4}$ Pa.

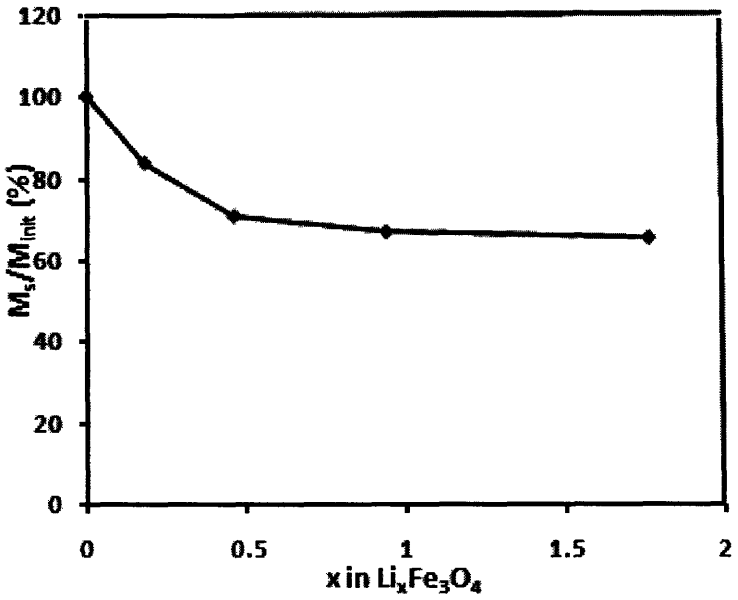

Figure 4-5: Variation of Saturation Magnetization with lithium content in PLD-grown films

diffraction data of the starting nanopowders is shown in Figure 4-6. The peaks index to the spinel structure. However, peaks from hematite are also present, with a volume fraction of roughly 15%.

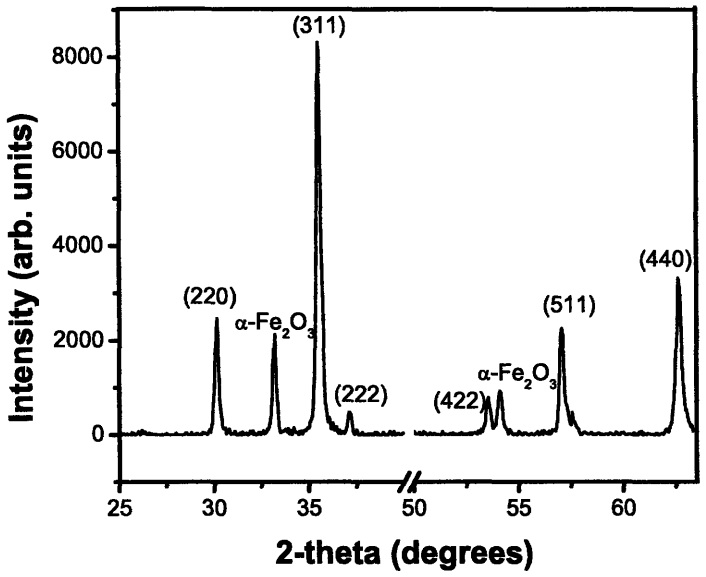

Figure 4-6: XRD pattern of nanocrystalline magnetite powder (before discharge).

Discharge curves for different discharge rates are shown in Figure 4-7. An optimum discharge rate of C/100 was chosen because there is no further significant upward shift of the voltage profiles upon decreasing the rate beyond C/50. The effect of electrochemical lithium insertion on the saturation moment is summarized in Figures 4-8 and 4-10. This data shows that the saturation moment is maintained up to approximately x = 1, and beyond this the moment drops rapidly with Li content. An example of hysteresis data is shown in Figure 4-8, where the hysteresis curves are plotted for a sample before and after discharge down to 0.9 V. The coercivity and loop shape are largely unchanged but the M_s has decreased by 53.4%. The large drop in saturation moment beyond x=1 in these experiments indicates the formation of substantial fractions of non-magnetic phase. This most likely consists of the lithiated rocksalt phase, which is paramagnetic at room temperature. The decrease in

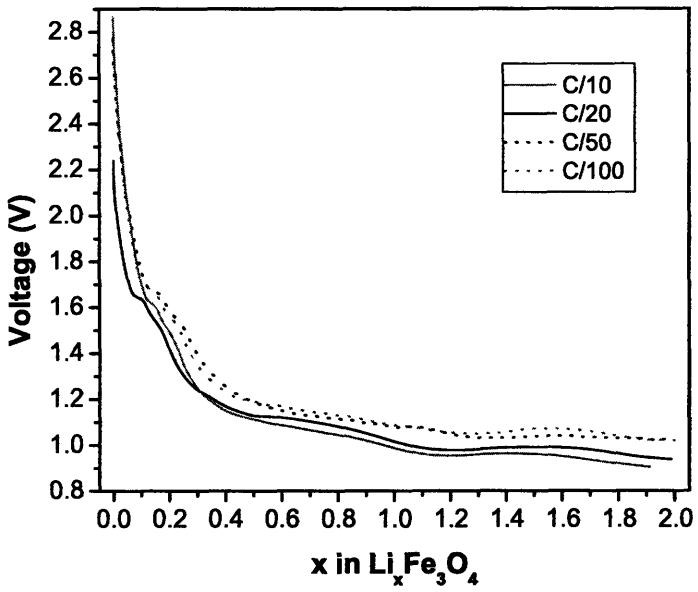

Figure 4-7: V-x curves for coin cells discharged down to a voltage cutoff of 0.9 V (current density $\sim$ 3-40 μA/cm^2)

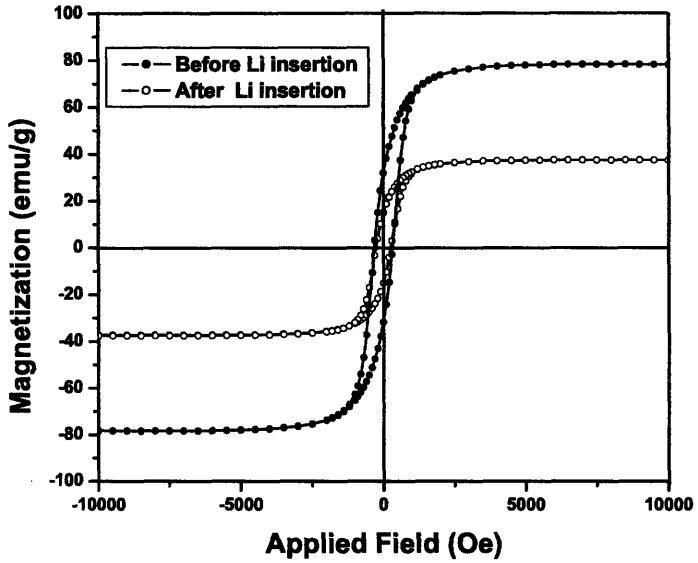

Figure 4-8: M-H curve of a cathode discharged down to 0.9 V at C/100 (current density= 3.7 μA/cm^2, x_{Li} inserted = 1.992).

moment with increasing lithium content may be a result of a decrease in Curie temperature with increasing x. Additionally, if Fe is extruded from the structure at high Li content, its subsequent oxidation could lead to superparamagnetic nanoparticles of magnetite or maghemite, or antiferromagnetic particles of hematite or wustite, any of which would reduce the room-temperature moment of the sample. Measurements of the temperature dependence of the magnetization of the samples can distinguish between these possible mechanisms, and these will be described in Section 4.3.5.

4.3.3 Structural Investigation

The XRD data are shown in Figure 4-9. It is expected that the spinel peaks change in relative intensities as lithiation proceeds, due to formation of the rocksalt structure from the spinel framework [11]. The ratios of (220), (311), (440) peaks of the spinel and the hematite (104) peak to the (111) spinel peak intensity are shown in Figure 4-9 as a function of lithium content. It is clear that the hematite phase is transformed, since this peak decreases in intensity and vanishes completely by x=2. The hematite/(111) peak ratio decreases from 26.0 at x=0 to 0.5 at x=1. Also the magnetite (311)/(111) ratio decreases from 36.6 at x=0 to 2.85 at x=2. The (220)/(111) peak ratio decreases from 9.0 at x=0 to 0.6 at x=2. The decrease in the (440)/(111) and (220)/(111) intensity ratios is in agreement with the mechanism proposed in the literature which involves cooperative displacement of Fe ions from the tetrahedral sites into octahedral sites [27].

4.3.4 Room-Temperature Magnetic Properties

The results of room-temperature magnetic measurements on lithiated nanoparticles are summarized in Figure 4-10. It is clear that the saturation magnetization decreases as lithiation proceeds, dropping to 29.2% of the original value at x=1.99. We note that there is not much change in the saturation moment in the regime x=0 to x=1. There is negligible change in the remanence M_r/M_s, except for a small rise in the beginning and beyond x=1.5. The coercivity shows no change until x=1.5,

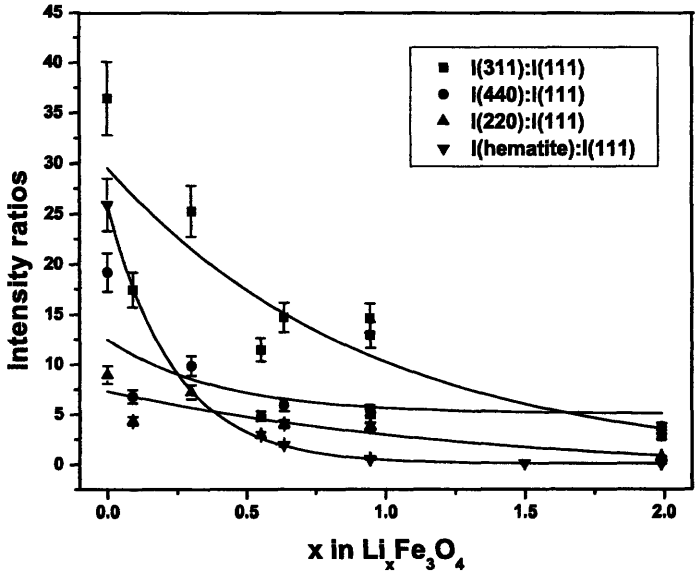

Figure 4-9: Intensity ratios of various spinel and hematite peaks as function of lithium content. The lines serve as a guide to the eye.

beyond which it starts to decrease.

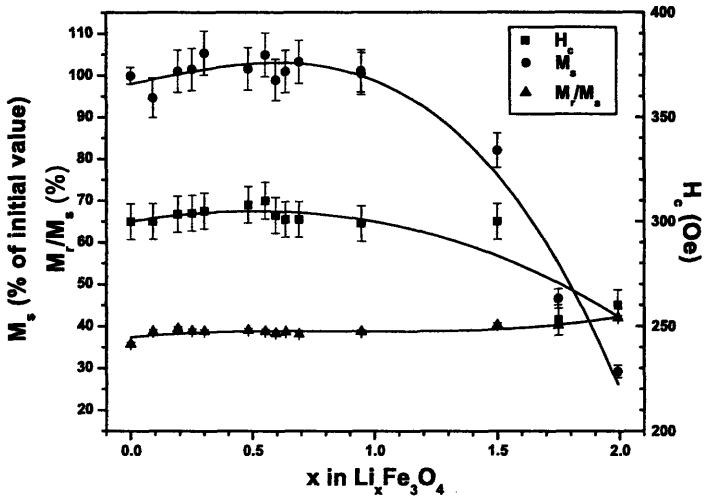

Figure 4-10: Variation of Saturation Magnetization, Coercive Field and Remanence with lithium content. The error bars denote the experimental errors.

4.3.5 Curie Temperature

The results of Curie temperature measurements are summarized in Fig. 4-11. The curve for the cathode prior to lithium insertion has an upward slope around 720 K. This anomalous behavior is seen in some samples, while in others it is absent. These features disappear upon cooling back down, so this is probably a result of an irreversible phase transformation upon heating. The source of this anomaly is unclear. However, Xu et al. point out that the annealing of superparamagnetic particles can contribute to an anomalous increase in magnetization with increase in temperature [62]. It is possible that presence of a small fraction of superparamagnetic particles in our starting powders could cause such behavior. However, the Curie temperatures unexpectedly remain close to that of bulk magnetite, which is 860 K, even though the moment decreases. This suggests that a fraction of the material is not transformed completely into the rocksalt phase, due to kinetic limitations. The cores of the nanoparticles probably remain unlithiated .

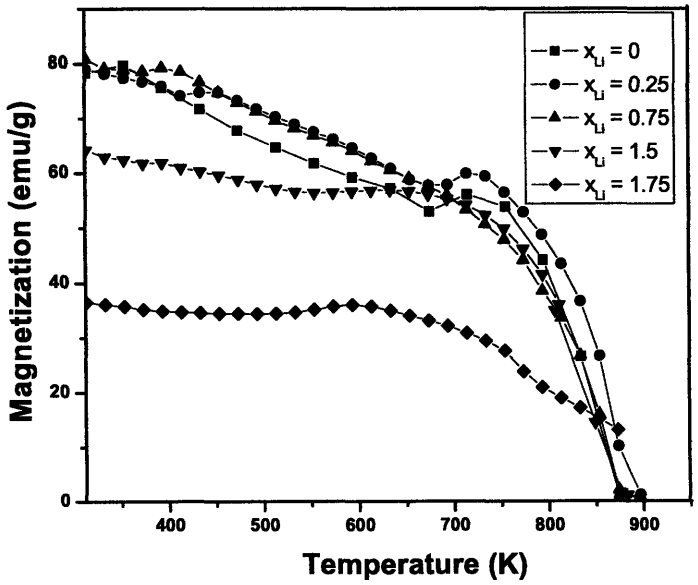

Figure 4-11: Summary of Curie Temperature measurements on samples discharged to different extents. Here x_{Li} denotes the number of moles of lithium inserted.

There are two main differences between the data for nanoparticles shown in Fig. 4-10 and that for samples synthesized by solid state reaction reported in the literature [3]. Neto et al report a monotonic decrease in M_s with lithium content for annealed samples [3], whereas these experiments show negligible changes in M_s until x=1. The Curie temperature remains close to that of Fe_3O_4, whereas chemically sythesized $LiFe_3O_4$ is paramagnetic at room temperature [3]. This suggests a different mechanism at work compared to that reported by Neto et al. These aspects will be considered next.

4.4 Model for M_s - x in $Li_xFe_3O_4$

We will now describe the possible mechanisms for the redistribution of ions in magnetite during Li insertion. These models are valid only for small x, and suggest different dependences of M on x, which will be compared with experimental data.

4.4.1 Topochemical reduction without cooperative displacement of ions

In this model, the Fe ions remain in their original positions, but a fraction x of octahedral Fe^{3+} is reduced to Fe^{2+}. The formula is:

$$[(Fe^{3+})^{8a\downarrow}]^A[(Fe^{2+})^{16d\uparrow}(Fe^{3+}_{1-x})^{16d\uparrow}(Fe^{2+}_x)\ ^{16d\uparrow}(Li^{+}_x)^{16c}]^B$$

$$M_s = [4 + 5(1-x) + 4x] - 5 = 4 - x \qquad \mu_B \text{ per F.U.} \tag{10}$$

Therefore M decreases linearly with x.

4.4.2 Cooperative displacement of 8a Fe^{3+} ions into 16c sites

This is a more realistic scenario, since diffusion of Li ions through 8a tetrahedral sites would cause displacement of tetrahedral Fe^{3+} ions into neighboring 16c sites due

to electrostatic repulsion. Although Fe^{2+}-Fe^{2+} (d^6-d^6) and Fe^{3+}-Fe^{3+} (d^5-d^5) B-B interactions are antiferromagnetic and introduce frustration into the system, limiting the model to low x values simplifies the picture. At low x, since there are very few 16c Fe cations, we can assume that:

1. Any 16c Fe will have only 16d Fe as its nearest neighbours (NN), and therefore 16d-16d and 16d-16c interactions would dominate over 16c-16c.

2. Overall, the dominant interactions are the A-B interactions which are antiferromagnetic in spinel and much stronger than B-B interactions.

3. Since the Curie temperature does not change much upon lithiation, it is reasonable to assume that the room temperature saturation magnetization is close to that at 0 K. The individual magnetic moments of Fe^{3+} and Fe^{2+} are 5 and 4 μ_B respectively.

4. There is preferential reduction of octahedral ions (16c ions) upon lithiation since the divalent ions that are formed upon lithiation being larger in size would prefer the bigger octahedral sites.

This results in:

$$[(Fe^{3+}_{1-x})^{8a\downarrow}]^A[(Fe^{2+})^{16d\uparrow}(Fe^{2+}_x)^{16c\downarrow}(Fe^{3+})^{16d\uparrow}(Li^{+})^{16c}_x]^B$$

$$M_s = [5 + 4 - 4x] - 5(1 - x) = 4 + x \quad \mu_B \text{ per F.U.} \tag{11}$$

From the voltage-charge curves, it appears as though the first plateau-like feature appears at x$\sim$0.2. We may assume that until this point, there is no displacement of Fe ions within the structure, and there is cooperative displacement of the ions beyond this. The resultant model is plotted along with the results for PLD-grown films and nanoparticles in Fig. 4-12. The model proposed by Neto et al is shown for comparison. It is clear that the PLD films and the nanoparticles show markedly different behavior. The behavior of the nanoparticles appears to be in reasonable

agreement with our model in the limit of small x, although the choice of x=0.2 as the point of commencement of the displacement of tetrahedral Fe^{3+} ions into octahedral 16c sites limits the applicability of the model. It is also not clear why the particles and thin films exhibit these differences in magnetic behavior.

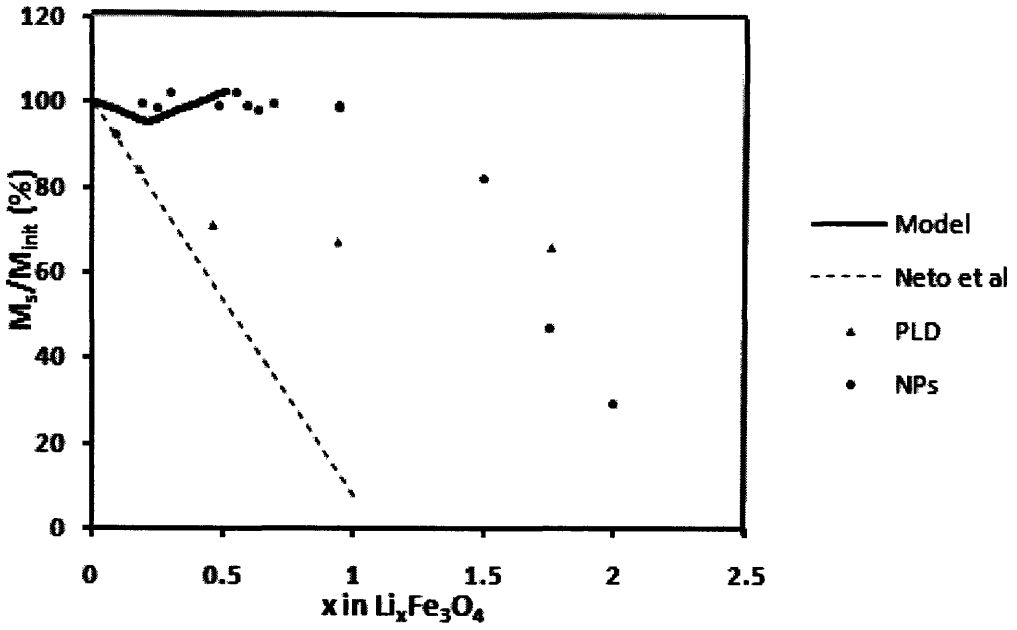

Figure 4-12: Comparison of experiments on NPs and PLD films to model. Results from a report in the literature on solid-state synthesis of lithium iron oxide is shown in the dotted line [3].

This suggests that the hematite impurity present in the nanoparticles might have a significant effect. X-ray diffraction measurements (Figure 4-9) indicate that the hematite phase disappears at lithium concentrations between x=0.63 and x=0.95. For the sake of simplicity, one may assume that the hematite reacts completely by x=0.63. The impurity hematite will also undergo a transformation from the hcp (corundum) structure to a ccp (rocksalt) structure [33, 48]. Furthermore, researchers have shown that the spinel-to-rocksalt phase transformation is suppressed in nanosized γ-Fe_2O_3 [63]. It is possible that nanosized magnetite undergoes a similar topochemical reaction mechanism and suppression of the spinel-rocksalt phase transformation and this may also explain the observed changes in M_s. A more rigorous model for the magnetic

behavior should take into account the reaction of hematite with lithium until x=0.63 since there might be competition between the Li insertion reaction into magnetite and the monophasic insertion reaction into hematite in the initial stages[33, 48].

However, the points of onset and completion of the reaction of hematite with lithium, and that of displacement of the tetrahedral Fe ions into octahedral sites are not clear and this complicates the picture. The high Curie temperatures suggest that there may be some unreacted Fe_3O_4 and the presence of hematite as impurity phase makes it difficult to estimate the percentage of unreacted phase.

Further, the calculated energies (GGA+U) for monophasic reaction with $Li_xFe_3O_4$ are 0, -1.69 and -0.3636 eV for x=0, 0.5 and x=1.0 respectively, while those for iron extrusion are -1.15, -1.07 and -1.19 eV for x=0, x=1 and x=2 respectively [22]. This suggests that at every stage, iron extrusion can be a competitive process to the reaction with spinel [22].

The exact nature of the mechanism responsible for the observed changes in M_s-x behavior is thus unclear, and is an unanswered question. It could be worthwhile to repeat these experiments on single-phase particles of Fe_3O_4 (without hematite impurity) to distinguish between these mechanisms. Mössbauer or EXAFS studies could also be useful to elucidate the exact mechanism. This will be discussed further in section 6.3.

4.5 Kinetic effects in PLD-grown thin films

This section discusses a simple model for describing some of the kinetic limitations in thin films outlined in Section 4.3. The geometry of diffusion in nanoparticles and thin films of PLD is shown in Fig. 4-13. It is assumed that the rate limiting step for the nanoparticles is solid state diffusion, whereas for the thin films, it could be either grain boundary diffusion or diffusion through the interior of the grains. Kinetic effects arising from diffusion through the liquid electrolyte and the Solid-Electrolyte Interface (SEI) have been ignored in this analysis. The lithiation process is modelled in terms of an effective diffusion coefficient D for diffusion of lithium ions. The times

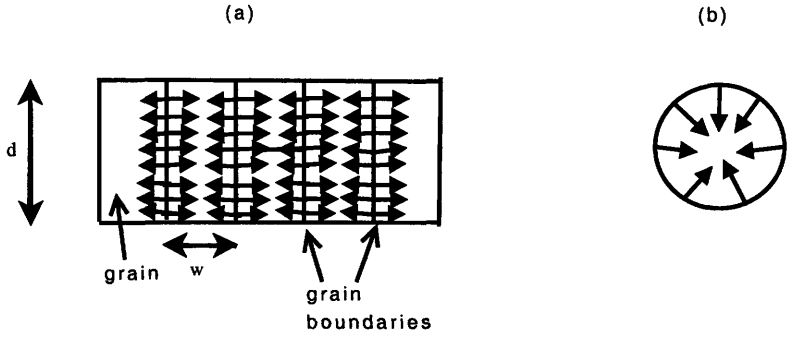

Figure 4-13: Schematic showing pathway for solid state diffusion of Li in (a) PLD-grown thin films (b) Nanoparticles of Fe_3O_4

for completion of diffusion through the films and nanoparticles can be calculated through the relation:

$$L = \sqrt{Dt} \tag{12}$$

where D is the effective diffusion coefficient for Li ions in Fe_3O_4, t is the time required for diffusion; and L is the diffusion length. This yields:

$$t_{NP} = r^2/D \tag{13}$$

where r is the radius of the nanoparticles.

There are two possible situations for diffusion in the thin films:

(a) Fast grain boundary diffusion: In this case, diffusion into the interior of the film from the grain boundaries is the rate limiting step.

$$t_{TF} = (0.5w)^2/D \tag{14}$$

where w is the width of the columnar grains in the thin film (Figure 4-13).

Therefore the ratio of the times required for complete diffusion through the films and nanoparticles is:

$$t_{TF}/t_{NP} = (0.5w/r)^2 \tag{15}$$

This gives a ratio of 2.4 assuming a 100 nm columnar width of the grains and 32.5 nm radius of the nanoparticles.

(b) Slow grain boundary diffusion: Since the grain boundaries extend through the thickness of the films (Figure 4-2), the total diffusion length is equal to the thickness of the film.

$$t_{TF} = (d)^2/D \quad (16)$$

In this case, the ratio of the times required for complete diffusion through the films and nanoparticles is:

$$t_{TF}/t_{NP} = (d/r)^2 \quad (17)$$

This gives a ratio of 9 for the times required for diffusion through the films and nanoparticles (assuming 100 nm thick films).

From the above discussion it is clear that there are greater kinetic limitations in the films compared to the nanoparticles.

4.6 Comparison to battery literature

In this section, the electrochemical measurements observed for Fe_3O_4 nanoparticles will be compared to the literature.

Ito et al obtained large capacities ($\sim$ 400 mAh/g) by using Fe_3O_4 fine particles as the cathode material upon discharge to 1.0 V [64]. However, it is to be noted that in our experiments we restricted the experiments to a capacity of 2 moles of Li per formula unit (or 230 mAh/g) coinciding with onset of iron extrusion [32]. The voltage-charge plot shown in Figure 4-7 is similar to the signature curve reported in lithium battery literature on use of Fe_3O_4 as a conversion electrode [32, 64, 65]. From these plots, it is clear that there are two distinct regimes. The first is a sloping regime (between 1.7 to 3 V) and the second one is a flatter region (between 1.0 to 1.7 V). This suggests that there may be two distinct mechanisms in operation in these regions, although open circuit voltage measurements would perhaps be a more rigorous way of elucidating the different mechanisms than the voltage-charge plots discussed here.

4.7 Conclusion

Fe_2O_{3-x} thin films grown by pulsed laser deposition (PLD) and commercially available magnetite nanoparticles were subjected to galvanostatic electrochemical dis-

charge at room temperature. Both systems show a substantial decrease in saturation magnetization M_s and a reduction in intensity of the 311, 220 and 440 X-ray reflections. We have observed a change in M_s of up to 30% for thin films and 75% for nanoparticles by discharging down to 0.9 V versus Li/Li^+. This decrease may be due to formation of a paramagnetic lithiated phase. The smaller drop observed in thin films is attributed to a kinetic effect because the high density of PLD-grown films limits lithiation to just the surface of the film. In magnetite nanoparticles, the porosity of the composite cathode and the larger surface area of the particles would result in better contact between the electrolyte and the oxide, and reduced kinetic limitations.

The magnetization is expected to decrease due to formation of paramagnetic lithiated phase. However, this should result in zero net room temperature magnetization upon completion of the phase transformation due to low ordering temperature of the lithiated phase. Although a substantial decrease in M_s was observed upon insertion of more than one mole of Li per formula unit into Fe_3O_4 nanoparticles, room-temperature magnetic measurements and Curie temperature measurements suggest that there are negligible changes in magnetization until x=1. There could be two possible explanations for this. Firstly, the spinel-rocksalt phase transformation may possibly be suppressed due to small size of the particles. Secondly, the presence of hematite as the impurity phase could also be a reason since it could be reacting with lithium in the early stages, and delaying the onset of the reaction of lithium with the spinel.

Chapter 5

Electrochemical Control of the Magnetic Moment of CrO_2

5.1 Introduction

Since the advent of research into chemical and electrochemical lithium insertion into chromium oxides [66, 67], researchers have looked into the possibility of using these oxides for Li batteries. There are a few reports on Li insertion into CrO_2, which shall be discussed in the following paragraphs [12, 13]. However, there have been no reports on the effect of lithiation on the magnetic properties of CrO_2. Among the chemically synthesized lithium chromium oxides, $LiCr_3O_8$ have been the subject of recent investigations, owing to their good rechargeability and energy density [67]. This is partly because the mechanism involved may be intercalation-deintercalation similar to that observed in the CoO_2-$LiCoO_2$ system. Electronic structure studies indicate that there may exist ferromagnetic ordering in certain phases of Cr_3O_8 and $LiCr_3O_8$ [67]. It has been suggested that lithium intercalation in this material system proceeds not through reduction of the valence of chromium, but instead through a regulation of the degree of covalency of the Cr-O bonds [67]. However, the application of this system towards chemical switching of magnetism is limited owing to their low ordering temperatures.

Insertion of lithium into CrO_2 produces compounds of formula Li_xCrO_2. In its

most stable crystal structure at x=1, $LiCrO_2$, is a Heisenberg antiferromagnet with a Néel temperature of 62 K [68]. In general, $LiMO_2$ compounds, where M is a transition metal, have a layered structure in which the Li and M ions occupy octahedral sites within an fcc oxygen lattice [69, 70]. In $LiCrO_2$ the Cr^{3+} ions occupy points on a two-dimensional triangular lattice separated by sheets of lithium and oxygen [71]. $LiCrO_2$ is isostructural with $LiNiO_2$, in which Li and Ni are segregated into layers perpendicular to the <111> direction, and there is a small distortion of the fcc lattice [72]. The $LiCrO_2$ compound is therefore a rhombohedrally-stacked 2-D triangular lattice antiferromagnet, with frustrated antiferromagnetic ground state magnetic order. There has been little work on lithium deintercalation and intercalation in $LiCrO_2$ [73]. Deintercalation in Li_xCrO_2 was found to be possible only between x=0.8 and x=1.0, and the reversibility was extremely poor [74].

Experiments on lithium intercalation have demonstrated a higher capacity (charge storage) in amorphous CrO_2 compared to crystalline CrO_2 (150 mAh/g and <50 mAh/g, respectively) [75, 76], but there has been no report on the effects of Li content on magnetic properties. One of the key parameters determining the kinetics and reversibility of electrochemical Li insertion in CrO_2 is the diffusivity of the Li ions. While CrO_2 has not been studied in detail, more information is available on TiO_2 in the rutile structure [77, 78, 79, 80, 81].

The TiO_2 rutile structure provides a highly anisotropic framework for diffusion of Li ions, with the diffusion coefficient being 5 orders of magnitude greater in the c-direction (10^{-6} cm^2/s) compared to the a- and b- directions [78, 79]. In TiO_2, inserted lithium ions are expected to occupy octahedrally-coordinated sites, which are favored by approximately 0.7 eV over tetrahedral sites [77]. The limited diffusivity in the ab planes restricts the capacity of rutile for Li insertion [77, 79] at room temperature. Early work on lithium insertion into rutile-structured TiO_2 suggested that while anatase TiO_2 has good reversible capacity, rutile-structured TiO_2 requires larger distortion of the crystal lattice and therefore lithium insertion into rutile is mainly a surface effect [53]. This was earlier rationalized due to the highly dense nature of the rutile structure. The evidence was inconclusive, and it has been suggested that the

difficulty is more due to blocking of the c-channel due to sluggish diffusion in the ab plane and due to Li-Li interactions than purely thermodynamic effects [31, 78, 79]. However, as the Li content increases, and the tetravalent ions are reduced into larger trivalent ions, the lattice expands in the ab plane and this could enhance the diffusion along the c-axis [79, 80]. However, this may not necessarily improve the overall kinetics since the ab diffusion is slow. Larger Li contents have also been introduced at higher temperatures, for example 1 mole of Li per formula unit of TiO_2 at 120 °C [81].

Researchers have tried to compare the experimental results on lithiation of TiO_2 with Hartree-Fock calculations using suitable *a posteriori* approximation corrections for electron correlations [82, 83]. In one such study, the difference in Mulliken charge, 3d population and local spin moments upon Li insertion into different polymorphs of TiO_2 were calculated [82]. These studies used structures for the fully lithiated compound $LiTiO_2$ by deriving from experimentally observed phases for intermediate Li composition. The Mulliken charge (which refers to the partial atomic charge calculated based on the LCAO method) serves as a measure of the difference in electronic density and thus changes in electronic and magnetic properties upon Li insertion [82]. These suggest that the rutile polymorph is most stable form of TiO_2 and the orthorhombic polymorph is most stable form of $LiTiO_2$. They show that due to significant covalency, the effective charge on the cations is reduced and there is formation of a local moment of 1 μ_B at the Ti sites [82]. There is no literature for calculations on CrO_2 for similar comparison.

This prior work suggests that the electrochemical Li-ion insertion process may be useful for creating large and reversible changes in the magnetic moment of CrO_2. In the first half of this chapter, the effect of Li insertion on the magnetic properties of 550 nm x 45 nm CrO_2 powder is reported and correlated with structural changes. Of particular interest is the extent of reversibility of both the electrochemical behavior and the magnetic properties.

The second part of the chapter describes the experiments on reversible changes in magnetic properties of 400 nm x 45 nm CrO_2 particles due to electrochemical

lithium insertion, forming Li_xCrO_2 where x<1. The significance of these experiments is exploration of the possibility of obtaining better reversibility (due to better strain accommodation) and also of enhanced kinetics (due to smaller Li diffusion path) in CrO_2 nanoparticles of slightly reduced size. The investigation on effects of galvanostatic electrochemical cycling on the magnetic properties of these CrO_2 nanoparticles focused in particular on the effect of the rate of Li^+ insertion.

5.2 Experimental Details

This section describes the experimental procedures, starting with those for the investigation on 550 nm x 45 nm CrO_2 particles.

The details of the preparation of positive electrodes (cathodes), and electrochemical schedules have already been described on page 57. Electrochemical cells (type TJ-AC, Tomcell Co. Ltd., Japan) were used for electrochemical measurements. Needle-shaped particles of CrO_2 with approximate dimensions of 550 nm x 45 nm (DuPont Magtrieve^{TM}) estimated from a scanning electron micrograph, Fig. 5-1, were used to make the composite cathodes, which contained a mixture of CrO_2: superP^{TM} carbon : PVDF with a weight ratio of 80:10:10 [43, 44]. The mixture was cast onto a 20 μm-thick aluminium substrate, forming a layer either 79$\pm$1.5 μm or 159$\pm$2 μm thick. The substrates were cut into disks and formed into cells with a Li metal anode and 1 M $LiPF_6$/ethylene carbonate/ diethyl carbonate electrolyte. The current applied to the cells was 3.2 mA per gram of CrO_2, corresponding to the insertion of 0.01 mole of lithium ions per formula unit of CrO_2 every hour. The applied voltage was kept below 4.5 V to avoid electrolyte decomposition and above 0.9 V to avoid reaction with the carbon and binder materials.

The cells were characterised magnetically before and after electrochemical cycling using a vibrating sample magnetometer at room temperature. The bulk magnetization M_s of the starting CrO_2 powders was 90 emu/g at 10 kOe. CrO_2 powders are difficult to saturate, and a size-dependent magnetization has been reported [84], but our value for M_s agrees well with reported values. A high-field paramagnetic slope

(3-11 x 10^{-6} emu/Oe) observed in the hysteresis curves of the cathodes above 6 kOe that originated from the additives and the aluminium substrate was subtracted from the measurements. This slope subtraction procedure had only a small effect (3-4%) on the calculated change in saturation magnetization caused by lithiation. X-ray diffraction of opened cells was carried out in Θ-2Θ geometry using a diffractometer with Cu Kα radiation. The starting powders contain some trace Cr_2O_3 estimated to be <1% from the ratio of XRD peak intensities. The CrO_2 phase may decompose upon exposure to the atmosphere, since it is metastable at ambient conditions [85]. This was evident in some samples that were exposed to the atmosphere for a prolonged period after overnight vacuum drying at 120 °C, in which XRD peaks corresponding to the orthorhombic oxy-hydroxide CrO(OH) phase were found. In order to avoid unwanted reactions, the cathodes were stored and assembled into coin cells inside a glovebox prior to the experiments.

Electrochemical Li^+ insertion of ~400 nm x ~45 nm needle-shaped CrO_2 particles (MicroMagnetics, Inc.) was carried out in type TJ-AC cells (Tomcell Co. Ltd., Japan). These particles were made into composite cathodes using a weight ratio of 80:10:10 of CrO_2:polymeric binder:conductive carbon. Details on preparation of cathodes and cells can be found in section 3.3.3. The discharge process used here produced samples with a nominal composition of Li of up to 0.5 moles per formula unit at the rate of C/100. For the discharge steps, a termination voltage of 0.9 V was used, and 4.5 V was used as the termination voltage for the subsequent charging steps. The cathodes were characterized pre- and post-lithiation by Vibrating Sample Magnetometry (VSM) and Θ-2Θ X-ray Diffraction.

5.3 Results and Discussion

The results from experiments on 550 nm x 45 nm chromium dioxide particles and nanoparticles of CrO_2 are summarized in this section.

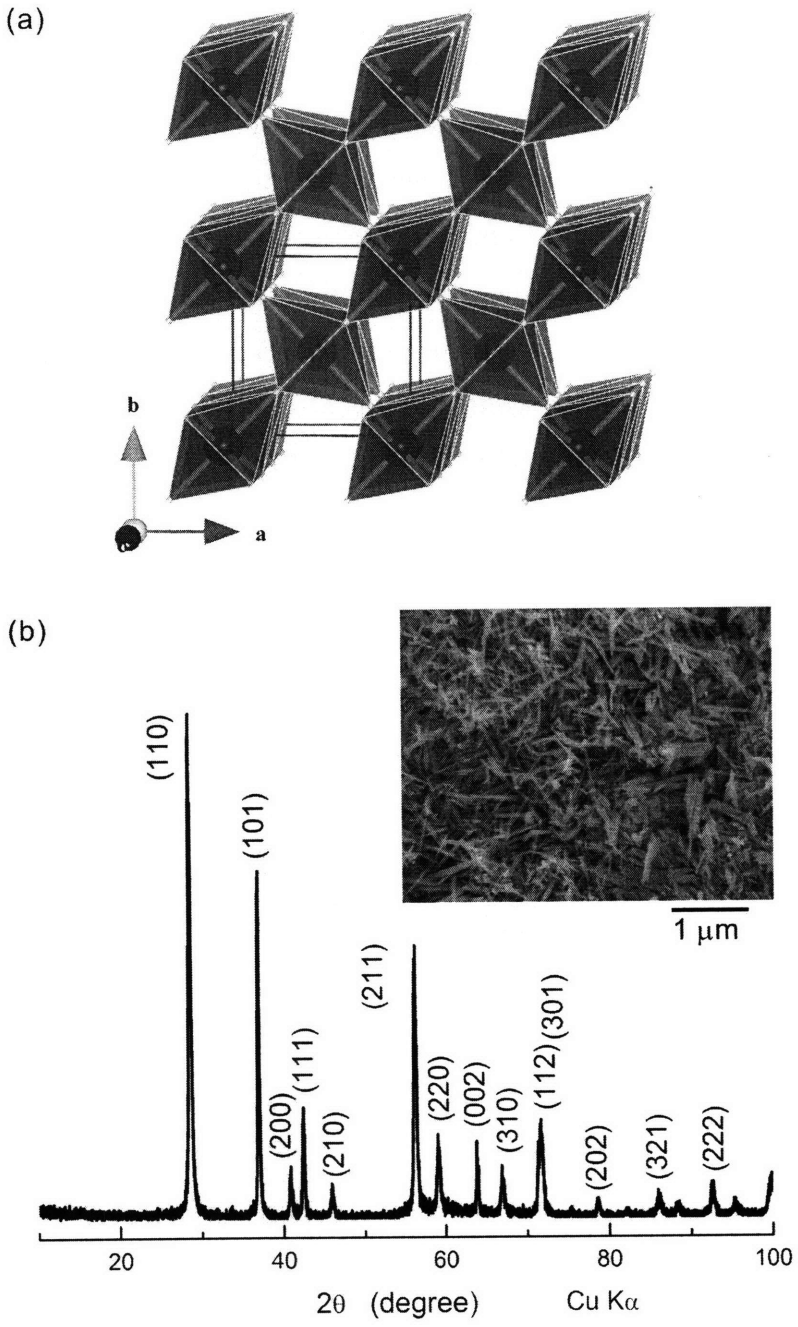

Figure 5-1: (a): Crystal Structure of CrO_2. [4] (b): XRD pattern of pristine CrO_2 sample. (c): SEM of starting powder.

5.3.1 Electrochemical insertion of Li into 550 nm x 45 nm CrO_2 particles at room temperature

Room temperature lithiation of CrO_2 led to a decrease in the saturation magnetization of up to 70% (Figure 5-2). A maximum of 0.5 moles of Li per formula unit

of CrO_2 (x=0.5) could be inserted at room temperature during the electrochemical discharge process. The changes in magnetic moment correlate with structural changes apparent from X-ray diffraction measurements (Figure 5-3). The CrO_2 (101) rutile-

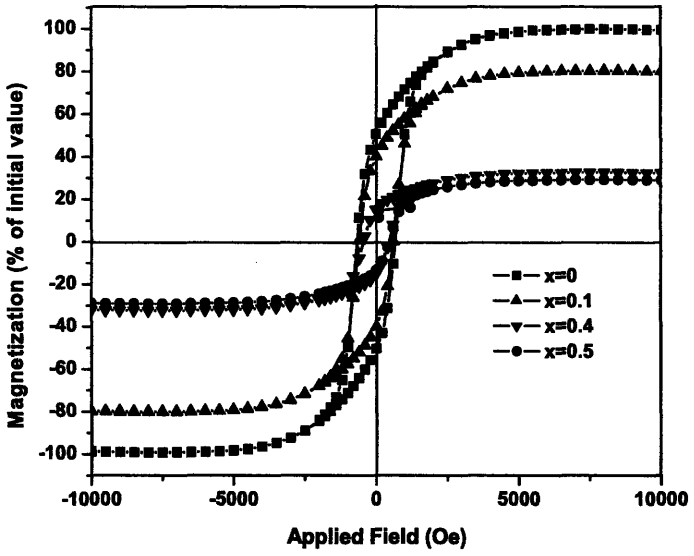

Figure 5-2: Magnetic hysteresis loops for Li_xCrO_2 with different Li contents x, normalized to the magnetization of pristine CrO_2.

structure peak broadens for x=0.1, and shoulder peaks appear at lower angles for x=0.4 and 0.5 (Fig. 5-3). This suggests an inhomogeneous expansion of the rutile lattice as lithiation proceeds. No peaks from the layered $LiCrO_2$ phase appeared up to x=0.5. Although the highest intensity peak from this compound would be obscured by a broad background peak from the other materials in the electrode, no other peaks from the compound could be identified. Peaks from the disordered rocksalt phase, observed previously upon lithiation of rutile-structured TiO_2 [86], were also not observed up to x=0.5. The shoulder peak is thus attributed to a nonferromagnetic Li^+ and Cr^{3+}-rich rutile phase. This is consistent with a report in the literature on chemical lithiation of CrO_2 at room temperature involving a topochemical reaction mechanism [87].

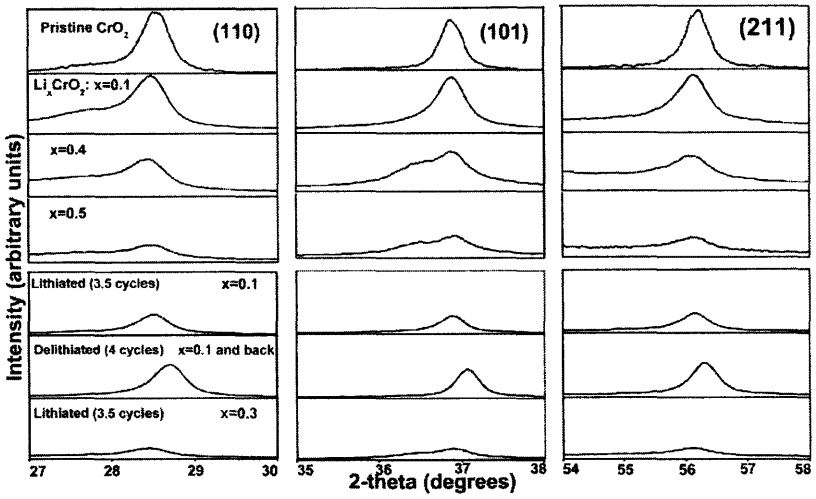

Figure 5-3: Comparison of (110) (left) (101) (middle) and (211) (right) x-ray peaks for samples discharged to different lithium contents x = 0.1, 0.4 and 0.5 at 20 °C, compared to the peak from the pristine CrO_2 sample. All peaks are shown with the same vertical scale.

5.3.2 Electrochemical reversibility of Li_xCrO_2 at room temperature

The reversibility of the Li insertion was examined by discharging samples (inserting Li) up to different values of x and then charging the samples (removing Li) to return to a nominal composition of x=0. This discharge-charge cycle was repeated up to four times. Fig. 5-4 shows the discharge-charge curves for x= 0.1, 0.2 and 0.3. The system shows near-perfect electrochemical reversibility at x=0.1, but a decrease in final voltage is observed upon cycling, which suggests that there is some structural degradation. For x=0.2, there is reasonably good electrochemical reversibility. The sample for x=0.3 shows poor electrochemical reversibility and in this case, the discharge capacity is higher than charging capacity. The corresponding structural changes are indicated in Fig. 5-3. As noted above, Li insertion lowers the CrO_2 peak intensity, broadens the peaks, and introduces additional low-angle shoulders at x=0.3 or higher. Li removal partly reverses these changes and results in an x-ray pattern close to that of the pristine powder, even for x=0.3. For example, a sample discharged to x=0.3 shows a shoulder peak adjacent to the broadened (101) peak, but

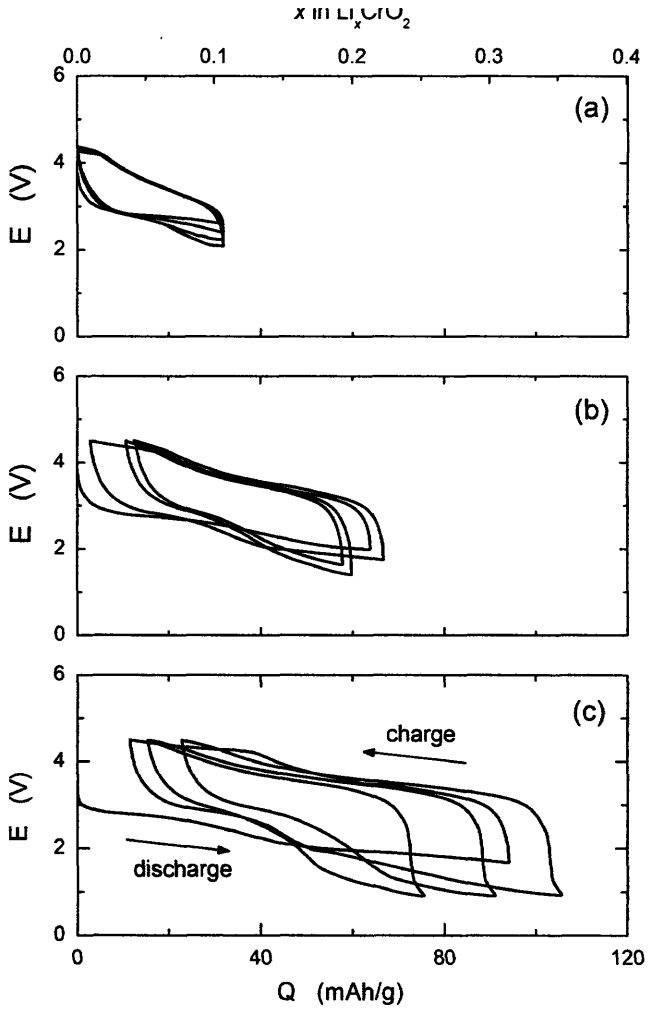

Figure 5-4: Charge and discharge cycles of CrO_2 samples at a current of 3.2 mA/g at room temperature showing the variation of cell voltage E with charge flow Q:(a) x = 0.1 (b) x = 0.2, and (c) x = 0.3, where x represents the maximum Li content inserted into each sample.

after cycling four times between x=0 and x =0.3 and returning to x=0, the shoulder peak is absent. The peak broadening is not fully reversible, for example the sample cycled four times to x=0.3 has a FWHM for the (101) peak of 0.49°, compared to 0.33° for the pristine powder and 0.84° for the discharged state. These results suggest that Li insertion creates some irreversible inhomogeneous strain in the lattice.

Intermittent discharge measurements (Fig. 5-5) supported the XRD observations. In these measurements, Li insertion is periodically interrupted by zero-current periods of relaxation lasting 5 hrs each. The open-circuit voltages (OCVs) observed after five hours of relaxation decrease as a function of x in Li_xCrO_2 with a relatively small polarization ($\sim$ 200 mV) in the low x limit. Also, much larger slope in the OCV-x curve was observed for x<0.05 than for higher lithium contents. This is consistent with the existence of predominantly a single phase, as suggested by XRD. The significantly large polarization ($\sim$ 1000 mV) in the region x>0.2 may indicate a change in the nature of the lithiation reaction at higher Li contents.

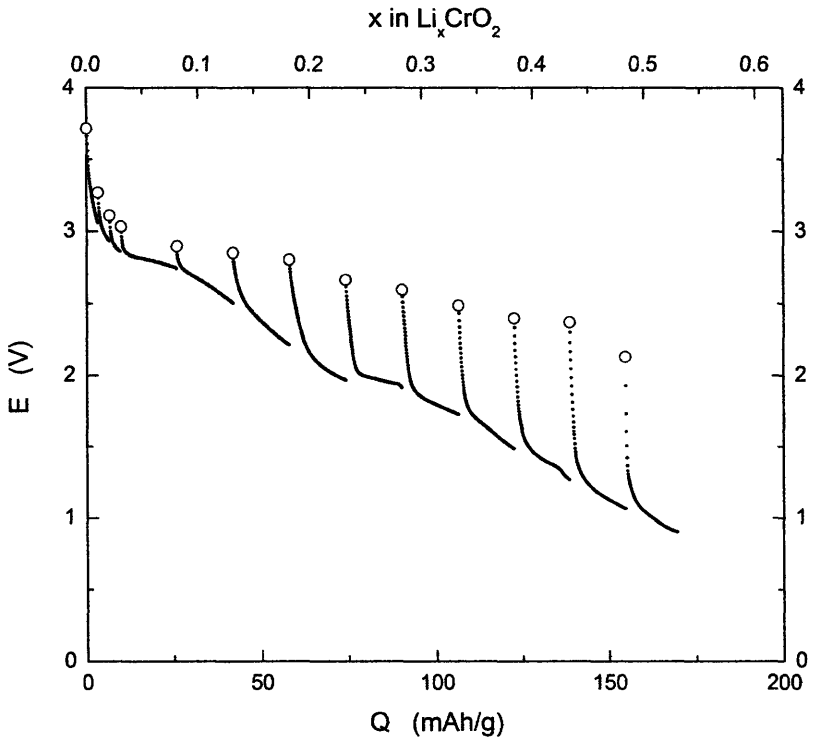

Figure 5-5: Intermittent charge curves of a CrO_2 sample at a rate of 3.2 mA/g at room temperature. The sample was charged multiple times, each one separated by a 5 hour off period. Open circles indicate the open circuit voltages measured after each 5 h current-off period.

Figure 5-7 shows the magnetization as a function of Li content for different numbers of discharge-charge cycles. Even for x = 0.1, a single complete discharge-charge cycle leads to a drop in magnetization of 15% (Fig. 5-7). Although the process

is electrochemically reversible up to x = 0.1, the magnetization is not reversible to the same extent. In contrast to the electrochemical cycling results, the magnetization changes are not fully reversible even for x=0.1 (Fig. 5-6), where a single complete discharge-charge cycle leads to a drop in magnetization of 15%.

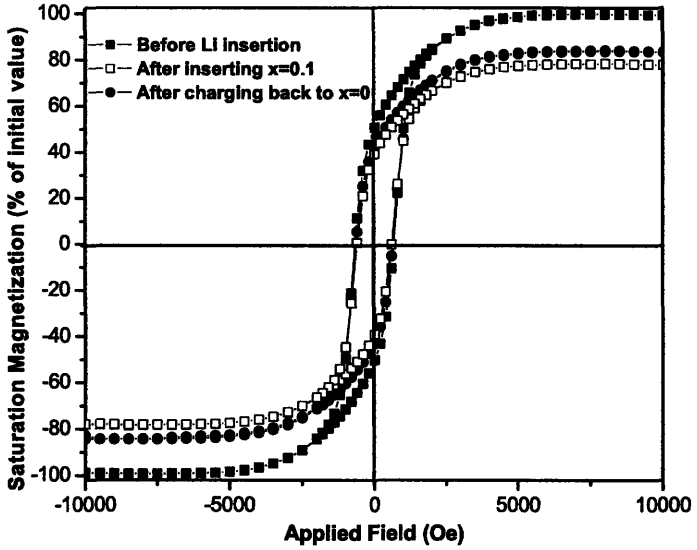

Figure 5-6: Comparison of magnetic properties before lithiation (solid squares), after insertion of x=0.1 moles of Li (open squares), and after removing Li (charging) back to x=0 (solid circles).

A larger drop in magnetization (Fig. 5-7) was obtained for three discharge-charge cycles, indicating that electrochemical cycling leads to progressively higher structural degradation. The irreversibility is more pronounced for higher x, where little of the magnetic moment is recovered on removing the Li from the structure. Figure 5-7 summarises the relation between magnetization and x for several experiments including different numbers of discharge-charge cycles.

5.3.3 Electrochemical cycling of Li_xCrO_2 at 60 °C

As mentioned in the introduction, the kinetics in this system are poor at room temperature, as is evident from the large polarization obtained upon electrochemical

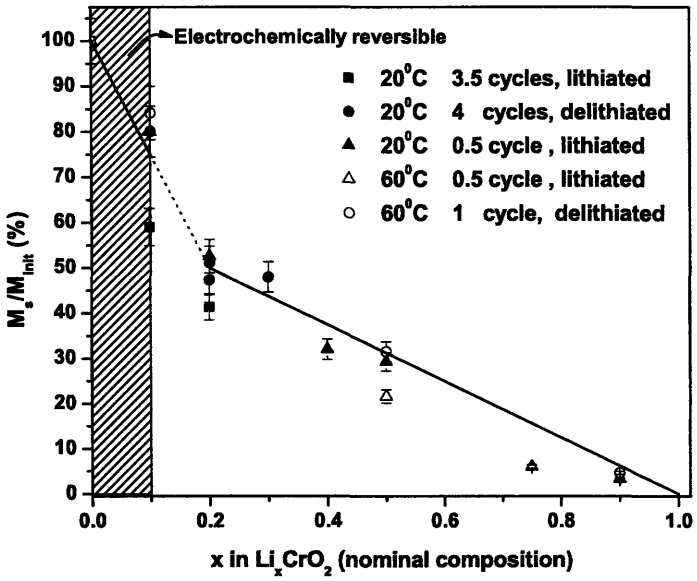

Figure 5-7: Summary of magnetization measurements of CrO_2 after electrochemical cycling. The samples were subjected to different number of discharge-charge cycles and left in the discharged (lithiated) state or the charged (delithiated) state. The solid points indicate room temperature data while the open points refer to 60 °C measurements. For example, "20 °C 3.5 cycles, lithiated" refers to a sample that has been subjected to three discharge-charge cycles at 20 °C, followed by a discharge to leave it at composition x. The shaded area of the graph indicates complete electrochemical reversibility. The lines represent model predictions for samples discharged once (triangular symbols).

cycling. Improvement in the kinetics of lithiation may be expected to increase the amount of lithium that can be inserted, and the reversibility of the structural and magnetic changes. Samples were subjected to 1-2 electrochemical cycles at 60 °C in which Li amounts varying between x=0.5 and x=0.9 were inserted. Li insertion beyond x=0.9 was limited by the cell reaching the voltage cutoff of 0.9 V. In Figure 5-8, the discharge-charge curves at room temperature and at 60 °C are plotted for comparison. There is less polarization at 60 °C, implying a reduced kinetic limitation and enabling insertion of much higher amounts of Li than is possible at room temperature.

Structurally, cycling at 60 °C also leads to broadening of the (101) peak and devel-

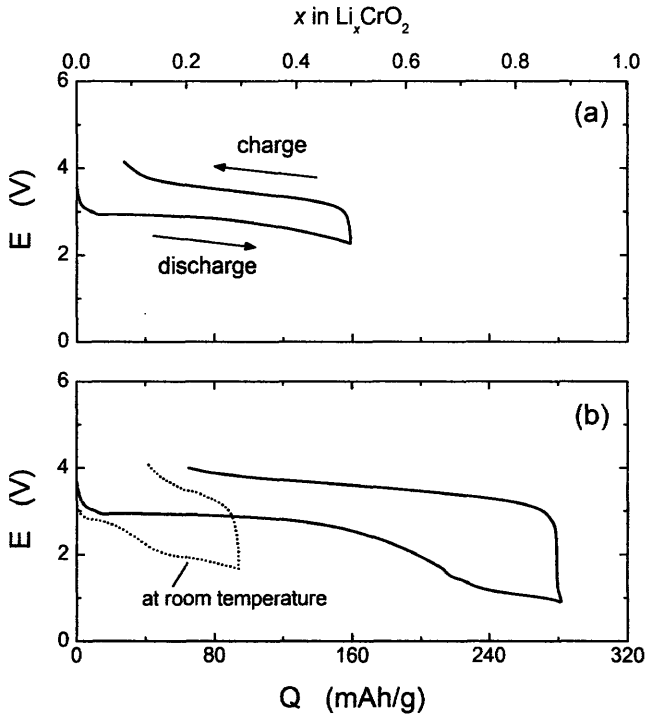

Figure 5-8: Charge and discharge cycles of CrO_2 samples at a current of 3.2 mA/g at 60 °C (solid curve) showing the variation of cell voltage E with charge flow Q: (a) x = 0.5 (b) x = 0.9, where x represents the maximum Li content inserted into each sample. The data obtained at room temperature for x = 0.3 are shown for comparison in (b) (dotted line).

opment of a shoulder peak at x=0.5 (Fig. 5-9), which decreases in intensity but does not fully disappear upon charging back to the unlithiated state. At x=0.75 and x=0.9, however, the shoulder peak is retained on charging back to x=0. The broadening of the (101) peak indicates that there is progressive destruction of long-range order in the rutile lattice, and the broadening becomes increasingly irreversible beyond x= 0.5.. The resultant changes in magnetization with Li content at 60 °C are summarized in Fig. 5-7. The magnetization is <5% of its initial value when the lithium content reaches x=0.75. However, the reversibility of the change in magnetization is still quite limited, and the electrochemical reversibility evident in the charge-discharge curves, which extends until at least x=0.5 at 60 °C, is not matched by the reversibility of the magnetization.

The $M_s(x)$ behavior in the range x=0.2 to x=1 is approximately linear (Fig. 5-

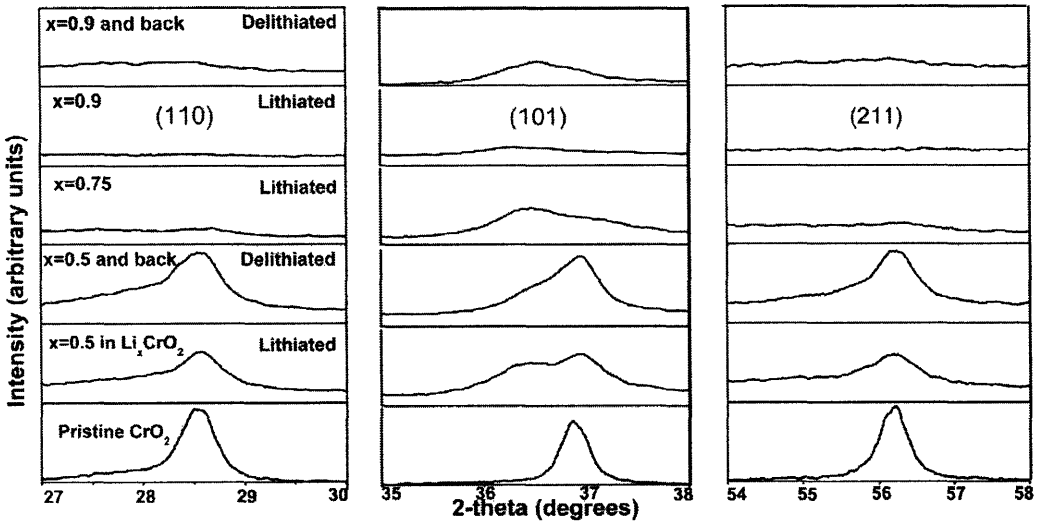

Figure 5-9: Comparison of the (110) (left), (101) (middle) and (211) (right) rutile peaks for different final charged and discharged states at 60 °C. Here the samples were either discharged once ("lithiated") or discharged and charged back ("delithiated"). The pristine sample has been normalized to fit to scale for each individual peak.

7). A possible explanation for this is the presence of two rutile-structure phases, as suggested by the x-ray diffraction data above x=0.2: one magnetic, and the other with no net moment. This is also supported by an intermittent discharge measurement that suggests two different Li insertion mechanisms in the low and intermediate x regimes(Fig. 5-5). The change in the voltage across the sample during the 5h relaxation period is modest ($\sim$ 200 mV) for x<0.1 but increases to $\sim$ 1 V for larger x, indicating a change in the kinetics of the Li insertion.

5.3.4 Modeling

To analyse the effects of Li insertion on the magnetization, we assume that the rutile framework is undisturbed upon lithiation and we consider the t_{2g}-t_{2g} interactions alone, since the e_g orbitals are empty. In CrO_2, the degeneracy of the t_{2g} states is lifted due to tetragonal symmetry. As a result, there exist d_{yz}+d_{zx} and d_{yz}-d_{zx} degenerate excited states above the d_{xy} ground state [18]. Therefore each Cr^{4+} ion in

the lattice has one localised electron in d_{xy} and an itinerant electron that has equal probability of occupying each of the excited states.

The source of the ferromagnetism is the parallel coupling of spins due to hopping of the itinerant electron between neighboring Cr^{4+} (d^2) ions. We assume that insertion of a Li^+ ion leads to reduction of a Cr^{4+} ion (of moment $2\mu_B$) into a Cr^{3+} ion ($3\mu_B$) for charge balance, and that there is no competing charge compensating mechanism, such as the filling of oxygen vacancies. The reduction of Cr^{4+} to Cr^{3+} creates d^2-d^3 and d^3-d^3 nearest-neighbor pairs, which leads to antiparallel coupling of spins through superexchange interaction between the t_{2g} orbitals.

At low Li concentrations, one can assume that d^2-d^2 and d^2-d^3 are the dominant interactions. This gives a ground state wherein the Cr^{4+} ions are coupled parallel to each other, and are coupled antiparallel to the small number of Cr^{3+} ions present. Neglecting the parallel coupling between neighboring Cr^{3+} ions, since such pairs would be present in very small concentrations, we expect a decrease in magnetic moment of 5 μ_B for each Li^+ ion that is incorporated into the structure. This corresponds to a change in moment of 1629 emu/cm^3 at 0 K, or equivalently a 250 % decrease in magnetization, for each mole of Li per formula unit of CrO_2. A line with this slope is shown on Fig. 5-7, and is in good agreement with the initial slope of M_s vs. Li content x.

The decrease in M_s with x may alternatively be a result of a decrease in Curie temperature with lithiation. To exclude this possibility, the Curie temperature of three lithiated samples was compared with that of the pristine powder. As seen in Figure 5-10, the Curie temperature decreases only by about 10 °C upon inserting 0.2 moles of Li per formula unit, which cannot account for the large changes in room-temperature M_s. As the Li content increases, d^3-d^3 and d^3-d^2 interactions become more dominant, both of which are antiparallel. This suggests that the structure will have little or no net magnetization as it approaches x=1. A loss in moment may also arise from the gradual disruption of the crystalline rutile structure at high x, evident from the x-ray diffraction data.

Finally, the irreversibility of the magnetic and structural properties, compared

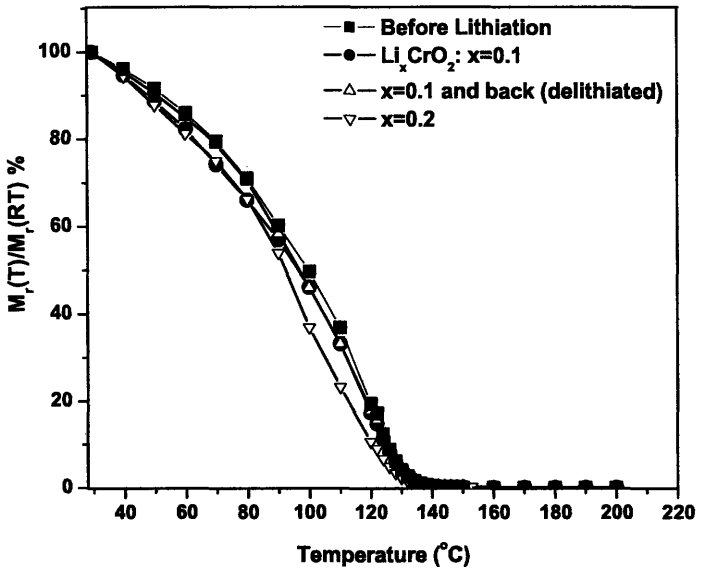

Figure 5-10: Curie temperature measurements for four CrO_2 samples, pristine (solid squares), discharged to x = 0.1 (solid circles) or 0.2 (open inverted triangles), and cycled to x=0.1 then back to x=0 (open triangles). The figure shows the remanent magnetization after saturation at 8 kOe as a function of temperature.

with the electrochemical cyclability, is attributed to structural changes or amorphization during the discharge/charge cycles.

5.3.5 Partially reversible changes in magnetic properties of 400 nm x 45 nm CrO_2 particles through electrochemical cycling

The magnetic hysteresis of the nanoparticles after different electrochemical cycling is summarized in Figure 5-11. Lithiation reduces the saturation magnetization from its initial value of 475 emu/cm^3, while leaving the coercivity largely unchanged at 450 Oe. Data are given for three electrochemical rates, C, C/10 and C/100. Samples were lithiated at constant current until the voltage reached 0.9V, corresponding to final Li contents of x = 0.06, 0.17 and 0.16 in the formula Li_xCrO_2 for rates C, C/10 and C/100 respectively. At rate C/100, the magnetization dropped to 30% of its

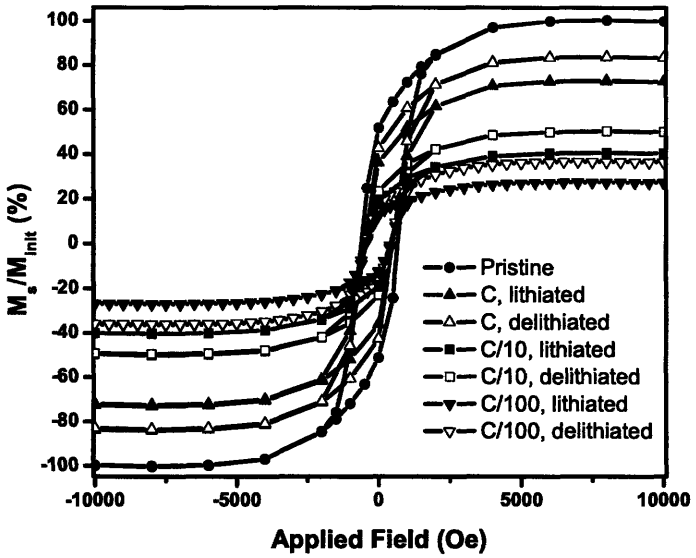

Figure 5-11: M-H curves for samples after lithiation and then after delithiation. Data are given for different electrochemical discharge rates C, C/10 and C/100. The lithiation steps result in Li contents of (after discharge 0.15, after charge back 0.06) for a rate of C, (discharge 0.38, charge 0.17) for C/10 and (discharge 0.50, charge 0.16) for C/100.

initial value. A faster Li insertion rate leads to a smaller amount of Li inserted for a given voltage cut-off, and a smaller drop in magnetization. Additional samples were identically lithiated to 0.9V then were delithiated up to a voltage of 4.5V. The saturation magnetization recovers partially upon delithiation.

The saturation magnetization is shown in Figure 5-12(a) as a function of final Li content x. The magnetization drops rapidly with increasing Li content. The amount of magnetization recovered on delithiation (i.e. the reversibility of the process) is on the order of 10% of the bulk M_s. In Figure 5-12(b), the saturation magnetization is plotted as a function of discharge rate. Higher rates lead to a smaller decrease in magnetization, though the amount of magnetization recovered on delithiation does not vary systematically with rate.

Figure 5-13 shows current-voltage loops for the discharge-charge cycle of several samples. The cell voltage of each sample starts at 3.5V, then decreases as charge

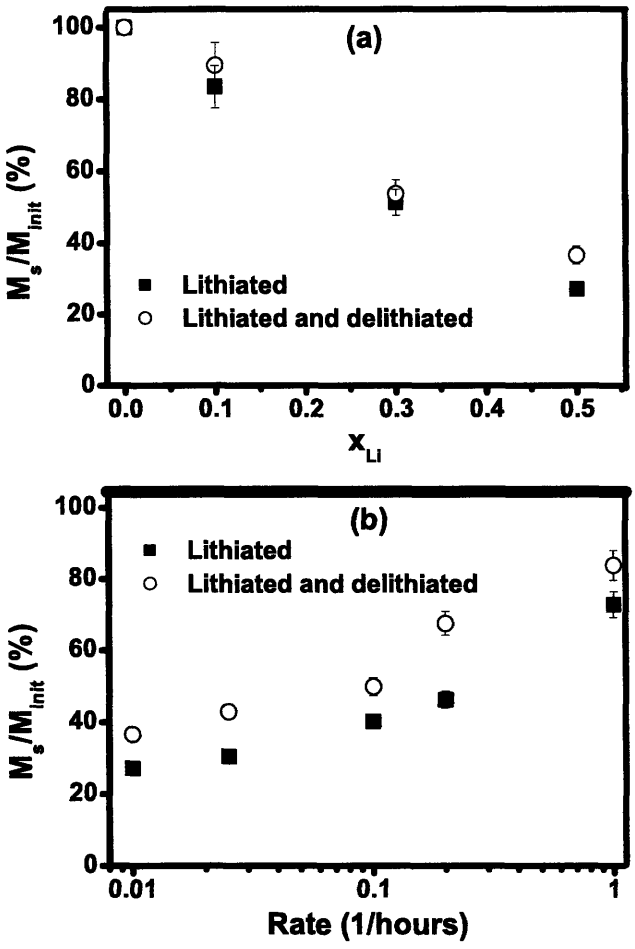

Figure 5-12: Plot of magnetization (a) as a function of lithium content in the discharged state and (b) as a function of rate for samples terminated at 0.9 V or x=0.5, whichever occurs first.

flows (the charge Q is measured in mAh per gram of CrO_2) until the cell reaches the cut-off voltage of 0.9V. Higher charge flow rates result in steeper discharge curves, i.e. a more rapid change in voltage for a given amount of charge that has flowed. This explains why smaller lithium contents are introduced at higher rates for a fixed cut-off voltage. During the delithiation part of the cycles, the voltage rises, but the loops do not close, indicating that the discharge-charge cycles are not reversible, and Li remains in the structure even after the charging process.

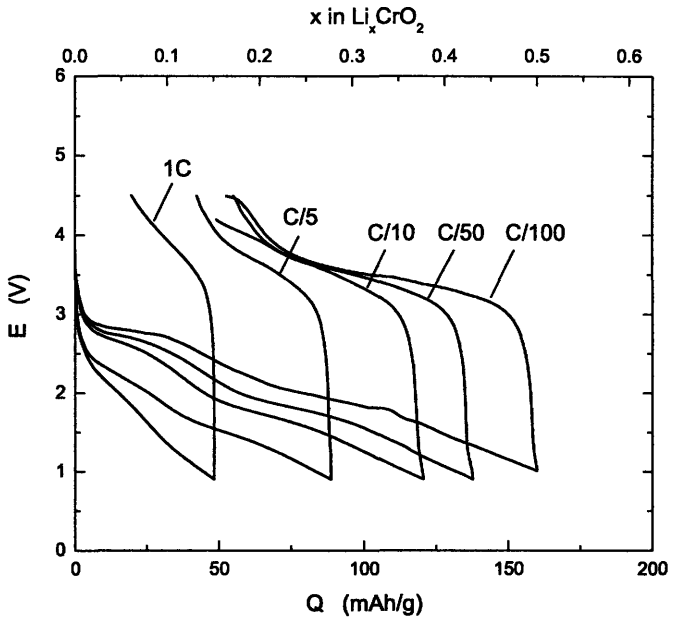

Figure 5-13: V-x plots comparing different rates of discharge for a termination voltage of 0.9 V.

Structural changes may be followed in Figure 5-14, which shows x-ray diffraction spectra for several samples. The pristine sample shows peaks characteristic of the rutile structure. These peaks are maintained at all values of Li content investigated here, but they become broader at higher x, and shoulder peaks appear near 25° and 55°. Delithiation only partially restores the structure, sharpening the peaks and reducing the intensity of the shoulder peaks. These changes are similar to those observed in 550 nm x 45 nm particles (Section 5.3), and correlate with the magnetic changes. By comparison with section 5.3.2, we assume that the shoulder peaks correspond to a Li-rich rutile-structure phase that forms at high Li contents.

The change in saturation magnetization with Li content for nanoscale CrO_2 particles resembles the results obtained for 550 nm x 45 nm CrO_2 particles tested at constant discharge rate of C/100 (Section 5.3), and there appears to be little improvement in the reversibility of magnetic properties except possibly at higher values of x. This indicates that kinetic effects, related to the rate of diffusion of Li through

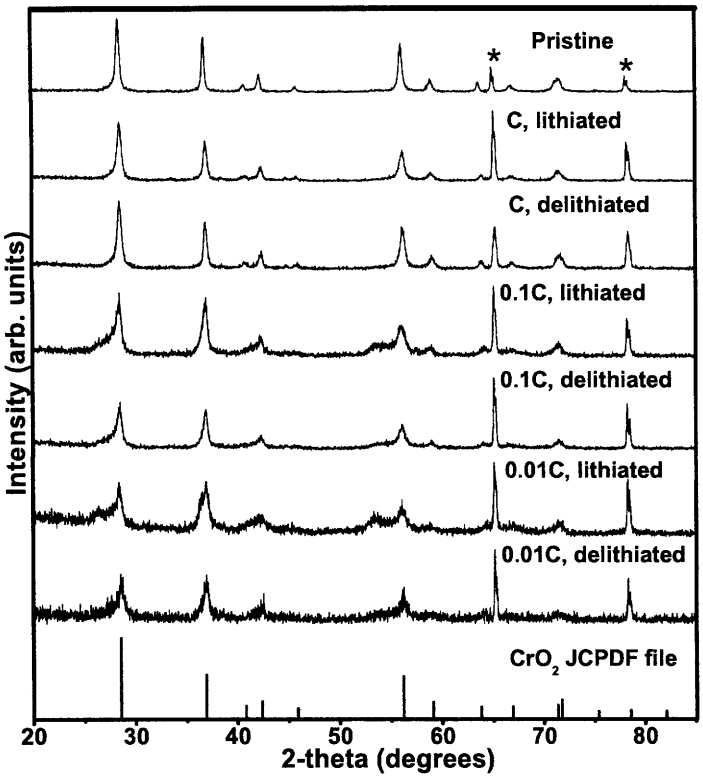

Figure 5-14: XRD plots (a) comparing different values of x (b) different rates of discharge. The asterisks indicate Al substrate peaks from the cathode assembly.

the bulk of the CrO_2, are not the dominant factors that limit the reversibility of the lithiation process in this system. The magnetic results for the nanoparticles can be interpreted in terms of the formation of one Cr^{3+} ion for each Li^+ introduced in the structure similar to the model that was described in Section 5.3.4.

5.3.6 Comparison to Literature on Rutile-Structured TiO_2

Li insertion into rutile-structured TiO_2, which is isostructural to CrO_2, is more well-studied, and has been considered for electrochromic applications in addition to being considered as a Li battery electrode [88]. In the following paragraphs, literature on Li insertion into rutile TiO_2 (space group R3m) will be discussed and compared to our results on CrO_2.

Li insertion into single crystal rutile TiO_2 showed that insertion into rutile is negligible within the voltage window of 1.5 to 3 V and primarily a surface phenomenon, later confirmed by EXAFS and XANES to be a 5 nm surface layer [88]. However, Kavan et al have shown that lithium insertion into rutile occurs, but at lower voltages and that mesoscopic rutile has reasonably reversible insertion capacity compared to single crystal rutile TiO_2, although still only half of that of anatase TiO_2 in the voltage range 1.2 V to 3 V [53]. Li insertion into rutile TiO_2 at 120 °C showed that the rutile structure is retained up to x=0.25, and there is subsequent transformation to a rocksalt phase at x=0.5. Recent studies have shown that one Li per formula unit can be inserted into nanocrystalline rutile TiO_2 in the voltage range 1 to 3 V compared to only x=0.06 for 5 to 10 μm powders of rutile TiO_2, and there is an irreversible phase transformation into the rocksalt Li_xTiO_2 phase. The initial discharge capacity increases with decrease in particle size, but the charge profiles remain largely invariant with crystallite size [31, 53]. This is consistent with the expectation of improvement in electroactivity with decreasing particle size due to shorter transport length for transport of Li and electrons, higher electrolyte-electrode contact area and better strain accommodation [29, 31, 53]. Hu et al have also shown that it is possible to reversibly accommodate 0.5 moles of Li per formula unit of nanometer-sized rutile TiO_2 (10 nm dia and 30-40 nm in length) with good capacity retention and high rate capability, compared to only 0.1-0.25 for micrometer-sized rutile [29]. The demonstration of Li insertion into rutile at 120 °C shows that it is thermodynamically favorable, and there may be kinetic restrictions that may limit the insertion capacity even at slow rates such as C/300, which may be overcome by an enhancement of the in-plane diffusivity by thermal activation [29, 31]. This is seen in our results on CrO_2 wherein the lithiation reaction can be done to a much larger extent at 60 C than at room temperature.

Further, it has been observed that there are three distinct regions in the discharge curves, namely an initial sloping regime upto x=0.35 in nanometer-sized rutile TiO_2, in which there is monophasic Li insertion; a voltage plateau at 1.4 V; and a third sloping region between 1 and 1.4 V. It is postulated that the initial sloped region in

the discharge curves for rutile TiO_2 may be due to surface storage of Li, as evidenced by a linear relation between specific surface area and the sloped capacity [29]. The 1.4 V plateau disappears in samples discharged down to 1 V, but appears in samples cut off at 1.4 V, suggesting that deep Li insertion between 1.4 and 1 V leads to an irreversible structural transformation [29, 31]. But this happens only at high lithium contents (x>0.5). It has been shown that this is due to formation of a nanocomposite of crystalline and amorphous rutile at these compositions. This work has also demonstrated the possibility of extremely high rate (up to 30C) performance of nanometer-sized rutile electrodes [29]. The voltage-charge behavior of CrO_2 at room temperature appears to be similar to that of TiO_2 (Fig. 5-8), albeit at higher voltages. There appear to be distinct regimes, the initial sloping regime, a voltage plateau at 3 V , a third sloping region between 2 V and 3V, and a voltage plateau at 2 V.

5.3.7 Comparison to Literature on the CoO_2-$LiCoO_2$ system

Comparing our results on CrO_2 to the reports on delithiated $LiCoO_2$, we find that the starting OCVs for CrO_2 is 4V, which is less than that (4.7 to 5.2 V) for fully delithiated $LiCoO_2$ [25, 89]. Upon charging back, we find that the end voltages are closer to the values reported for CoO_2. The rapid decrease of voltage during the initial stages of discharge is similar to the features observed during the de-intercalation of $LiMn_2O_4$ and $LiCoO_2$. The dip-peak-dip in the dV/dx curve at x=0.5 and the two broad peaks at x=0.15 and x=0.33 seen for CoO_2 corresponding to appearance of a Li ion ordered phase, are missing [25]. Since XRD results do not show the appearance of superlattice peaks, this possibility can be ruled out.This suggests that such Li ordering phenomena does not occur in CrO_2 and points to an alternative mechanism at work.

5.4 Conclusion

This study shows that it is possible to create large changes in the magnetization of 550 nm x 45 nm CrO_2 via electrochemical lithium insertion at room temperature or at 60 °C. In the low Li regime, below about x = 0.2 in Li_xCrO_2, a large change in magnetization of 20±2% per 0.1 Li/formula unit is obtained, and is in reasonable agreement with a model (which predicts a 25% change) for the reduction of Cr^{4+} to Cr^{3+} to balance charge as Li^+ is inserted. The change in magnetization is partly reversible, especially at low Li contents (for x<0.1). Electrochemically and structurally, the changes appear to be reversible for x<0.1, and the partial reversibility of the magnetic changes may indicate the presence of defects such as vacancies in the structure after the discharge-charge cycling, to which the magnetic moment is very sensitive. The kinetics and reversibility of the process are improved at 60 °C, and Li contents up to x=0.9 could be inserted into the structure. At these concentrations the room temperature moment is reduced to <5% of its initial value. This decrease is irreversible, due to disruption of the rutile crystal structure of the CrO_2.

The changes in magnetic and structural properties of 400 nm x 45 nm chromium dioxide nanoparticles were also investigated upon subjecting them to Li^+ insertion by galvanostatic electrochemical cycling. The results have been compared qualitatitively to the experiments on 550 nm x 45 nm particles of chromium dioxide. The changes in M_s are similar in magnitude to results on 550 nm x 45 nm CrO_2 particles. The rutile structure is preserved on Li insertion, though the peaks become broader and shoulders appear at high Li contents. The effect of rate of testing of these nanoparticles has been shown to be effectively similar to that of inserting lower amounts of Li into the structure, and the extent of reversibility of magnetic properties is similar to the 550 nm x 45 nm particles, particularly for smaller x. The lithiation reaction can be done to a much larger extent at 60 °C than at room temperature and this demonstrates that the kinetic limitations of Li diffusion in rutile due to small ab-plane diffusivity can be overcome by thermal activation, similar to TiO_2. The voltage-charge plots of CrO_2 at room temperature appears to be similar to that of TiO_2, but at higher

voltages.

The lithiation mechanism could be different from lithiation of CoO_2, which is the fully delithiated compound in the CoO_2-$LiCoO_2$ system commonly used in lithium batteries. For example, there is no evidence for formation of ordered phase that has been observed in the CoO_2-$LiCoO_2$ system. These partly reversible or irreversible and dramatic changes in magnetic moment may be useful in applications such as magnetic actuation, or programmable magnetoelectronic devices, where it may be desirable to 'switch' the magnetization of a material between different values. Moreover, the change in magnetic properties with Li insertion may be used as a sensitive probe to determine the extent of the electrochemical and structural reversibility.

Chapter 6

Conclusion

6.1 Summary

This thesis has shown that it is possible to use electrochemical lithiation to induce large changes in the saturation magnetization (M_s) of 550 nm x 45 nm and 400 nm x 45 nm particles of ferromagnetic CrO_2, and nanoparticles and thin films of ferrimagnetic Fe_3O_4.

In the case of room-temperature lithiation of 550 nm x 45 nm chromium dioxide particles, for $x < 0.2$ in Li_xCrO_2, a change in magnetization of 20±2% per 0.1 Li/formula unit is observed, and these changes have been explained with a model for the reduction of Cr^{4+} to Cr^{3+}. The change in M_s is partially reversible at low Li contents (for $x<0.1$). The changes appear to be electrochemically and structurally reversible for $x<0.1$. The kinetics and reversibility of the process can be improved by conducting the experiments at 60 °C. At 60 °C, Li contents up to $x=0.9$ could be inserted into the structure, resulting in a room temperature moment that is <5% of its initial value. This decrease is irreversible, due to disruption of the rutile crystal structure.

The changes in magnetic and structural properties of 400 nm x 45 nm chromium dioxide particles induced by electrochemical cycling have been compared qualitatively to experiments on 550 nm x 45 nm particles. The effect of increasing the rate of cycling has been shown to be similar to that of inserting lower amounts of Li. The extent of

reversibility of magnetic properties is similar to that for 500 nm x 45 nm particles, particularly for small x.

For Fe_3O_4 nanoparticles, the magnetization is expected to decrease due to formation of paramagnetic rocksalt phase. Room-temperature magnetic measurements and Curie temperature measurements suggest that there are negligible changes in magnetization until x=1, beyond which there is a monotonic decrease in M_s. Although the exact nature of the mechanism is not clear, the M_s-x behavior may be explained by possible suppression of the spinel-rocksalt phase transformation due to small size of the particles, and reaction of the impurity hematite phase with lithium in the early stages.

In Fe_2O_{3-x} thin films grown by pulsed laser deposition (PLD), a change in M_s of up to 30% was obtained by discharging down to 0.9 V versus Li/Li^+. This is smaller in magnitude compared to nanoparticles of Fe_3O_4. The smaller drop in M_s is attributed to kinetic effects resulting from the high density and greater diffusion lengths in PLD-grown films. Such changes in magnetic properties on electrochemical cycling may be useful in applications such as dynamic rheology or magnetoelectronic devices, where it may be desirable to 'switch' the magnetization of a material between different values.

6.2 Contributions of the thesis

The effects of electrochemical lithiation and cycling on structural and magnetic properties of CrO_2 have been measured. It has been shown that the process has a reversible electrochemical capacity of 30-60 mAh/g and that it is possible to get high (initial) discharge capacity (150 mAh/g) in crystalline CrO_2 at room temperature (compared to earlier reports on capacity <50 mAh/g) by discharge down to 0.9 V. It is possible to increase the (initial) discharge capacity in crystalline CrO_2 upon thermal activation (60 °C). The discharge process leads to a monotonic decrease in the saturation moment of CrO_2 with negligible changes in coercivity and remanence. The magnetic behavior was explained based on a model that takes into account

reduction of cation valence, and can be used to explain the M versus x behavior for low x (x<0.1).

Electrochemical reversibility need not guarantee reversibility of magnetic properties. Intermittent charge-discharge experiments have shown that there may be three different pathways for Li insertion in the voltage regimes 1-2 V, 2-2.7 V and 2.7-4.0 V. The effect of rate has been tested on magnetic properties and structure of needle-shaped 400 nm x 45 nm particles of CrO_2 , and it has been shown that it is similar to inserting lower amounts of Li into the structure at constant voltage cutoff. There exists the possibility of high rate capability. The effect of reduction in particle size has been explored qualitatively. It has been shown that the limiting factors may be some intrinsic kinetic limitations in rutile, such as the blocking of c-channel by already inserted Li ions and high anisotropy in diffusivity.

The effect of lithiation on structure and magnetic properties has also been demonstrated on nanoparticles of magnetite. The lithiation process has been studied on thin films of Fe_3O_4 grown on conducting substrates by Pulsed Laser Deposition.

In summary, this thesis explored the use of electrochemical lithiation-delithiation for control of magnetic properties of CrO_2 and Fe_3O_4 nanoparticles and thin films and demonstrated the possibilities and limitations of the same.

6.3 Recommendations for Future Work

There are some outstanding scientific questions that can be addressed by further experiments. As mentioned in Chapter 4, spectroscopic studies such as Mössbauer or X-ray absorption (EXAFS or XANES) could be undertaken on $Li_xFe_3O_4$ (0<x<2). These techniques provide information on the valence state and also the chemical environment of the cations in the structure and therefore could be used to determine the onset of the displacement of 8a Fe ions to 16c sites, formation of the rocksalt structure, and to differentiate the different possible mechanisms. It may also be worthwhile to perform ab-initio calculations (GGA) on Li_xCrO_2 (0<x<1) to determine the magnetic ground states.

Other materials worth investigating for this effect include cubic ferrites such as $CuFe_2O_4$, $MgFe_2O_4$ and $CoFe_2O_4$. $CuFe_2O_4$ and $MgFe_2O_4$ are particularly interesting choices. $CuFe_2O_4$ crystallizes in the inverse spinel structure, while $MgFe_2O_4$ has been shown to be a mixed spinel with a high inversion parameter [90, 91]. These possess low net magnetization since the moments of the octahedral and tetrahedral Fe cations are aligned antiparallel with each other. Lithiation will create an imbalance of moments through reduction of octahedral Fe^{3+} ions into Fe^{2+}. The Mg^{2+} and Cu^{2+} ions are expected to remain invariant upon lithiation since reduction of these to metal is less energetically favorable. These are examples of systems where magnetism can possibly be turned 'on' through electrochemical lithiation. $CoFe_2O_4$ might also be an interesting choice because its high magnetocrystalline anisotropy might be useful for applications. Magnetic perovskite compounds could also be considered. $Bi(FeNi)O_3$ is an example. The magnetic ordering in this compound depends on whether there is B-site ordering or random arrangement of ions [92]. Finally, Ti substitution in CrO_2 may also be worth considering to improve capacity since TiO_2 Li battery electrodes have been shown to have good reversible capacity.

A number of devices, such as microfluidic or solid state devices could be constructed based on these results. The following section discusses some ideas for the same. For applications in dynamic rheology, a possible way to apply this process is chemically, instead of electrochemically, using a microchannel shaped as shown in Figure 6-1 wherein controlled amounts of lithiating and delithiating agents are supplied through independently controlled valves into a microreactor containing the active material, which itself would be a suspension (magnetorheological fluid) containing micron(or sub-micron)-sized particles of the transition metal oxide. The lithiated and delithiated material can then be relayed to the application site that requires dynamic tuning of rheology. These streams can either be kept separate or combined into a single channel depending upon the application. However, there are some challenges that would need to be overcome before this can be feasible. Firstly, suitable chemistry needs to be found for the lithiating and delithiating compounds, because the chemicals need to be stable in the carrier media that are typically used in magne-

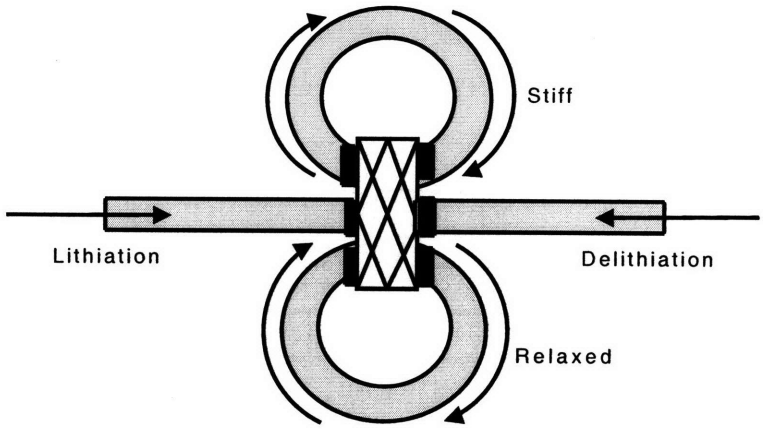

Figure 6-1: Schematic of a microfluidic device employing the effect

torheological fluids. These may include compounds like n-butyl lithium for lithiation, and NO_2BF_4 for delithiation. Secondly, the individual particles may have to be engineered on the nanoscale to enable fast reaction rates. MR fluids presently used in magnetoviscous applications use applied fields of 500 Oe or 40 kA/m to produce the required changes in flow behavior of micron-sized Fe particles. This corresponds to a magnetic induction of 1.2 T or 1000 kA/m. As a comparison, the use of such electrochemically stimulated changes in magnetization on these materials, would, at best, produce changes in magnetization 500 kA/m (approximately equal to the saturation magnetization of Fe_3O_4 and CrO_2). However such a method would have the merit of not requiring the application of large magnetic fields, and therefore maybe useful in certain applications.

For applications as Li ion sensors, CrO_2 may be a promising candidate since a large M_s-x slope of 1629 emu/cc/mol of Li was obtained upon lithiation. This corresponds to a slope of ~300 emu/g/mole of Li. Factoring in the weight of the active material used in the porous electrodes (~10 mg), the resultant change in M_s is ~3 emu/mole of Li. Since most magnetometers have a sensitivity of $\sim 10^{-5}$ emu or better, this effect can possibly yield good sensitivity and low detection limits for Li ions. For comparison, lithium sensors based on ion selective electrodes (ISE) and ion selective field-effect transistors (ISFETs) have ionic sensitivity of $\sim$ 50 mV/pLi and detection limits of $\sim 10^{-6}$ mol/l [93, 94, 95].

Solid state magnetic devices employing this effect would need to be designed similar to a thin film Li battery. This would perhaps involve a multilayer stack as shown in Figure 6-2 for CrO_2. The multilayer stack could be built on a substrate

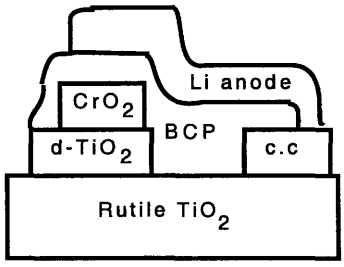

Figure 6-2: Schematic of a solid state device employing the effect

like TiO_2 (rutile), with doped TiO_2 or RuO_2 serving as the cathode current collector. A block copolymer film, spun coat on top of the active CrO_2 layer and the anode current collector, can serve as the electrolyte. The cathode current collector can be grown by MOCVD, while CrO_2 has been grown successfully by researchers by CVD using chromyl chloride as precursor.

This is a long-term view of the applicability of this work, which would need (de)magnetizing or switching currents (constant) of roughly 10 $\mu A/cm^2$ assuming a 10nm thick patterned CrO_2 film, full theoretical capacity and a charge-discharge rate of 10C. This is very low compared to the power requirements in MRAMs, which typically require current densities of 10^7-10^8 A/cm^2 for spin transfer torque based switching. However, as mentioned in Chapter 1, these devices would be severely limited in terms of switching time (Table 6.1). In rutile-structured nanoelectrodes of TiO_2, researchers have achieved capacities of 70 mAh/g at a discharge/charge rate of 30C [29]. Assuming that a similar rate can be achieved with CrO_2, this corresponds to an extremely slow switching time of 30 s. In principle, this could be made 10^8 (D_c/D_{ab}) times faster if the anisotropy of Li diffusion in rutile be fully exploited. This could yield a switching time ~300 ns, and is listed as the best case in Table 6.1. This might be achieved by reproducing the experiments in a solid-state lithium battery with (001) oriented CrO_2 patterned thin films. This is based on the assumption that the rate of diffusion in rutile is limited by the ab plane diffusivity which is 8

orders of magnitude slower than the c-axis diffusivity [77].

This effect is thus clearly not suitable for high speed applications, although it may compare favorably in terms of speed to Flash (NAND) technology. Furthermore, present day lithium batteries have a life of 300-500 cycles, which is the number of discharge-charge cycles that they can be used for without fading of capacity. This is very unsatisfactory for memory devices. For comparison, Flash memories have an endurance (number of write cycles) of 10^5 while MRAMs have almost infinite endurance. Therefore, at best, such devices can be used for low endurance applications (<10000 cycles for a given byte). A key requirement for such practical applications

Table 6.1: Comparison with existing and prototype memory technologies

	MRAM	STT	Flash(NOR)	Flash(NAND)	Li device
Write/erase time	3-20 ns	2-20 ns	1 μs/10 ms	1 ms/0.1 ms	300 ns(best)
Write power	high	low	very high	very high	low
Voltage	3 V	0.15 V	6-8 V	16-20 V	1-4 V
Endurance	$>10^{15}$	$>10^{15}$	10^5	10^5	300-500

is the need to enhance reversibility of the effect by avoiding destruction of rutile framework (amorphization/phase transformation) due to the strain created by Li-ion insertion. The strain created by the electrochemical process could possibly be managed by using strained epitaxial films. For example, if a (001) oriented film with in-plane (ab) tensile stresses were to be used, it might make the lithium insertion process easier, since lithium insertion would allow relaxation of the tensile stresses by expansion of the lattice. However this could make the delithiation process more difficult since that involves compression in the (ab) plane. The effect of stresses on the lithiation-delithiation process in CrO_2 is an unanswered question that merits investigation especially for solid state application of this effect.

Another approach for building solid state devices may involve using nano architectured electrodes that have been recently developed for high power density conversion electrode applications. These electrodes can be made by depositing the active material onto nanostructured current collectors (copper nanorods) that are electrodeposited into the pores in anodized porous alumina membranes. These provide the advantage

of short diffusion lengths without compromising the need for proper electrical contact between the particles of the active material [65].

Finally, it is possible to envisage use of ions other than Li to accomplish the same effect. Protonation (insertion of H^+ ions), a process used in Proton Exchange Membrane Fuel Cells and electrochemical supercapacitors, is one such process [96, 97, 98]. The small size of diffusing species (protons) could potentially result in lesser structural damage, improved kinetics and better reversibility. CrO_2 might be a promising material in this regard, since rutile-structured RuO_2 and V-substituted RuO_2 have been used as cathodes for electrochemical capacitors [97, 98].

Appendix A

Prediction of magnetic properties of oxides

The following sections give more details on prediction of magnetic properties of oxides through the application of Goodenough rules [21]. Tables are available in Ref. [21], which can be used to determine the orientation of moments in different cases (d^5-d^5, d^3-d^5, for example) arising due to both delocalization and correlation mechanisms. These tables deal with octahedral configuration of the cations, and the bond angles dealt with are 90 and 180 degrees. However for most cases that are of interest (for example in spinels), the cation-anion-cation angles encountered are intermediate between 90 and 180 degrees. For intermediate angles, Goodenough suggests interpolation by looking at the extreme bond angles. For example, if the orientation is antiparallel for the 180^o case, and parallel for the 90^o case, then it is suggested that somewhere between 125^o and 135^o, there is the transition from parallel to antiparallel type of behavior.

A.1 Application of Goodenough's rules

The prediction of magnetic behavior of a system via Goodenough rules involves the following steps:

I. Application of Goodenough rules to get the sign of the exchange coefficients.

This involves: (a) Writing down the electronic configurations of the d-orbitals of the magnetic cations, taking into account crystal field splitting and spatial configurations (i.e. tetrahedral (A) or octahedral (B)) and identifying the cation-anion-cation angles. (b) Arriving at the relative orientations (parallel or antiparallel) of the cation spins for each type of cation-anion-cation combination: This may involve interpolation from the orientations obtained at 90^o and 180^o in case the angle involved is intermediate between 90 and 180 degrees. In some cases, such as d^5-d^5, d^3-d^5, etc. the relative orientation at 90 and 180 degrees can be obtained from the tables in Goodenough's book [21]. In other cases, one can predict it by going through the following steps: (i) Considering all possible superexchange mechanism between all combinations of orbitals (i.e. e_g-e_g, e_g-t_{2g} and t_{2g}-t_{2g}). In each case, the relative spin orientation of the ions can be predicted to be the one that maximizes hopping probability of an electron jumping from one ion to the next (between the orbitals in question). The maximum hopping probability corresponds to the situation in which energy of the resultant electronic configuration of the ion (to which the electron has hopped) is minimal. It should be noted that the spin of an electron is preserved upon hopping. Mechanisms that involve the overlap of orthogonal orbitals need not be considered. Examples are: 1. 180^o cation-anion-cation delocalization interaction between e_g and t_{2g} orbitals.

2. 90^o and 180^o cation-anion-cation correlation interaction via s- orbital (of oxygen) between t_{2g}-t_{2g} and t_{2g}-e_g orbitals.

(ii) The overall interaction between a particular pair of cations can be arrived at by taking into account contributions from various superexchange mechanisms. For example, if most of the interactions are antiparallel, the overall interaction is antiferromagnetic for that particular cation-anion-cation combination. (i.e. J_{ij} is negative).

II. Solving for the spin groundstate. The relative spin orientations obtained by application of Goodenough may not be realizable in practice due to geometrical frustration. This is the case in complicated crystal structures, like the spinel. In such cases, we need to use the predictions of Goodenough rules in conjunction with crys-

tal structure information to get the spin ground state (the alignment of spins that would lead to the minimum energy). This determines whether the system behaves as a ferromagnet, antiferromagnet or a ferrimagnet.

As an example, let us suppose that, from the application of Goodenough's rules, it is inferred that all the exchange coefficients are negative (i.e. favor antiferromagnetic exchange); then the overall tendency is for the ions to align antiparallel to each other (to minimize the pairwise energy). Crystal structure information can then be used to say which pairs of ions would be parallel or antiparallel to minimize the overall energy.

Factors that should be considered here are:

1) Bond distances: Ions that are separated by smaller distances interact more strongly than those that are farther apart, and hence contribute more to the overall energy. Therefore such pairs of ions should have antiparallel spins.

2) Number of nearest neighbors of each type of ion: If there are more A-B nearest neighbor pairs than A-A and B-B, for example, then A and B ions should be aligned antiparallel to achieve minimum energy. Therefore, in the spin groundstate, A and B should be antiparallel. From this the spin orientations of the other cation pairs could be arrived at, and hence the spin ground state.

Once the spin ground state is arrived at, it is relatively easy to say what the magnetic behavior of the compound is, though arriving at the spin ground state itself could be a non-trivial task for complicated crystal structures.

Bibliography

[1] C.J. Jones. *d- and f-block chemistry.* Cambridge: Royal Society of Chemistry, 2001.

[2] K. Kang and G. Ceder. *Phys. Rev. B*, 74:094105, 2006.

[3] J. M. Neto and P. H. Domingues. *J. Mater. Sci. Lett.*, 16:231–233, 1997.

[4] K. Momma and F. Izumi. *Commission on Crystallogr. Comput., IUCr Newslett.*, 7:106, 2006.

[5] I. Zutic, J. Fabian, and S. D. Sarma. *Rev. Mod. Phys.*, 76:323, 2004.

[6] M. Bibes and A. Barthelemy. *IEEE Trans. Electron Devices*, 54:1003, 2007.

[7] J. S. Parker, S. M. Watts, P. G. Ivanov, and P. Xiaong. *Phys. Rev. Lett.*, 88:196601–1, 2002.

[8] C. M. Fang, G. A. de Wijs, and R. A. de Groot. *J. Appl. Phys.*, 91:8340, 2002.

[9] O. Kahn and C. J. Martinez. *Science*, 279:44, 1998.

[10] C. Janiak. *Dalton Transactions*, page 2781, 2003.

[11] J. Fontcuberta, J. Rodriguez, M. Pernet, G. Longworth, and J.B. Goodenough. *J. App. Phys.*, 59:1918–1926, 1986.

[12] J. M. D. Coey and M. Venkatesan. *J. Appl. Phys.*, 91:8345, 2002.

[13] J. M. D. Coey and S. Sanvito. *J. Phys. D: Appl. Phys.*, 37:988, 2004.

[14] B. V. Reddy and S. N. Khanna. *Phys. Rev. Lett.*, 83:3170, 1999.

[15] Jr. R. J. Soulen, J. M. Byers, M. S. Osofsky, B. Nadgorny, T. Ambrose, S. F. Cheng, P. R. Broussard, C. T. Tanaka, J. Nowak, J. S. Moodera, A. Barry, and J. M. D. Coey. *Science*, 282:85, 1998.

[16] W. J. De Sisto, P. R. Broussard, T. F. Ambrose, B. E. Nadgorny, and M. S.Osofsky. *Appl. Phys. Lett.*, 76:3789, 2000.

[17] Y. Ji, G. J. Strijkers, F. Y. Yang, C. L. Chien, J. M. Byers, A. Anguelouch, G. Xiao, and A. Gupta. *Phys. Rev. Lett.*, 86:5585, 2001.

[18] P. Schlottmann. *Phys. Rev. B*, 67:174419–1, 2003.

[19] J.B. Goodenough. *Prog. Solid State Chem.*, 26:359, 1972.

[20] A. D. Smith and Y. Huai. *Future Fab Intl.*, 23.

[21] J.B. Goodenough. *Magnetism and the Chemical Bond.* Robert E. Krieger Publishing Company, 1976.

[22] K.Persson and G. Ceder. *Unpublished.*

[23] M. A. Korotin, V. I. Anisimov, D. I. Khomskii, and G. A. Sawatzky. *Phys. Rev. Lett.*, 80:4305, 1998.

[24] A. Van der Ven and G. Ceder. *Electrochem. Solid-State Lett.*, 3:301, 2000.

[25] T. Motohashi, Y. Katsumata, T. Ono, R. Kanno, M. Karppinen, and H. Yamauchi. *Chem. Mater.*, 19:5063–5066, 2007.

[26] S. Y. Chung, J.T. Bloking, and YM. Chiang. *Nature Materials*, 1:123, 2002.

[27] M. M. Thackeray. *J. Am. Ceram. Soc.*, 82:3347–3354, 1999.

[28] SY Huang, L Kavan, I Exnar, and M Grtzel. *J. Electrochem. Soc.*, 142:L142–L144, 1995.

[29] YS. Hu, N. Kienle, YG. Guo, and J. Maier. *dv. Mater.*, 18:1421–1426, 2006.

[30] M. A. Reddy, M.S. Kishore, V. Pralong, V. Caignaert, U. V. Varadaraju, and B. Raveau. *Electrochem. Comm.*, 8:1299–1303, 2006.

[31] C. Jiang, I. Honma, T. Kudo, and H. Zhao. *Electrochem. Solid-State Lett.*, 10:A127–A129, 2007.

[32] M. M. Thackeray, W. I. F. David, and J. B. Goodenough. *Mater. Res. Bull.*, 17:785–793, 1982.

[33] D. Larcher, C. Masquelier, D. Bonnin, Y. Chabre, V. Masson, J. B. Leriche, and J. M. Tarascon. *J. Electrochem. Soc.*, 150:A133–A139, 2003.

[34] Douglas. B. Chrisey and Graham K. Hubler. *Pulsed Laser Deposition of Thin Films.* Wiley-Interscience, 1994.

[35] F. Ilievski, T. Tepper, and C. A. Ross. *IEEE Trans. on Magnetics*, 39:3172, 2003.

[36] T. Tepper, F. Ilievski, C. A. Ross, T. R. Zaman, R. J. Ram, S. Y. Sung, and B. J. H. Stadler. *J. App. Phys.*, 93:6948, 2003.

[37] S. Foner. *Rev. Sci. Instrum.*, 30:548, 1959.

[38] A. Zieba and S. Foner. *Rev. Sci. Instrum.*, 53:1344, 1982.

[39] G. J. Bowden. *J. Phys. E: Sci. Instrum.*, 5:1115, 1972.

[40] S. Foner. *J. Appl. Phys.*, 79:4740, 1996.

[41] D. Feldmann and R. P. Hunt. *Z. InstrumKde*, 72:259, 1964.

[42] R. C. O'Handley. *Modern Magnetic Materials.* Wiley Interscience, 1997.

[43] V. Sivakumar, S. Kumar, C. A. Ross, and Y. Shao-Horn. *ECS Trans.*, 2(8):1, 2006.

[44] V. Sivakumar, S. Kumar, C. A. Ross, and Y. Shao-Horn. *IEEE Trans. Mag.*, 43:3121, 2007.

[45] S. Ma and H. Noguchi. *J. Electrochem. Soc.*, 148:A589–A594, 2001.

[46] E. Ferg, R. J. Gummor, A. de Kock, and M. M. Thackeray. *J. Electrochem. Soc.*, 141:L147, 1994.

[47] N. Koshiba, K. Takada, M. Nakanishi, E. Asaka, and Z. Takehara. *J. Electrochem. Soc.*, 62:870, 1994.

[48] D. Larcher, D. Bonnin, R. Cortes, I. Rivals, L. Personnaz, and J. M. Tarascon. *J. Electrochem. Soc.*, 150:A1643–A1650, 2003.

[49] A Ahniyaz, T Fujiwara, SW Song, and M Yoshimura. *Solid State Ionics*, 151:419–423, 2002.

[50] P. Poizot, S. Laurelle, S. Grugeon, L.Dupont, and J-M. Tarascon. *Nature*, 407:496, 2000.

[51] S. Kohiki, K. Hori, A. Kawaguchi, Y. Murakawa, H. Shimooka, T. Tajiri, H. Deguchi, M. Mitome, Y. Bando, S. Fukushima, M. Arai, M. Oku, and T. Shishido. *Jpn. J. App. Phys.*, 43:L1620, 2004.

[52] M. Tabuchi, S. Tsutsui, C. Masquelier, R. Kanno, K. Ado, I. Matsubara, S. Nasu, and H. Kageyama. *J. Solid State Chem.*, 140:159, 1998.

[53] L. Kavan, D. Fattakhova, and P. Krtil. *J. Electrochem. Soc.*, 146:1375, 1999.

[54] B. Fuchs and S. Kemmler-Sack. *Solid State Ionics*, 68:279, 1994.

[55] K. Ado, M. Tabuchi, H. Kobayashi, H. Kageyama, O. Nakamura, Y. Inaba, R. Kanno, M. Takagi, and Y. Takeda. *J. Electrochem. Soc.*, 144:L177, 1997.

[56] R. Kanno, T. Shirane, Y. Kawamoto, Y. Takeda, M. Takano, M. Ohashi, and Y. Yamaguchi. *J. Electrochem. Soc.*, 143:2435, 1996.

[57] X. Wang, L. Gao, L. Li, H. Zheng, Z. Zhang, W. Yu, and Y. Qian. *Nanotechnology*, 16:2677–2680, 2005.

[58] P. H. Domingues, E. Nunez, and J. M. Neto. *Journal Of Magnetism And Magnetic Materials*, 96:101–104, 1991.

[59] P. H. Domingues, J. M. Neto, M. R. Silva, and M. El. Massalami. *Hyperfine Interactions*, 133:41–46, 2001.

[60] V.L. McLaren, C.A. Kirk, M. Poisot, M. Castellanos, and A.R. West. *Dalton Trans.*, 19:3042, 2004.

[61] T. Tepper and C. A. Ross. *J. App. Phys.*, 91:4453, 2002.

[62] X. N. Xu, Y. Wolfus, A. Shaulov, Y.Yeshurun, I. Felner, I. Nowik, Yu Koltypin, and A. Gedankenet. *J. App. Phys.*, 91:4611–4616, 2002.

[63] S. Kanzaki, T. Inada, T. Matsumura, N. Sonoyama, A. Yamada, M. Takano, and R.Kanno. *Journal of Power Sources*, 146:323–326, 2005.

[64] S.Ito, K. Nakaoka, M. Kawamura, K. Ui, K. Fujimoto, and N. Koura. *J. Power Sources*, 146:319, 2005.

[65] P. L. Taberna, S. Mitra, P. Poizot, P.Simon, and J-M. Tarascon. *Nature Materials*, 5:567, 2006.

[66] R. Koksbang, D. Fauteaux, P. Norby, and K. A. Nielsen. *J. Electrochem. Soc.*, 136:598, 1989.

[67] R. Vidya, P. Ravindran, A. Kjekshus, and H. Fjellvag. *Phys. Rev. B*, 73:235113, 2006.

[68] M. Suzuki, I. Yamada, H. Kadowaki, and F. Takei. *J. Phys.: Condens. Matter*, 5:4225, 1993.

[69] T. A. Hewston and B. L. Chamberland. *J. Phys. Chem. Solids*, 48:97, 1987.

[70] E. J. Wu, P. D. Tepesch, and G. Ceder. *Phil. Mag. B*, 77:4, 1998.

[71] A.P. Ramirez. *Annu. Rev. Mater. Sci.*, 24:453, 1994.

[72] W. Li, J. N. Reimers, and J. R.Dahn. *Phys. Rev. B.*, 49:826, 1994.

[73] S. Madhavi, G. V. Subba Rao, B. V. R. Chowdari, and S. F. Y. Li. *Electrochimica Acta*, 48:219, 2002.

[74] S. Miyazaki, S. Kikkawa, and M. Koizumi. *Synthetic Metals*, 6:211, 1983.

[75] Y. Takeda, R. Kanno, Y. Tsuji, and O. Yamamoto. *J. Power Sources*, 9:325, 1983.

[76] J. Kim and A. Manthiram. *J. Electrochem. Soc.*, 144:3077, 1997.

[77] M.V. Koudriachova, N.M. Harrison, and S.W. de Leeuw. *Phys. Rev. Lett.*, 86:1275, 2001.

[78] A. Stashans, S. Lunell, and R. Bergstrom. *Phys. Rev. B*, 53:159, 1996.

[79] M. V. Koudriachova, N. M. Harrison, and S. W. de Leeuw. *Solid State Ionics*, 157:35, 2003.

[80] O. W. Johnson. *Phys. Rev.*, 136:A284, 1964.

[81] W.J. Macklin and R.J. Neat. *Solid State Ionics*, 53 - 56:694, 1992.

[82] W. C. Mackrodt. *J. Solid State Chem.*, 142:428–439, 1999.

[83] R. Dovesi C. Pisani and C. Roetti. *Ab-initio Hartree-Fock Treatment of Crystalline Systems.* Springer-Verlag, Berlin/New York, 1988.

[84] X. Zhang, Y. Chen, L. Lu, and Z. Li. *J. Phys. Cond. Mat.*, 18:L559, 2006.

[85] M. A. Alario Franco and K. S. W. Sing. *J. Thermal Analysis and Calorimetry*, 4:47, 1972.

[86] E. Baudrin, S. Cassaignon, M. Koelsch, J. P. Jolivet, L. Dupont, and J. M. Tarascon. *Electrochem. Comm.*, 9:337, 2007.

[87] D. W. Murphy, F. J. Di Salvo, J. N. Carides, and J. V. Waszczak. *Mater. Res. Bull.*, 13:1395, 1978.

[88] M. Wagemaker, D. Lutzenkirchen-Hecht, P. Keil, A. A. van Well, and R. Frahm. *Physica B*, 336:118–123, 2003.

[89] G. G. Amatucci, J. M. Tarascon, and L. C. Klein. *J. Electrochem. Soc.*, 143:1114, 1996.

[90] V. Krishnan, R. K. Selvan, C. O. Augustin, A. Gedanken, and H. Bertagnolli. *J. Phys. Chem. C*, 111:16724, 2007.

[91] S. M. Antao, I. Hassan, and J. B. Parise. *American Mineralogist*, 90:219, 2005.

[92] G.F. Dionne, A. R. Taussig, M. Bolduc, L. Bi, and C. A. Ross. *J. App. Phys.*, 101:09c524, 2007.

[93] Yu. Ermolenko, T. Yoshinobu, Yu. Mourzina, S. Levichev, K. Furuichi, Yu. Vlasov, M. J. Schning, and H. Iwasaki. *Sensors and Actuators B*, 85:79, 2002.

[94] T. Matsuo and K. D. Wise. *IEEE Trans. Biomed. Eng.*, page 485, 1974.

[95] M. J. Madou and S. R. Morrison. *Chemical sensing with solid state devices.* Academic Press, London, 1989.

[96] R. Kötz and M. Carlen. *Electrochimica Acta*, 45:2483, 2000.

[97] V. Subramanian, S. C. Hall, P. H. Smith, and B. Rambabu. *Solid State Ionics*, 175:511, 2004.

[98] K. Yokoshima, T. Shibutani, M. Hirota, W. Sugimoto, Y. Murakami, and Y. Takasu. *J. Power Sources*, 160:1480, 2006.